



Residual circulation in tidally energetic estuaries: contributions and dependencies

Doctoral thesis

Elisabeth Schulz

Residual circulation in tidally energetic estuaries:
contributions and dependencies

Dissertation

zur Erlangung des akademischen Grades
doctor rerum naturalium (Dr. rer. nat.)
der Mathematisch-Naturwissenschaftlichen Fakultät
der Universität Rostock

vorgelegt von
Elisabeth Schulz, geb. Fischer,
geb. am 07.12.1984 in Rostock

Rostock, 14.10.2014

Gutachter: Prof. Dr. Hans Burchard
Leibniz-Institut für Ostseeforschung Warnemünde (IOW)
Rostock, Deutschland

UD Dr. Henk M. Schuttelaars
Technische Universiteit Delft (TU Delft)
Delft, Nederland

Verteidigungsdatum: 16.12.2014

Abstract

Estuaries are complex systems influenced by many different parameters and processes, for example tidal currents from the ocean side and river discharge from the inland side. Accordingly, estuarine circulation is composed of many contributions, the knowledge of which is essential for a proper management of estuaries. The circulation contributions and their dependencies on the influencing parameters can be investigated by means of numerical hydrodynamic models.

The simulation results reveal that the tidal straining circulation is the dominant contribution in a large part of the parameter space. This circulation arises from tidal asymmetries of stratification and shear. In tidally energetic estuaries, stratification is generally diminished by the along-estuary flood currents and induced by the along-estuary ebb currents, but it can also be induced by across-estuary circulation. Depending on the cross-sectional shape of an estuary, the across-estuary circulation can even be much more efficient in inducing strong ebb stratification than the along-estuary currents. Thus, also the tidal straining circulation and the total, estuarine circulation depend on the shape, for example the depth-to-width ratio, of an estuary. Other influencing parameters identified to be important are the minimum-to-maximum depth ratio, the along-estuary salinity gradient and the across-estuary diffusivity.

A more profound abstract of the main study - about the impact of the depth-to-width ratio on the residual along-estuary circulation - can be found at the beginning of the second chapter.

Zusammenfassung

Residuelle Zirkulation in gezeitendominierten Ästuaren: Beiträge und Abhängigkeiten

Ästuarie sind komplexe Systeme, die von vielen verschiedenen Parametern und Prozessen beeinflusst werden, zum Beispiel Gezeitenströmungen von Seiten des Ozeans und Flusseinträge von Seiten des Inlands. Dementsprechend ist ästuarine Zirkulation aus vielen Beiträgen zusammengesetzt, deren Kenntnis für eine geeignete Behandlung von Ästuaren unerlässlich ist. Die Zirkulationsbeiträge und ihre Abhängigkeiten von den beeinflussenden Parametern können mithilfe numerischer hydrodynamischer Modelle untersucht werden.

Die Simulationsergebnisse machen deutlich, dass die *Tidal Straining*-Zirkulation in einem großen Bereich des Parameterraums der dominierende Beitrag ist. Diese Zirkulation entsteht aus Gezeitenasymmetrien von Schichtung und Scherung. In gezeitendominierten Ästuaren wird Schichtung im Allgemeinen von den Flutströmungen entlang des Ästuars abgebaut und von den Ebbströmungen entlang des Ästuars aufgebaut, aber sie kann auch durch Querkirkulation aufgebaut werden. In Abhängigkeit von der Querschnittsform eines Ästuars kann die Querkirkulation sogar wesentlich wirksamer im Aufbau starker Ebbschichtung sein als die Strömungen entlang des Ästuars. Somit hängen auch die *Tidal Straining*-Zirkulation und die gesamte, ästuarine Zirkulation von der Form, zum Beispiel dem Verhältnis der Tiefe zur Breite, eines Ästuars ab. Andere Parameter, deren Einfluss als wichtig identifiziert wird, sind das Verhältnis der minimalen zur maximalen Tiefe, der Salzgradient entlang des Ästuars und die Diffusivität quer zum Ästuar.

Contents

Abstract	v
Zusammenfassung	v
Preface	viii
Acknowledgements	viii
Curriculum Vitae	x
Publications	xii
Declaration of authorship	xiii
Selbstständigkeitserklärung	xiii
Explanatory notes	1
1 Introduction to estuarine circulation	2
1.1 Gravitational circulation	2
1.2 Strain-induced periodic stratification (SIPS)	3
1.3 Tidal straining circulation	3
1.4 Transverse and advectively driven circulation	4
1.5 Other contributions	5
2 Impact of the depth-to-width ratio on the residual along-channel circulation	6
2.1 Motivation	7
2.2 Theory	7
2.2.1 Basic equations	7
2.2.2 Channel geometry	9
2.2.3 Non-dimensional numbers	9
2.3 Methods	11
2.3.1 Numerical model, experiments and set-up	11
2.3.2 Prescribed parameters	11
2.3.3 Analysis and notation	12
2.4 Results and discussion	14
2.4.1 Aspect ratio and estuarine circulation	14
2.4.2 Transverse stratifying and destratifying processes	19
2.4.3 Further results and discussion	25
2.4.4 Three-dimensional approach	29
3 More on the tidal straining circulation	31
3.1 Estimation of α leading to maximum tidal straining circulation	31
3.2 Detailed investigation of the tidal straining circulation and the reduced experiments	35

3.2.1	Method: Decomposition of the tidal straining circulation	36
3.2.2	Results and discussion of the tidal straining decomposition	37
3.2.3	Interplay of momentum advection and transverse salinity advection	39
3.2.4	Gravitational and advectively driven circulation in the reduced experiments	43
4	Impact of other parameters on the residual along-channel circulation	47
4.1	Convergence and other circulation contributions	47
4.2	Impact of the quasi-lateral diffusivity	48
4.3	Impact of the minimum-to-maximum depth ratio	51
4.4	Impact of the full width at half maximum depth	54
5	Decomposition of the estuarine circulation for free surface elevation	56
5.1	Mathematical framework	56
5.1.1	Dynamic equations and boundary conditions in σ coordinates	56
5.1.2	Eulerian residual velocity	57
5.1.3	Decomposition of the total residual longitudinal circulation	59
5.1.4	Lateral terms	60
5.2	Method: Three-dimensional simulation, analysis and notation	61
5.3	Results and discussion of the estuarine circulation decomposition	62
5.4	Further results and discussion	63
6	Conclusion and outlook	66
6.1	Recapitulation	66
6.2	Applicability to reality	67
6.3	Future prospects	68
A	About the two-dimensional model	I
A.1	Alternative equation of state	I
A.2	Calculation of the channel geometry	II
A.2.1	Coefficients of the Gaussian curve	II
A.2.2	Cross-sectional area and mean depth	II
A.3	Dimensional analysis	III
A.4	Implementation of the reduced experiments	V
A.5	Further figures	VII
A.5.1	Reduced experiment F (to section 3.2.3F)	VII
A.5.2	Impact of α and S_i (to section 2.4.3.2)	VIII
B	About the three-dimensional model	IX
B.1	River discharge weighting scheme in consideration of the water depth	IX
	List of Figures	XI
	List of Tables	XII
	List of Source codes	XII

Preface

Acknowledgements

Many people supported me during my doctoral studies and my life prior to that. I want to express my deep gratitude to them - even though words do not seem to be enough.

I thank my supervisor Hans Burchard for a wonderful and challenging time. Thanks for helping me on my way into the scientific world. Thanks for all the fruitful discussions during which I never felt stupid. Thanks for letting me do things my way and for pushing me when it was necessary. I daresay I grew a lot during the last years, thanks to your everlasting support and great inspiration.

I thank Henk M. Schuttelaars for the most fantastic discussions. I enjoyed them so much and they always helped me and my work to progress. Thanks for these unforgettable experiences and for your cordial kindness.

I thank Ulf Gräwe, Johannes Becherer and Kaveh Purkiani for ongoing and imaginative discussions. I learned a lot from you, your ideas and your work. Thanks for the cool time in the hot world of tidal estuaries and numerical simulations.

I thank Lars Umlauf for helping me whenever I had questions about turbulence or other complicated things. Thanks for your uncomplicated explanations.

I thank Nikolai Kornev for challenging questions and motivating remarks. Thanks for a comprehensive introduction to Large Eddy Simulations.

I thank Huib E. de Swart for the most extraordinary lecture I have ever attended. Thanks for very many explanations concerning morphodynamic modelling. I thank Aart Kroon for instructive information on sediment transport processes. It is much to my regret that I did not do morphodynamics in the end. Thanks to both of you for a very joyful and enriching summer school.

I thank W. Rocky Geyer and Parker MacCready for an awesome summer. Thanks for everything you taught me about hydrodynamics. Thanks for being geniuses and genial at the same time.

I thank Rob D. Hetland for infecting me with Python. Thanks for introducing me to my now favourite programming language when I was new to this world.

I thank Sabine Heinzius for demanding and enjoyable English classes. Thanks for helping me to further improve my writing and communication skills.

I thank Knut Klingbeil for twenty-four/seven support with the cluster and GETM. Thanks for keeping everything running - or repairing it. I owe you hundreds of successful simulations.

I thank Peter Holtermann, Richard Hofmeister and Hannes Rennau for assisting me with any problems with Linux or GETM. Thanks for making my start with these things very easy.

I thank Eefke van der Lee for help with English and Matlab and Bianca Schippmann for help with Fortran and for many intensive discussions. Thanks to both of you for your open ears and kind, unconditional support.

I thank Berit Recklebe for straightforward administrative assistance. Thanks for making things easier and more convenient for me.

I thank all my colleagues at IOW for the very pleasant working atmosphere. Thanks for being the way you are. I will miss you.

Last but absolutely not least, I thank my family.

Ich danke meinen Eltern, Marita und Hartmut Fischer. Danke, Mama und Papa, für alles, was ihr mir gegeben und mitgegeben habt. Danke für eine wunderschöne Kindheit. Danke für eure bedingungslose Unterstützung während des gesamten Studiums. Ohne euch wäre ich nicht so leicht so weit gekommen. Danke, dass ihr immer für mich und meine kleine Familie da seid.

Ich danke meinen Geschwistern, Karl und Magdalena Fischer. Ihr habt meine Kindheit noch schöner gemacht. Danke für eure Hilfe, wenn ich sie brauchte. Danke, dass auch ihr immer für mich und meine kleine Familie da seid.

Ich danke meine Großeltern, Heinz und Walli Fischer. Auch ihr habt meine Kindheit noch schöner gemacht. Danke für eure unermüdliche Zuwendung in Form von bestem Gartenobst und -gemüse und leckeren Marmeladen.

Ich danke meinem Mann, Gunnar Schulz. Danke, mein Herz, für dein Verständnis und deine Hilfe, vor Allem in den letzten Monaten und Wochen. Merci beaucoup pour la France. Ohne deinen Rückhalt könnte ich das nicht.

Ich danke meinen Schwiegereltern, Karin und Gerhardt Schulz. Danke, dass ihr mich so herzlich in eure Familie aufgenommen habt. Danke für euer gewachsenes Verständnis für mich und meine Arbeit. Danke für schöne und erholsame Ferien.

Ich danke meinen Kindern, Florian und Alexander Schulz. Ihr bereichert mein Leben unendlich. Danke, ihr lieben kleinen Engel, für alles an euch.

Regarding the publication (Chapter 2)

The studies of Elisabeth Schulz have been funded by a scholarship from the University of Rostock, Interdisciplinary Faculty, Department Maritime Systems.

The work of Henk M. Schuttelaars has been supported by a visiting scientist grant through the Leibniz Institute for Baltic Sea Research Warnemünde.

Ulf Gräwe has been funded by the German Federal Ministry of Research and Education (BMBF) in the framework of the project PACE (The future of the Wadden Sea sediment fluxes: still keeping pace with sea level rise?, FKZ 03F0634A).

The work of Hans Burchard has been carried out in the framework of the project ECOWS (Role of Estuarine Circulation for Transport of Suspended Particulate Matter in the Wadden Sea) funded by the German Research Foundation (DFG, project BU1199/11).

We thank Lars Umlauf (Leibniz Institute for Baltic Sea Research Warnemünde, Rostock, Germany) for valuable discussions and hints.

The authors are furthermore grateful to the two anonymous reviewers, whose remarks and suggestions helped to greatly improve this paper.

Curriculum Vitae

Research experience

- Nov. 2009 – Oct. 2014 **PhD scholarship student & scientific employee**, *Leibniz Institute for Baltic Sea Research Warnemünde (IOW), Department of Physical Oceanography and Instrumentation*, Rostock, Germany.
supervisor: Prof. Dr. Hans Burchard
- Jan.–Nov. 2009 **scientific employee**, *IOW, Dept. Phys. Ocean.*, Rostock, Germany.
supervisor: PD Dr. habil. Gerald Schernewski
project: *GENeric European Sustainable Information Space for environment (GEN-ESIS)*
tasks: implementation of curvilinear coordinates into the Lagrangian particle tracking model GITM, realistic GETM simulations of the Oder estuary and according particle tracking simulations (particles represent bacteria), assessment of the ecological water quality; project management, writing of project reports
- Oct. 2007 – Jan. 2009 **student research assistant**, *IOW, Dept. Phys. Ocean.*, Rostock, Germany.
supervisor: Prof. Dr. Hans Burchard
project: *European COastal-shelf sea OPerational observing and forecasting system (ECOOP)*
tasks: Please be referred to the section *Diplom thesis*.
- Mar.–Apr. 2008 **student research assistant**, *IOW, research vessel Alkor*, Bornholm Basin, Baltic.
supervisor: Dr. Lars Umlauf (now PD Dr. habil.)
tasks: ADCP and microstructure measurements in shift work
- Feb.–Mar. 2007 **student intern**, *Alfred Wegener Institute (AWI) for Polar and Marine Research, Research Division of Climate Sciences*, Bremerhaven, Germany.
supervisor: Dr. Gerit Birnbaum
tasks: data analysis of precipitation and strong-wind events at the Kohnen station (Dronning Maud Land, Antarctica), processing of digital satellite images by means of the TeraVision software, graphical evaluation of weather forecasts
- 2004–2006 further student assistant jobs at the *University of Rostock*, Rostock, Germany

Teaching

- Oct. 2013 – Feb. 2014, Oct.–Dec. 2014 **Coastal ocean processes**, *University of Rostock*, Rostock, Germany.
tasks: supervision of exercise lessons, correction of students' assignments and examinations

Summer and winter schools

- June–July 2014 **Coastal and estuarine morphodynamics**, *Skallingen Laboratory, University of Copenhagen*, Ho-Blåvand, Denmark.
 (9 days) organisers: Dr. Aart Kroon, Prof. Dr. Huib E. de Swart
 homepage: news.imau.nl/?p=1676
- Feb. 2014 **Modelling mixing and transport in lakes, harbors and estuaries**, *The Abdus Salam International Centre for Theoretical Physics*, Trieste, Italy.
 (3 days) organisers: Dr. Joseph J. Niemela, Prof. Dr. Vincenzo Armenio
 homepage: www.dicar.units.it/dia/eventi/Evento.asp?ide=1
- Sept. 2011 **Physics of the ocean**, *Physikzentrum Bad Honnef*, Bad Honnef, Germany.
 (5 days) organisers: Prof. Dr. Martin Visbeck, Prof. Dr. Wolfgang Roether
 homepage: www.pbh.de/en/aktuelles/S211.html
- July–Aug. 2009 **Estuarine and coastal fluid dynamics**, *Friday Harbor Laboratories, University of Washington*, Friday Harbor, San Juan Island, WA, USA.
 (5 weeks) instructors: Ph.D. W. Rockwell Geyer, Prof. Dr. Parker MacCready
 homepage: faculty.washington.edu/pmacc/Classes/FHL_2009/ecfd2009.html

Education

- Jan. 2009 **Diplom of physics (Dipl.-Phys.)**, *University of Rostock & Leibniz Institute for Baltic Sea Research Warnemünde*, Rostock, Germany.
 grade: 1.2 (“outstanding”)
- Sept. 2005 **Vordiplom of physics**, *University of Rostock*, Rostock, Germany.
 grade: 1.5 (“outstanding”)
- June 2003 **Abitur**, *Gymnasium Große Stadtschule Rostock*, Rostock, Germany.
 grade: 1.7 (“good”)
 advanced courses: mathematics, English

Diplom thesis

- title *Turbulent kinetic energy dissipation rate in the Rhine region of freshwater influence*
- supervisor Prof. Dr. Hans Burchard
- summary Measurements of the TKE dissipation rate in the Rhine ROFI had revealed a maximum in the upper half of the water column around high water (max. along-shore currents), which could not be explained. By means of idealised three-dimensional simulations using GETM, I found that they are caused by high shear when the fore- and the back-front of the freshwater plume transit the water column.
- grade 1.0 (“outstanding”)

Publications

1. Fischer, E., H. Burchard, and R. D. Hetland, 2009: Numerical investigations of the turbulent kinetic energy dissipation rate in the Rhine region of freshwater influence. *Ocean Dyn.*, **59**, 629–641, doi:10.1007/s10236-009-0187-4.
2. Birnbaum, G., J. Freitag, R. Brauner, G. König-Langlo, E. Schulz, S. Kipfstuhl, H. Oerter, C. H. Reijmer, E. Schlosser, S. H. Faria, H. Ries, B. Loose, A. Herber, M. G. Duda, J. G. Powers, K. W. Manning, and M. R. van den Broeke, 2010: Strong-wind events and their influence on the formation of snow dunes: observations from Kohnen station, Dronning Maud Land, Antarctica. *J. Glaciol.*, **56**, 891–902, doi:10.3189/002214310794457272.
3. Burchard, H., R. D. Hetland, E. Schulz, and H. M. Schuttelaars, 2011: Drivers of residual estuarine circulation in tidally energetic estuaries: straight and irrotational channels with parabolic cross section. *J. Phys. Oceanogr.*, **41**, 548–570, doi:10.1175/2010jpo4453.1.
4. Schernewski, G., E. Fischer, T. Huttula, G. Jost, and M. Ras, 2012: Model tools to support bathing water quality management: *Escherichia coli* bacteria in a Baltic lagoon. *Journal of Coastal Conservation*, **16**, 473–488, doi:10.1007/s11852-012-0202-7.
5. Burchard, H., E. Schulz, and H. M. Schuttelaars, 2014: Impact of estuarine convergence on residual circulation in tidally energetic estuaries and inlets. *Geophysical Research Letters*, **41**, 913–919, doi:10.1002/2013GL058494.
6. Schulz, E., H. Burchard, and H. M. Schuttelaars, 2014: Impact of the depth-to-width ratio of periodically stratified tidal channels on the estuarine circulation. *J. Phys. Oceanogr.*, under review.

Declaration of authorship

I hereby declare on oath that I wrote the thesis at hand self-dependently and without help by others. To this, I used only those auxiliary means and resources which I stated and I indicated all passages taken from these resources, literally or with regard to contents, accordingly.

Selbstständigkeitserklärung

Ich versichere hiermit an Eides statt, dass ich die vorliegende Arbeit selbstständig angefertigt und ohne fremde Hilfe verfasst habe. Dazu habe ich keine außer den von mir angegebenen Hilfsmitteln und Quellen verwendet und die den benutzten Werken inhaltlich und wörtlich entnommenen Stellen habe ich als solche kenntlich gemacht.

(Erklärung wörtlich entnommen aus <http://www.uni-rostock.de/fileadmin/UniHome/Gremien/Promotion/erklaerung-mnf-rostock-netz.pdf>)

Rostock, 14.10.2014

Explanatory notes

The reader interested in the main results of this work is referred to chapter 2. That chapter corresponds to a large extent with a manuscript submitted to the *Journal of Physical Oceanography*.

The authors of that manuscript are Elisabeth Schulz¹, Henk M. Schuttelaars², Ulf Gräwe¹ and Hans Burchard¹ from the institutions listed below. Simulations, analyses and writing were done by E. Schulz except for the particle tracking simulations (Fig. 2.6, U. Gräwe).

After acceptance, the publication will be available here:

<http://journals.ametsoc.org/loi/phoc>

The mathematical framework for decomposing estuarine residual currents into dynamic components (sections 2.3.3, 5.1) was developed by Elisabeth Schulz¹, Robert D. Hetland³, Henk M. Schuttelaars² and Hans Burchard¹.

The river discharge weighting scheme in consideration of the river cells' water depth (appendix B.1) was the idea of Elisabeth Schulz¹ and implemented into GETM with support from Knut Klingbeil¹.

1. Leibniz Institute for Baltic Sea Research Warnemünde, Rostock, Germany
2. Delft Institute of Applied Mathematics, Delft University of Technology, Delft, The Netherlands
3. Department of Oceanography, Texas A&M University, College Station, Texas, USA

Chapter 1

Introduction to estuarine circulation

An estuary is a body of flowing water affected by riverine freshwater from one side and oceanic saltwater from the other side. The corresponding density difference drives a gravitational circulation (1.1). Against former assumptions, this circulation is not always the dominant, let alone the only contribution to the total estuarine circulation. E.g., in tidal estuaries, tidal straining can play an important role (1.3). Further relevant effects are differential advection (1.4) and, as the case may be, Earth rotation (Coriolis force), wind shear stress, channel curvature and asymmetry of the depth profile.

The flow in a tidal estuary is not steady, but it varies over the tidal cycle so that the residual, estuarine circulation is of interest, e.g. for the residual transport of suspended particulate matter (SPM). (It should be noted that the covariance of tidal current velocity and SPM concentration may be more important, depending on the SPM properties, see Burchard et al. 2013).

1.1. Gravitational circulation

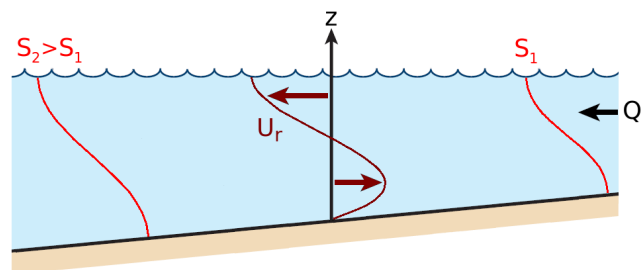


Figure 1.1.: Schematic of gravitational circulation (adapted from Simpson et al. 1990; MacCready and Geyer 2010).

The circulation in tidal estuaries has been investigated for more than half a century, but the driving mechanisms are still not fully understood. In the beginning, only the *gravitational* (also called gravity-, density- or buoyancy-driven) *circulation* was considered (e.g. Pritchard 1952; Agnew 1960; Hansen and Rattray 1965): The salinity (and thus density) decrease from the ocean toward the riverine freshwater reach induces an up-estuary baroclinic pressure gradient force which increases from surface to bottom. The down-estuary barotropic pressure gradient force is vertically constant.

Combined, these forces drive an up-estuary bottom flow of saline water and a down-estuary surface flow of fresher water (Fig. 1.1). This is the *classical estuarine circulation*.

1.2. Strain-induced periodic stratification (SIPS)

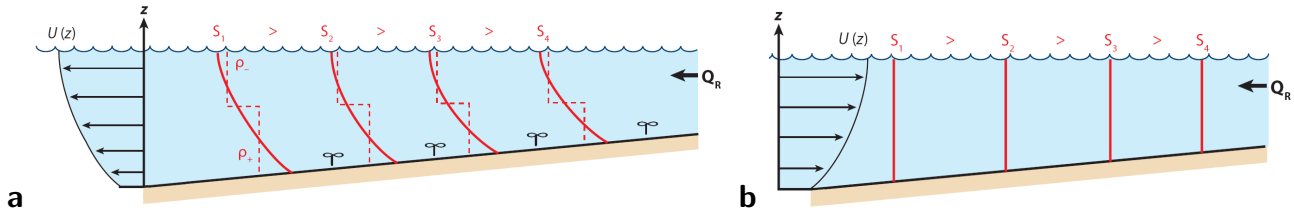


Figure 1.2.: Schematic of strain-induced periodic stratification (SIPS; adapted from Simpson et al. 1990; MacCready and Geyer 2010). **a** Ebb shear and stratification; **b** flood shear and destratification.

Linden and Simpson (1988) and Simpson et al. (1990) discovered the stratifying and destratifying effect of the vertically sheared ebb and flood current in the presence of a longitudinal (along-channel, axial) salinity gradient: Since the absolute velocity increases with the distance from the bottom, the ebb current transports fresher over more saline water, resulting in a stably stratified water column (Fig. 1.2a), and the flood current reduces or completely erases this stratification (b). Simpson et al. (1990) called this process *strain-induced periodic stratification (SIPS)* and described its dependency on the horizontal gradient Richardson number, now called *Simpson number* (Burchard et al. 2011).

1.3. Tidal straining circulation

Even though it was already known that stratification suppresses turbulence (Linden 1979, 1980) and understood how turbulent mixing reduces the intensity of a density-driven flow (Linden and Simpson 1986), it took some time before the feedback of SIPS on the tidal currents was recognised: Jay and Musiak (1994, 1996) explained how stratification during ebb decreases the eddy viscosity and thus allows stronger shear, i.e. surface-enhanced ebb currents, and how a homogeneous water column during flood increases the eddy viscosity and thus prohibits strong flood shear, i.e. leads to bottom-enhanced flood currents (Fig. 1.3). The residual (tidally averaged, subtidal) circulation contribution resulting from this tidal asymmetry of eddy viscosity and shear has the same orientation as the classical estuarine circulation and is called *tidal straining circulation* (Burchard et al. 2011; Geyer and MacCready 2014).

One- and two-dimensional model studies (Burchard and Hetland 2010; Burchard et al. 2011) revealed that this is the dominant circulation contribution in periodically stratified estuaries. The first field observations of tidal straining circulation in tidally energetic, weakly stratified channels (Becherer et al. 2011) supported these results. Current measurements (Stacey et al. 2001) and simulations (Burchard et al. 2011) also showed that the tidal straining circulation can reverse, i.e. oppose the orientation of the classical estuarine circulation, when stratification is strong during flood (by lateral straining, see next section).

A classical longitudinal salinity gradient provided (salinity decreasing in the up-estuary direction), down-estuary shear and stratification enforce each other until the flow becomes unstable, i.e. the instantaneous local gradient Richardson number, $Ri = N^2/S^2$, falls below the critical value of 0.25

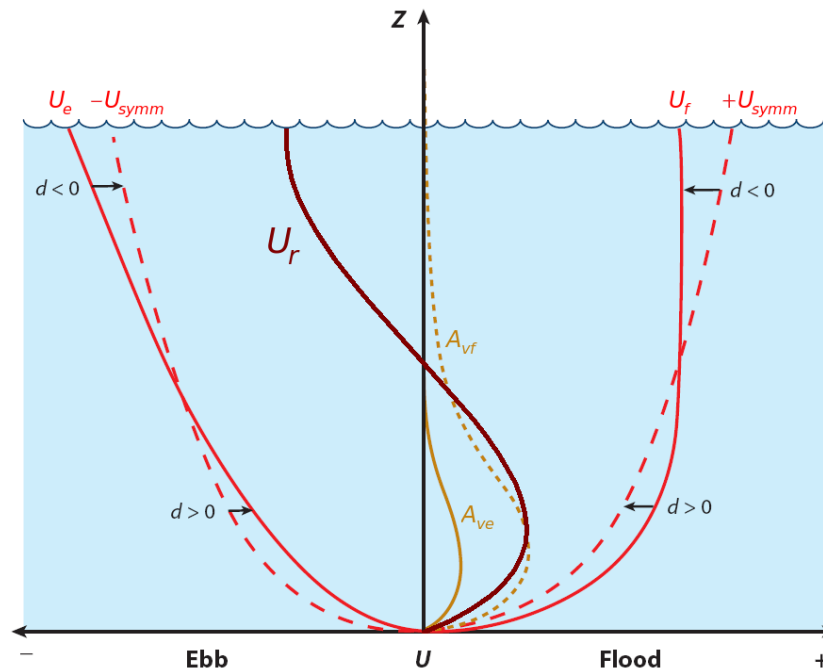


Figure 1.3.: Schematic of tidally asymmetric eddy viscosity and shear and of tidal straining circulation (adapted from Jay and Musiak 1994, 1996; MacCready and Geyer 2010).

($N^2 = -g/\rho_0 \cdot \partial\rho/\partial z$ Brunt-Väisälä or buoyancy frequency, $S^2 = (\partial u/\partial z)^2 + (\partial v/\partial z)^2$ shear squared; Kundu and Cohen 2002).

1.4. Transverse and advectively driven circulation

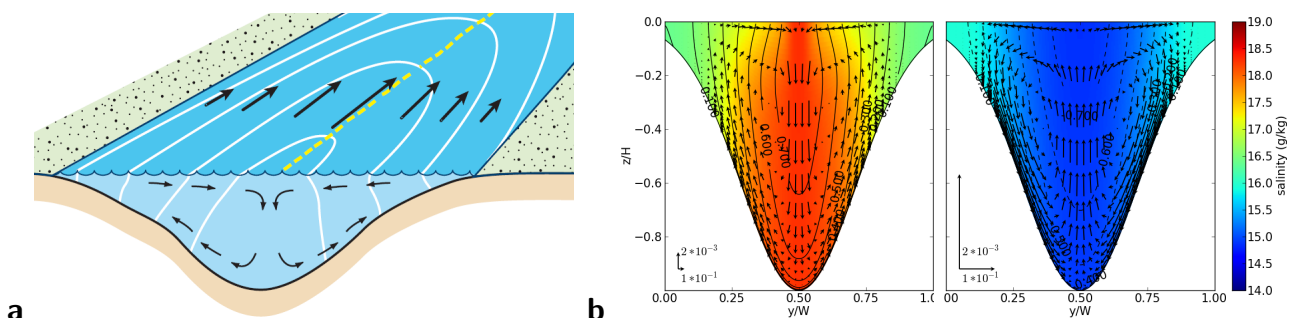


Figure 1.4.: a Schematic of laterally differential longitudinal advection (straight arrows at surface) during flood and the resulting lateral salinity gradient (white lines are isohalines) and surface-convergent transverse circulation (arrows in cross-sectional plane) (MacCready and Geyer 2010).

b Simulation results of salinity (colour), longitudinal velocity (contours) and lateral and vertical velocities (arrows) shortly before full flood (left) and full ebb (right) (cp. Fig. 2.5).

The existence of *transverse* (cross-sectional, secondary) *circulation* was first postulated by Smith (1976) and confirmed by observations of surface convergence during flood (e.g. Nunes and Simpson 1985). It was attributed to bathymetry-induced lateral (across-channel) shear of the longitudinal tidal current (faster above deep channel) leading to lateral salinity gradients which generate a trans-

verse gravitational circulation. Lerczak and Geyer (2004) described the effect of *differential advection of along-channel density gradients* and the resulting transverse circulation on the longitudinal momentum and circulation. To clearly indicate the mechanism driving these circulations, we refer to it as *laterally differential longitudinal advection (of salinity)*.

During flood, the salinity increases from the shoals to the thalweg (deepest channel) so that the transverse circulation is surface-convergent (Fig. 1.4). This is called *flood-oriented transverse circulation* (Burchard et al. 2011). It advects high longitudinal momentum from the surface centre downward and low momentum from the shoals toward the thalweg, at the surface, which leads to bottom-enhanced flood currents. During ebb, the salinity decreases from the shoals to the thalweg so that the transverse circulation is surface-divergent. This is called *ebb-oriented transverse circulation*. It advects high momentum from the surface centre toward the shoals and low momentum from the shoals toward the thalweg, at the bottom, which leads to surface-enhanced ebb currents. The residual longitudinal circulation contribution resulting from this tidally asymmetric shear also has the same orientation as the classical estuarine circulation and is called *advectively driven circulation* (Burchard et al. 2011).

Measurements (e.g. Stacey et al. 2001; Lacy et al. 2003; Becherer et al. 2011; Scully and Geyer 2012; Becherer et al. 2014; Purkiani et al. 2014) and numerical studies (Scully et al. 2009; Purkiani et al. 2014) revealed that transverse circulation can also induce stratification and that this *lateral straining* process is more important during stronger mixing conditions (flood, spring tide). Thus, stratification can be stronger during flood than during ebb, which is contrary to the longitudinal straining (SIPS, see section 1.2).

1.5. Other contributions

Field observations and model results (Valle-Levinson et al. 2000; Valle-Levinson 2008; Huijts et al. 2011) showed that transverse circulation and lateral convergence can also result from Coriolis deflection of the longitudinal tidal currents, i.e. transverse circulation does not require (but may be enhanced by) salinity gradients. Yet another lateral effect is related to turbulent mixing being constantly high above the shoals and periodic above the channel (Scully and Friedrichs 2007). This gradient increases the phase lag between shoals and channel particularly around slack after ebb and drives a laterally sheared residual longitudinal circulation with up-estuary flow above the shoals and down-estuary flow above the channel.

Further possible contributions to the estuarine circulation arise from channel convergence (e.g. Ianniello 1979; Burchard et al. 2014), curvature (Geyer 1993; Chant 2002; Becherer et al. 2014), wind (Scully et al. 2005; Waterhouse et al. 2013) and trapping due to complex geometry (Lacy et al. 2003; Giddings et al. 2012).

The reviews by MacCready and Geyer (2010) and Geyer and MacCready (2014) contain comprehensive summaries of estuarine circulation processes.

Chapter 2

Impact of the depth-to-width ratio of a tidally energetic estuary on the residual along-channel circulation

Abstract The dependency of the estuarine circulation on the depth-to-width ratio of a periodically stratified tidal estuary is systematically investigated here for the first time. Currents, salinity and other properties are simulated by means of the General Estuarine Transport Model (GETM) in cross-sectional slice mode, applying a symmetric Gaussian-shaped depth profile. The width is varied over four orders of magnitude. The individual along-channel circulation contributions from tidal straining, gravitation, advection etc. are calculated and the impact of the depth-to-width ratio on their intensity is presented and elucidated.

It is found that the estuarine circulation exhibits a distinct maximum in medium wide channels, which is caused by a maximum of the tidal straining contribution. This maximum is related to a strong tidal asymmetry of eddy viscosity and shear created by secondary strain-induced periodic stratification (2SIPS): In medium channels, transverse circulation generated by lateral density gradients due to laterally differential longitudinal advection induces stable stratification at the end of the flood phase, which is further increased during ebb by longitudinal straining (SIPS). Thus, eddy viscosity is low and shear is strong in the entire ebb phase. During flood, SIPS decreases the stratification so that eddy viscosity is high and shear is weak. The circulation resulting from this viscosity-shear correlation, the tidal straining circulation, is oriented like the classical, gravitational circulation, with riverine outflow at the surface and oceanic inflow close to the bottom. In medium channels, it is about five times as strong as in wide (quasi-one-dimensional) channels, in which 2SIPS is negligible.

This chapter is structured as follows: The first section describes the novelty of this study. Section 2.2 introduces the theoretical background, the channel geometry and non-dimensional numbers. The following section explains the two-dimensional numerical model, the parameters and the analysis of the model output. Then the results are presented and discussed: Section 2.4.1 describes the impact of the aspect ratio on the estuarine circulation, particularly the tidal straining contribution, and on the eddy viscosity and the stratification; section 2.4.2 clarifies the role of lateral and vertical straining and advection for the stratification; section 2.4.3 substantiates the results by means of additional experiments and simulations; section 2.4.4 introduces a three-dimensional model used to further confirm the results of the two-dimensional model. In the conclusion, the 2SIPS process and

its influence on the longitudinal tidal straining circulation in dependency on the aspect ratio are summarised.

2.1. Motivation

Lerczak and Geyer (2004) suggested that lateral effects would be stronger in narrower estuaries and recommended further studies to investigate the interaction of the transverse and the longitudinal circulation and the salinity field. Simulations with three different widths (Burchard et al. 2011) could not strongly confirm this assumption but revealed a clear dependency of the tidal straining circulation (and thus the total, estuarine circulation) on the width, with the intensity increasing with the width.

The numerical study presented here provides the first systematic investigation of the impact of the aspect ratio (depth-to-width ratio) on the estuarine circulation. It spans four orders of magnitude of the aspect ratio and shows that the dependency described by Burchard et al. (2011) holds only for narrow and medium wide estuaries (aspect ratio $\gtrsim 0.004$, depending on other parameters, see section 2.4.1.1). It reveals that for wider estuaries, the intensity of the dominant, tidal straining circulation decreases with the width, i.e. the estuarine circulation is *maximum for a certain aspect ratio*, a phenomenon we explain here.

Lerczak and Geyer (2004) described how the transverse circulation advects the salinity, together with the longitudinal momentum, and numerous observations revealed its stratifying effect (lateral straining, see section 1.4). While the feedback of the momentum advection on the estuarine circulation was recognised (advectively driven circulation), the feedback of the stratification, via the interaction with eddy viscosity and shear (tidal straining circulation), was not considered.

Our study shows that lateral straining ($\partial_z v \partial_y S$) can lead to stratification during or at the end of flood, depending on the aspect ratio. This has far-reaching consequences for the stratification during ebb, the tidal asymmetry and the estuarine circulation. We suggest to call this process *secondary strain-induced periodic stratification (2SIPS)*.

2.2. Theory

2.2.1. Basic equations

We assume an infinitely long, longitudinally uniform, straight, irrotational estuary (Fig. 2.1a) and use the hydrostatic dynamic equations and the salinity budget equation as given in Burchard et al. (2011):

The hydrostatic dynamic equations along (x , u) and across (y , v) the estuary can be written as follows:

$$\partial_t u + v \partial_y u + w \partial_z u - \partial_z (A_z \partial_z u) - \partial_{y*} (A_{y*} \partial_{y*} u) = \int_z^0 [\partial_x b] d\hat{z} - [P_x], \quad (2.1)$$

$$\partial_t v + v \partial_y v + w \partial_z v - \partial_z (A_z \partial_z v) - \partial_{y*} (A_{y*} \partial_{y*} v) = \int_z^0 \partial_y b d\hat{z} - P_y. \quad (2.2)$$

∂_{y*} is the quasi-horizontal partial derivative along σ layers and P the barotropic pressure gradient in the given direction. Here, square brackets, $[\cdot]$, are used to denote prescribed variables.

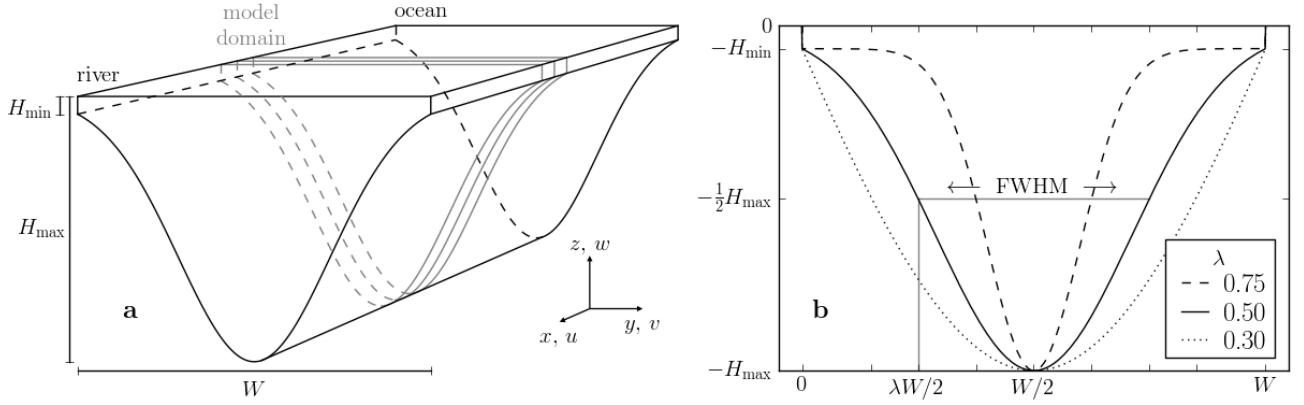


Figure 2.1.: **a** Schematic of the model domain and its orientation; **b** Gaussian depth profiles for different λ (2.10).

The budget equation for the salinity is

$$\partial_t S + u[\partial_x S] + v\partial_y S + w\partial_z S - \partial_z(K_z\partial_z S) - \partial_{y*}(K_{y*}\partial_{y*} S) = 0, \quad (2.3)$$

with $K_z(y, z, t)$ the vertical eddy diffusivity.

The longitudinal barotropic pressure gradient is calculated in such a way that the cross-sectionally averaged longitudinal velocity, $\bar{u}(t)$, equals a prescribed M_2 tidal current,

$$\bar{u}(t) = \frac{1}{A} \int_A u(y, z, t) d\hat{A} = U_t \sin(\omega t), \quad (2.4)$$

with A the cross-sectional area, U_t the prescribed cross-sectionally averaged M_2 velocity amplitude, $\omega = 2\pi/T$ the circular frequency and $T = 44714$ s the periodic time of the M_2 tidal current.

Note that river discharge is ignored here. Looking into tidal inlet systems such as those in the Wadden Sea, non-zero discharge does not play an important role. A horizontal density gradient can also be established with zero discharge, e.g. by differential heating (Burchard et al. 2008).

The lateral barotropic pressure gradient is calculated in such a way that the surface elevation is constant, $\eta(y, t) = 0$ (rigid lid, $\int_{-H}^0 v dz = 0$, see Burchard et al. 2011). It should be noted that this does not mean zero lateral barotropic pressure gradients.

The results and sensitivities to parameters obtained with the simplified two-dimensional model (more details in section 2.3.1) are in qualitative agreement with those obtained with a three-dimensional model (section 2.4.4).

We use a simplified equation of state (MacCready and Geyer 2010; Geyer and MacCready 2014):

$$\rho = \rho_0(1 + \beta S), \quad (2.5)$$

with $\rho(y, z, t)$ the density, $\rho_0 = 1025 \text{ kg m}^{-3}$ the reference density, $\beta = 7.8 \cdot 10^{-4} \text{ psu}^{-1}$ the haline contractivity and $S(y, z, t)$ the salinity. Thus, the buoyancy,

$$b = -g(\rho - \rho_0)/\rho_0, \quad (2.6)$$

with g the gravitational acceleration, becomes

$$b = -g\beta S. \quad (2.7)$$

2.2.2. Channel geometry

For the depth profile we choose a Gaussian curve (Fig. 2.1),

$$H(y) = c_1 + c_2 \exp(-c_3\{y - W/2\}^2), \quad (2.8)$$

with W the prescribed channel width. The coefficients, c_1 , c_2 and c_3 , are determined by the following conditions:

$$\begin{aligned} H(0) = H(W) &= H_{\min} < H_{\max}/2, \\ H(W/2) &= H_{\max}, \\ H(\lambda W/2) &= H_{\max}/2, \end{aligned} \quad (2.9)$$

with H_{\min} and H_{\max} the prescribed minimum and maximum depth at the shores ($y = 0, W$) and the thalweg ($y = W/2$), respectively. The parameter λ is related to the prescribed full width at half maximum depth (FWHM, Fig. 2.1b):

$$W = \lambda W + \text{FWHM}, \quad (2.10)$$

where λ equals the fraction of the channel width with $H(y) \leq H_{\max}/2$ and thus determines the steepness of the channel slopes, together with H_{\min} and the aspect ratio (2.14).

2.2.3. Non-dimensional numbers

The system described above is characterised by the nine dimensional parameters numbered in Tab. 2.1. These parameters involve two dimensions (length (m) and time (s)) so that the system is well-defined by seven linearly independent non-dimensional numbers ($9 - 2 = 7$; e.g. Buckingham 1914; Kalagnanam et al. 1994). A possible and in parts commonly used set is that given in Tab. 2.1.

The Simpson number is also known as horizontal Richardson number; the unsteadiness number is also known as Stokes number (Souza 2013) or inverse Strouhal number (Burchard et al. 2011 and references therein). Their dynamic impact and that of the non-dimensional bottom roughness length were systematically investigated in previous studies (Burchard and Hetland 2010; Burchard et al. 2011). These studies used the average water depth as length scale, $H = H_{\text{mean}}$, but here we choose the maximum water depth, $H = H_{\max}$, which is independent of the channel shape.

Preliminary tests for the study presented here showed a dependency on the non-dimensional quasi-lateral diffusivities of momentum and salinity, $\tilde{A}_{y*} = \tilde{K}_{y*}$, which we define by scaling with the channel width, W , and the root mean square (RMS) friction velocity scale, U_* ,

$$\tilde{A}_{y*} = A_{y*}/(WU_*). \quad (2.11)$$

It should be noted that the estuarine circulation decreases with increasing \tilde{A}_{y*} . This hints at the

dimensional parameters			values / ranges
1 ○ ★	W	width (surface)	$100 - 10^6$ m
2 ○ ★	$\text{FWHM} = (1 - \lambda)W$	full width at half maximum depth	$50 - 0.5 \cdot 10^6$ m
3 ○	H_{\max}	maximum water depth (thalweg)	15 m
4 ○	H_{\min}	minimum water depth (shoals)	1 m
	$H_{\text{mean}} = 1/W \int_0^W H(y) dy$	mean water depth	7.8 m
5 ○	z_0^b	bottom roughness length	0.001 m
	T	M_2 tidal period	44714 s
6	$\omega = 2\pi/T$	M_2 tidal frequency	$1.4 \cdot 10^{-4} \text{ s}^{-1}$
	$\partial_x S$	longitudinal salinity gradient	$-3 \cdot 10^{-4} \text{ psu m}^{-1}$
7	$\partial_x b = -g\beta\partial_x S$	longitudinal buoyancy gradient	$2.3 \cdot 10^{-6} \text{ s}^{-2}$
	U_t	cross-sectionally averaged M_2 velocity amplitude	1 m s^{-1}
8	$U_* = U_t \sqrt{C_D/2}$	root mean square (RMS) friction velocity scale	0.033 m s^{-1}
9 ○ ★	$A_{y*} = \tilde{A}_{y*} W U_*$	quasi-lateral eddy diffusivity along σ layers	$0.069 - 693 \text{ m}^2 \text{ s}^{-1}$
non-dimensional numbers			values / range
1	$\text{Si} = \partial_x b H_{\max}^2 / U_*^2$	Simpson number	0.48
2	$\text{Un} = \omega H_{\max} / U_*$	unsteadiness number	0.064
3	$\tilde{z}_0^b = z_0^b / H_{\max}$	non-dimensional bottom roughness length	$6.7 \cdot 10^{-5}$
4	\tilde{A}_{y*}	non-dimensional quasi-lateral eddy diffusivity	0.021
5	λ	fraction of W with $H(y) \leq H_{\max}/2$	0.5
6	$\tilde{H}_{\min} = H_{\min} / H_{\max}$	minimum-to-maximum depth ratio	0.067
7 ★	$\alpha = H_{\max} / W$	aspect ratio, depth-to-width ratio	$1.5 \cdot 10^{-5} - 0.15$
	$C_D = \kappa^2 / \{(1 + \tilde{z}_0^b) \ln(1 + 1/\tilde{z}_0^b) - 1\}^2$	drag coefficient	$2.2 \cdot 10^{-3}$

Table 2.1.: Dimensional parameters and non-dimensional numbers with their reference values or variation ranges. The numerals in the first column indicate the system-characterising nine parameters and seven linearly independent non-dimensional numbers. The circles mark model input. The stars mark varied parameters and numbers; others are invariant. Parameters and numbers without an equation are directly prescribed; others are calculated. σ is the bottom-following coordinate, $\sigma(y, z) = z/H(y)$; $\kappa = 0.4$ is the von Kármán constant.

Note that the quasi-lateral diffusivity of salinity here equals that of momentum, $K_{y*} = A_{y*}$ and $\tilde{K}_{y*} = \tilde{A}_{y*}$.

importance of lateral processes but is not further investigated here (see section 4.2).

The remaining three non-dimensional numbers describe the channel shape (also see section 2.2.2 and Fig. 2.1b):

$$\lambda = 1 - \text{FWHM}/W, \quad (2.12)$$

$$\tilde{H}_{\min} = H_{\min}/H_{\max}, \quad (2.13)$$

$$\alpha = H_{\max}/W. \quad (2.14)$$

The focus of our study is on the impact of the aspect ratio, α , on the estuarine circulation and its contributions. (The impact of \tilde{H}_{\min} and λ is described in sections 4.3 and 4.4.)

2.3. Methods

2.3.1. Numerical model, experiments and set-up

The dimensional equations are solved numerically by means of the three-dimensional General Estuarine Transport Model (GETM, <http://www.getm.eu>) incorporating a two-equation k - ε turbulence closure model (General Ocean Turbulence Model, GOTM, <http://www.gotm.net>). See Burchard et al. (2011) for details on the two-dimensional mode of GETM, i.e. the y - z slice model with vanishing longitudinal gradients except for the baroclinic and the barotropic pressure gradients.

In order to investigate the importance of transverse advection of momentum and salinity for the longitudinal circulation, we carry out further experiments with reduced physics, in addition to the reference experiment, A: full physics, which uses the full equations (2.1)-(2.3). The reduced experiments are implemented as follows (also see appendix A.4):

C: no momentum advection,

$$v\partial_y u = w\partial_z u = 0 \text{ in (2.1) and } v\partial_y v = w\partial_z v = 0 \text{ in (2.2);}$$

D: no lateral internal pressure gradient, i.e. no transverse circulation,

$$\partial_y b = 0 \text{ in (2.2);}$$

F: no transverse salinity advection,

$$v\partial_y S = w\partial_z S = 0 \text{ in (2.3).}$$

Experiments C and D have already been carried out by Burchard and Schuttelaars (2012); experiment F is new. (It should be noted that we do not call it B or E in order to avoid confusion with Burchard and Schuttelaars (2012).)

The domain of the cross-sectional slice model is shown in Fig. 2.1a. The model domain lies in the y - z plane and has a lateral resolution of 200 cells and a vertical resolution of 100 σ layers with zooming toward the bottom. The surface elevation is constant, $\eta(y, t) = 0$ (rigid lid).

The model is forced by a constant baroclinic pressure gradient and a periodic barotropic pressure gradient (2.4). The computational time step is $\Delta t = T/20000 \approx 2.2$ s except for very narrow channels, for which numerical stability requires $\Delta t = T/40000 \approx 1.1$ s ($W \leq 300$ m) or even $\Delta t = T/80000 \approx 0.6$ s ($W \leq 100$ m). The model is started from rest at slack after ebb and run for ten tidal cycles to ensure periodicity.

It should be noted that we tested the periodicity as well as the influence of the starting point. If started at slack after flood, the model gives the same results except for an expectable offset in salinity and thus density and buoyancy.

2.3.2. Prescribed parameters

The invariant parameters are prescribed with the reference values listed in Tab. 2.1 unless otherwise noted. They yield the non-dimensional numbers also listed in Tab. 2.1, e.g. the Simpson number $Si = 0.48$ and the unsteadiness number $Un = 0.064$.

For comparison, applying the average water depth and the amplitude of the friction velocity ($U_{*,amp} = \sqrt{2}U_* = U_t\sqrt{C_D}$) leads to $Si = 0.066$ and $Un = 0.024$ and applying the average water depth and the RMS friction velocity leads to $Si = 0.13$ and $Un = 0.034$. The latter calculation is

in agreement with Burchard et al. (2013) and our values compare well to those given for the York River during spring tide or the Western Scheldt (their Tab. 1).

In this contribution, we focus on variation of the width with $100 \text{ m} \leq W \leq 10^6 \text{ m}$, yielding the aspect ratio $0.15 \geq \alpha \geq 1.5 \cdot 10^{-5}$, i.e. spanning four orders of magnitude. This parameter range is investigated with about 60 simulations.

Please note that not the entire α range can be found in reality, but it is used here to also cover marginal phenomena, e.g. to show the (transition to) quasi-one-dimensional behaviour of wide estuaries. Aspect ratios of several real estuaries are listed in Tab. 2.2 for comparison.

	estuary	α	H (m)	W (km)	reference
wide	Delaware, estuary mouth	$1.5 \cdot 10^{-4}$	6.1	40	van Rijn 2011
	Hooghly, estuary mouth	$3.2 \cdot 10^{-4}$	7	22	van Rijn 2011
	Western Scheldt, estuary mouth	$4.0 \cdot 10^{-4}$	10	25	van Rijn 2011
medium	York River, near Clay Bank	$3.3 \cdot 10^{-3}$	10	3	Scully and Friedrichs 2007
	Willapa Bay, Stanley Channel	$6.7 \cdot 10^{-3}$	20	3	Banas and Hickey 2005
	Hudson River, 6 km south of George Washington Bridge	$1.3 \cdot 10^{-2}$	15	1.2	Peters 1997
narrow	Schillbalje (tidal gat southwest of Wadden Sea island Spiekeroog)	$1.5 \cdot 10^{-2}$	15	1	Becherer et al. 2014
	Fraser River	$1.5 \cdot 10^{-2}$	12	0.8	Geyer and Smith 1987
	San Francisco Bay, Suisun Cutoff	$2.4 \cdot 10^{-2}$	12	0.5	Stacey et al. 1999
	St. Augustine Inlet	$2.7 \cdot 10^{-2}$	15	0.55	Waterhouse et al. 2013
	Ponce de Leon Inlet	$3.4 \cdot 10^{-2}$	12	0.35	Waterhouse and Valle-Levinson 2010
	Conway, Tal-y-Cafn reach	$3.9 \cdot 10^{-2}$	5.5	0.14	Nunes and Simpson 1985

Table 2.2.: Aspect ratios of several real estuaries, calculated from depth and width as found in the given literature and divided into three size classes (see section 2.4.1.1, Fig. 2.2). It should be noted that $H = H_{\text{mean}}$ in the first three examples.

In order to keep the channel shape (λ) and the non-dimensional quasi-lateral diffusivities ($\tilde{A}_{y*} = \tilde{K}_{y*}$) constant, the full width at half maximum depth and the dimensional diffusivities are varied (see Tab. 2.1).

It should be noted that preliminary tests confirmed self-similarity when the dimensional parameters are varied but the non-dimensional numbers are invariant. For example, if H_{max} is doubled, invariance of the non-dimensional numbers requires doubling of H_{min} , z_0^b , W , FWHM and U_t as well as quadrupling of A_{y*} and K_{y*} . If this is taken account of, the results of the two simulations are the same.

Please also note that, for the default parameter values (Tab. 2.1), Coriolis force has no significant effect on the residual circulation (section 2.4.3.2).

2.3.3. Analysis and notation

Velocities (u , v , w), vertical eddy viscosity (A_z) and salinity (S) are analysed based on the last (tenth) tidal cycle of the model output, when a periodic state is reached.

The time and spatial coordinates are non-dimensionalised by their characteristic scales:

$$\tilde{t} = t/T, \tilde{y} = y/W, \tilde{z} = z/H_{\text{max}}. \quad (2.15)$$

The non-dimensional time is defined such that we have full flood at $\tilde{t} = 0.25$ and full ebb at 0.75.

The velocities are non-dimensionalised by the tidal current amplitude, U_t (Burchard et al. 2011), and the eddy viscosity by H_{\max} and U_* :

$$\tilde{u} = u/U_t, \tilde{v} = v/U_t, \tilde{w} = w/U_t, \quad (2.16)$$

$$\tilde{A}_z = A_z/(H_{\max}U_*). \quad (2.17)$$

Residual (tidally averaged) values are denoted by triangular brackets, $\langle \tilde{u} \rangle$, and fluctuations by primes, $\tilde{u}' = \tilde{u} - \langle \tilde{u} \rangle$.

The estuarine circulation, i.e. the total residual longitudinal circulation, is decomposed into contributions from tidal straining, gravitational and advectively driven circulation and other, minor effects (see section 4.1) by means of the method presented by Burchard and Hetland (2010) and Burchard et al. (2011):

$$\langle \tilde{u}_{\text{total}} \rangle = \langle \tilde{u}_{\text{strain}} \rangle + \langle \tilde{u}_{\text{grav}} \rangle + \langle \tilde{u}_{\text{advec}} \rangle + \text{other}, \quad (2.18)$$

$$\langle \tilde{u}_i \rangle = \langle u_i \rangle / U_t, \quad (2.19)$$

$$\langle u_i \rangle = \int_{-H}^z \mathcal{A}_i d\hat{z} - \frac{\gamma(y, z)}{H(y)} \int_{-H}^0 \int_{-H}^z \mathcal{A}_i d\hat{z} dz, \quad (2.20)$$

$$\gamma(y, z) = \frac{H \int_{-H}^z \hat{z} / \langle A_z \rangle d\hat{z}}{\int_{-H}^0 \int_{-H}^z \hat{z} / \langle A_z \rangle d\hat{z} dz}. \quad (2.21)$$

The tidal straining circulation, $\langle \tilde{u}_{\text{strain}} \rangle$, results from the covariance of the eddy viscosity and the vertical shear of the longitudinal velocity divided by the residual viscosity:

$$\mathcal{A}_{\text{strain}} = -\langle A'_z \partial_z u' \rangle / \langle A_z \rangle. \quad (2.22)$$

The gravitational circulation, $\langle \tilde{u}_{\text{grav}} \rangle$, is forced by the longitudinal buoyancy gradient and the advectively driven circulation, $\langle \tilde{u}_{\text{advec}} \rangle$, by lateral and vertical advection:

$$\mathcal{A}_{\text{grav}} = \int_z^0 \int_{\hat{z}}^0 \langle \partial_x b \rangle d\hat{z} d\hat{z} / \langle A_z \rangle, \quad (2.23)$$

$$\mathcal{A}_{\text{advec}} = \left\{ - \int_z^0 \partial_y \langle uv \rangle d\hat{z} + \langle uw \rangle \right\} / \langle A_z \rangle. \quad (2.24)$$

It should be noted that these contributions are not independent of each other but that they interact non-linearly. For example, the tidal straining circulation is associated with stratification and shear, both of which are influenced by the total residual circulation. Still, the direct forcing mechanisms are identified with this method and can then be further investigated, as we will show for the tidal straining circulation (sections 2.4.1.3 and 2.4.2).

For the quantification of the intensity of the total circulation and its contributions, the following measure is applied (Burchard et al. 2011):

$$\mathcal{M}(\langle \tilde{u}_i \rangle) = -\frac{1}{W} \int_0^W \frac{4}{H^2(y)} \int_{-H(y)}^0 \langle \tilde{u}_i \rangle(y, z) \left\{ z + \frac{H(y)}{2} \right\} dz dy. \quad (2.25)$$

This measure is additive, i.e.

$$\mathcal{M}(\langle \tilde{u}_{\text{total}} \rangle) = \mathcal{M}(\langle \tilde{u}_{\text{strain}} \rangle) + \mathcal{M}(\langle \tilde{u}_{\text{grav}} \rangle) + \mathcal{M}(\langle \tilde{u}_{\text{advec}} \rangle) + \text{other}, \quad (2.26)$$

and it preserves the orientation of the circulation, with $\mathcal{M}(\langle \tilde{u}_i \rangle) > 0$ for classical estuarine circulation.

For visualisation of the transverse circulation, a particle tracking model is applied. The utilised integration scheme is 4th order Runge-Kutta with a time step of $\Delta t = T/500 \approx 89.4$ s. The interpolation is linear in time and cubic in space. The model is implemented in MATLAB.

About 8000 particles are released in one half of the cross-section (symmetric, Fig. 2.1b). They are initially (at slack after ebb) distributed on a rectangular grid with a non-dimensional spacing of $\Delta \tilde{z} = 6.7 \cdot 10^{-3}$ in the vertical and $\Delta \tilde{y} = 5 \cdot 10^{-3}$ in the lateral direction. (Note that the model is dimensional.) The particles are moved solely by transverse advection (\tilde{v} and \tilde{w}) over one tidal cycle.

It should be noted that the transverse advection is not independent of the longitudinal advection (\tilde{u}). Only the direct influence of \tilde{u} and of diffusion is ignored for the particle tracking.

2.4. Results and discussion

2.4.1. Aspect ratio and estuarine circulation

2.4.1.1. Impact of the aspect ratio on the estuarine circulation contributions

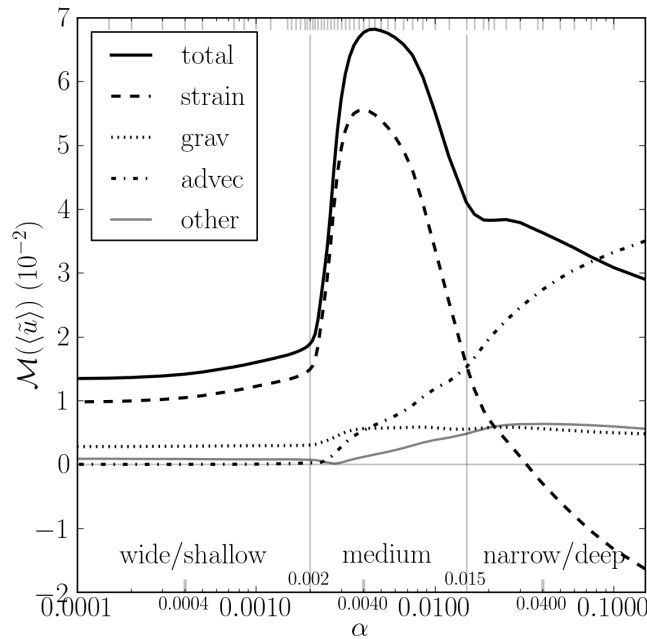


Figure 2.2.: Measure of the intensity of the residual longitudinal circulation contributions for varying aspect ratio (experiment A). The short bars at the upper abscissa mark the α values of the individual simulations; the two vertical lines represent the limits between wide, medium and narrow channels ($\alpha_1 = 0.002$, $\alpha_2 = 0.015$) and the three short bars at the lower abscissa mark the channels shown in the following figures ($\alpha_w = 0.0004$, $\alpha_m = 0.004$, $\alpha_n = 0.04$).

The impact of a channel's aspect ratio on the intensity of the estuarine circulation and its contributions is shown in Fig. 2.2. For convenience, we define the following three size classes: **wide/shallow** channels with $\alpha \leq \alpha_1 = 0.002$, **narrow/deep** channels with $\alpha \geq \alpha_2 = 0.015$ and **medium** channels in between. These limits (solid vertical lines in Fig. 2.2) coincide with distinct changes of the residual longitudinal circulation, particularly the tidal straining and the advectively driven contribution.

It should be noted that the values of α_1 and α_2 as well as the course of the functions $\mathcal{M}(\langle \tilde{u}_i \rangle)$ over α depend on the prescribed parameters (Tab. 2.1), which vary along real estuaries, just as α .

In wide channels, the estuarine circulation is relatively weak, with the tidal straining circulation being the dominant contribution (73 – 79%), followed by the gravitational circulation (21 – 16%).

At $\alpha_1 = 0.002$, the intensity of the tidal straining circulation starts to increase sharply, the advectively driven circulation starts to increase and the gravitational circulation increases slightly. In medium channels, the total circulation reaches a maximum, which is caused primarily by a maximum of the tidal straining circulation at $\alpha_m = 0.004$. The advectively driven circulation continues to increase while the gravitational circulation remains about constant.

At $\alpha_2 = 0.015$, the advectively driven circulation becomes stronger than the tidal straining circulation so that, in narrow channels, the advectively driven circulation is the dominant contribution. The intensity of the tidal straining circulation falls below zero at $\alpha = 0.03$, i.e. the tidal straining circulation reverses and opposes the classical estuarine circulation in very narrow channels. The gravitational circulation remains about constant.

These results raise the main question of this paper: Why is the tidal straining circulation maximum for a certain aspect ratio? Furthermore, why is it reverse in very narrow channels? Before we answer this (sections 2.4.1.3 and 2.4.2.1), let us consider the residual velocity profiles establishing the circulation intensities.

2.4.1.2. Comparison of residual profiles for different aspect ratios

Cross-sectional views of the residual circulation contributions are shown in Fig. 2.3 for a wide ($\alpha_w = 0.0004$), a medium ($\alpha_m = 0.004$) and a narrow ($\alpha_n = 0.04$) channel. In agreement with the measure of their intensity (Fig. 2.2, α values marked at lower abscissa), the medium channel exhibits the strongest down-estuary residual flow at the surface and up-estuary flow above the bottom (Fig. 2.3a2), which is mainly caused by the strong tidal straining circulation (**b2**). The gravitational (**c2**) and the advectively driven contribution (**d2**) are much weaker.

In the wide channel, all circulation contributions are weaker than in the medium channel (**a1-d1** vs. **a2-d2**). The advectively driven circulation (**d1**) has almost ceased so that the wide channel resembles a one-dimensional situation.

In the narrow channel, the advectively driven circulation is stronger than in the medium channel (**d2** vs. **d3**) and the tidal straining circulation exhibits up-estuary flow below the surface and down-estuary flow at the slopes and in the centre of the channel (**b3**), which opposes the classical estuarine circulation ($\mathcal{M}(\langle \tilde{u}_{\text{strain}} \rangle) < 0$, Fig. 2.2).

Also shown in Fig. 2.3 are the residual eddy viscosity and the salinity. In the wide channel, salinity decreases from the thalweg to the shoals and only very slightly from the bottom to the surface (**f1**). Consequently, stratification is very weak. Eddy viscosity, on the other hand, is strong in the centre of the channel (**e1**).

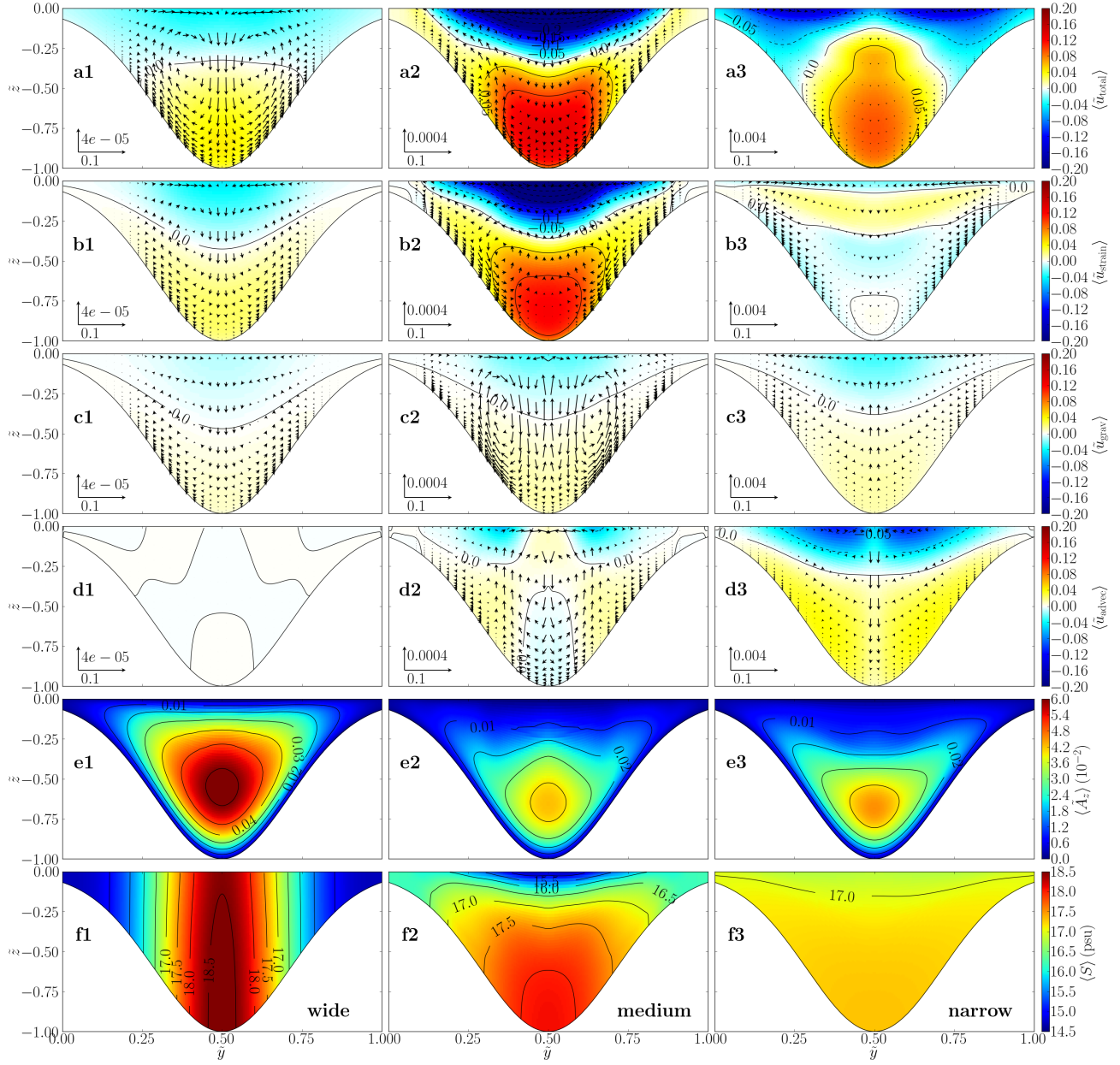


Figure 2.3.: From left to right: **1** wide ($\alpha_w = 0.0004$), **2** medium ($\alpha_m = 0.004$) and **3** narrow ($\alpha_n = 0.04$) channel; from top to bottom: residual profile of non-dimensional **a** estuarine circulation, **b** tidal straining circulation, **c** gravitational circulation, **d** advectively driven circulation, **e** eddy viscosity and **f** dimensional salinity. Note that the velocity scales change with the aspect ratio.

In the medium channel, salinity stratification is strong with highest values above the centre of the channel (**e2**). Eddy viscosity is relatively small and confined to the deep parts of the channel (**f2**).

In the narrow channel, salinity varies only very little with strongest stratification occurring below the surface (**f3**). There, eddy viscosity is comparable to that in the medium channel; in the lower part, it is slightly higher (**e3**).

A detailed explanation of the differences in circulation, eddy viscosity and stratification for different channel widths follows in the next sections (2.4.1.3 and 2.4.2).

2.4.1.3. Origin of the maximum and the reverse tidal straining circulation

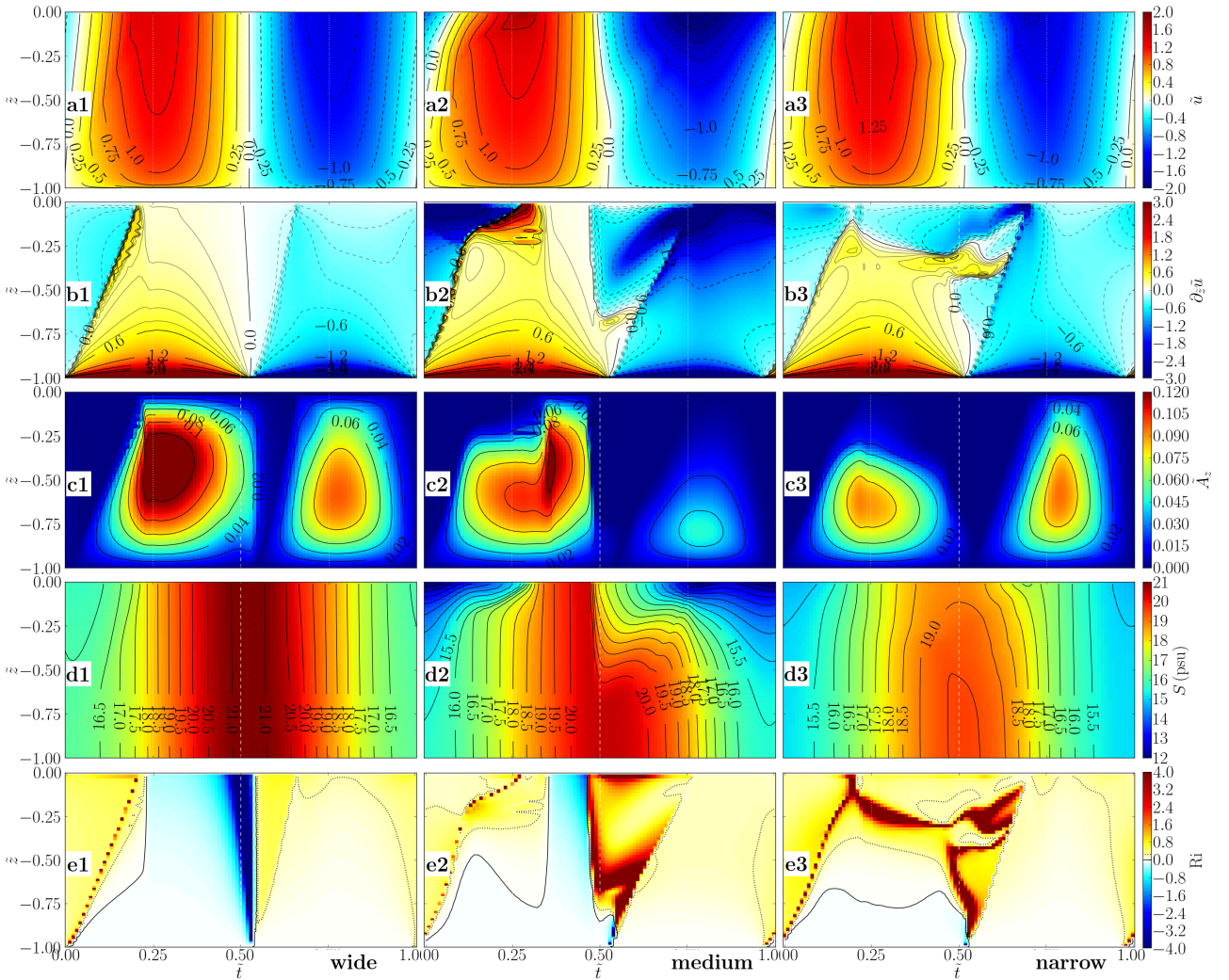


Figure 2.4.: From left to right: **1** wide ($\alpha_w = 0.0004$), **2** medium ($\alpha_m = 0.004$) and **3** narrow ($\alpha_n = 0.04$) channel; from top to bottom: tidal cycle at thalweg of non-dimensional **a** longitudinal velocity, **b** vertical shear of longitudinal velocity, **c** eddy viscosity, **d** dimensional salinity and **e** gradient Richardson number, $Ri = N^2/S^2$ (solid contour at $Ri = 0$, dotted at 0.25).

In order to investigate the maximum of the tidal straining circulation in the medium channel, we now take a closer look at tidal cycles of the longitudinal velocity, its vertical shear, the eddy

viscosity, the salinity and the gradient Richardson number at the thalweg (Fig. 2.4). Recall that the covariance of viscosity and vertical shear of longitudinal velocity divided by residual viscosity is the driving term for the tidal straining circulation ($\mathcal{A}_{\text{strain}}$, (2.22)).

In the wide channel, the expected behaviour of weak strain-induced periodic stratification is observed (SIPS, see section 1.2 and references therein): The shear is weakly asymmetric with negative shear being slightly stronger and longer-lasting than positive shear ($\partial_z \tilde{u} \approx -1.08$ at full ebb vs. 1.03 at full flood, thalweg averages) (Fig. 2.4**a1,b1**). This is due to the eddy viscosity asymmetry with smaller eddy viscosity during ebb than during flood (**c1**), which is again due to the weak, strain-induced stratification during ebb and early flood and homogeneous or even unstable water columns (negative Ri) during full and late flood (**d1,e1**).

The tidal asymmetries grow drastically when going to medium channels. (Recall that only the aspect ratio is changed, in terms of non-dimensional numbers.) In the medium channel, negative shear is much stronger than positive shear (-1.99 vs. 1.24), particularly in the upper half of the thalweg water column (-1.14 vs. 0.31) (**a2,b2**). This leads to very high shear fluctuations with $\partial_z \tilde{u}' < 0$ (i.e. $\partial_z \tilde{u} < \partial_z \langle \tilde{u} \rangle$) during ebb and $\partial_z \tilde{u}' > 0$ (i.e. $\partial_z \tilde{u} > \partial_z \langle \tilde{u} \rangle$) during flood (not shown). Furthermore, negative shear is very persistent in the upper half, at the surface even from before slack after flood ($\tilde{t} \approx 0.47$) till after full flood ($\tilde{t} \approx 0.27$). This strong and long-lasting negative shear is due to very low eddy viscosity not only during ebb (**c2**): Eddy viscosity strongly decreases already before slack after flood, remains comparably low even at full ebb and peaks only after full flood ($\tilde{t} \approx 0.36$). This low eddy viscosity is again due to very strong stratification (**d2,e2**), which sets in already before slack after flood and persists throughout the entire ebb phase and into the flood phase, at the surface even till after full flood. This behaviour cannot be explained by the longitudinal tidal currents; transverse processes must play an important, stratifying role and are going to be investigated in section 2.4.2.1.

In the narrow channel, negative shear is still stronger and longer-lasting than positive shear (-1.14 vs. 1.03) (**a3,b3**). Close to the surface, this negative shear even persists over the entire tidal cycle. Eddy viscosity is now stronger during ebb than during flood (**c3**), but its maximum is smaller than that in wide or medium channels. This reverse eddy viscosity asymmetry is due to a reverse stratification pattern with strongest (though still weak) stratification during and shortly after flood and homogeneous water columns in the second half of the ebb phase (**d3,e3**). This behaviour cannot be explained by the longitudinal tidal currents, either.

fulfilment of characteristics	wide	medium	narrow
(i) $\partial_z \tilde{u}' > 0$, $\tilde{A}'_z > 0$ during flood	☑	☑	☐
(ii) $\partial_z \tilde{u}' < 0$, $\tilde{A}'_z < 0$ during ebb	☐	☑	☐
(iii) $\langle \tilde{A}_z \rangle$ small	☐	☑	☑

Table 2.3.: Overview of the characteristics leading to maximum tidal straining circulation as well as their fulfilment (☑) for the three size classes. (An empty check box, ☐, corresponds to the notation (i) etc. in the text.)

Three characteristics lead to the observed maximum of the tidal straining circulation in the medium channel (Tab. 2.3): (i) Positive shear fluctuation ($\partial_z \tilde{u}' > 0$) coincides with strong eddy viscosity, i.e. positive viscosity fluctuation ($\tilde{A}'_z > 0$, i.e. $\tilde{A}_z > \langle \tilde{A}_z \rangle$), during flood; (ii) negative shear fluctuation coincides with very weak eddy viscosity, i.e. negative viscosity fluctuation, during ebb and (iii) the

residual eddy viscosity is low. (i) and (ii) determine the orientation of the tidal straining circulation, which is classical ($\mathcal{M}(\langle \tilde{u}_{\text{strain}} \rangle) > 0$) in the medium channel. All three characteristics determine the intensity, which shows a maximum value here.

In the wide channel, only characteristic (i) is clearly fulfilled; positive shear fluctuation coincides with strong viscosity fluctuation during flood. Negative shear fluctuation coincides with moderate viscosity, i.e. positive viscosity fluctuation (not shown), around full ebb ((ii) not fulfilled, notation: (ii)); however, negative shear fluctuation coincides with very weak viscosity, i.e. negative viscosity fluctuation, at the beginning of ebb and around slack after ebb (ii). The residual tidal straining circulation in the wide channel is classically oriented, but the opposing contribution during ebb (ii) and the high residual viscosity (iii) yield a weak intensity.

In the narrow channel, the eddy viscosity asymmetry is reverse, but the shear asymmetry is not. (The surface shear is negative during flood, but its fluctuation is positive like in wide and medium channels; not shown.) Positive shear fluctuation coincides with moderate viscosity, i.e. positive viscosity fluctuation, around full flood (i) but with very weak viscosity, i.e. negative viscosity fluctuation, at the beginning and end of flood (i). Negative shear fluctuation coincides with very weak viscosity, i.e. negative viscosity fluctuation, at the beginning and end of ebb (ii) but with strong viscosity, i.e. positive viscosity fluctuation, around full ebb (ii). The classical-opposing contributions are slightly larger than the classical so that the residual tidal straining circulation opposes the classical orientation, i.e. the tidal straining circulation is reverse in narrow channels. The fact that these contributions almost balance yields a weak intensity even though the residual viscosity is low (iii).

2.4.2. Transverse stratifying and destratifying processes

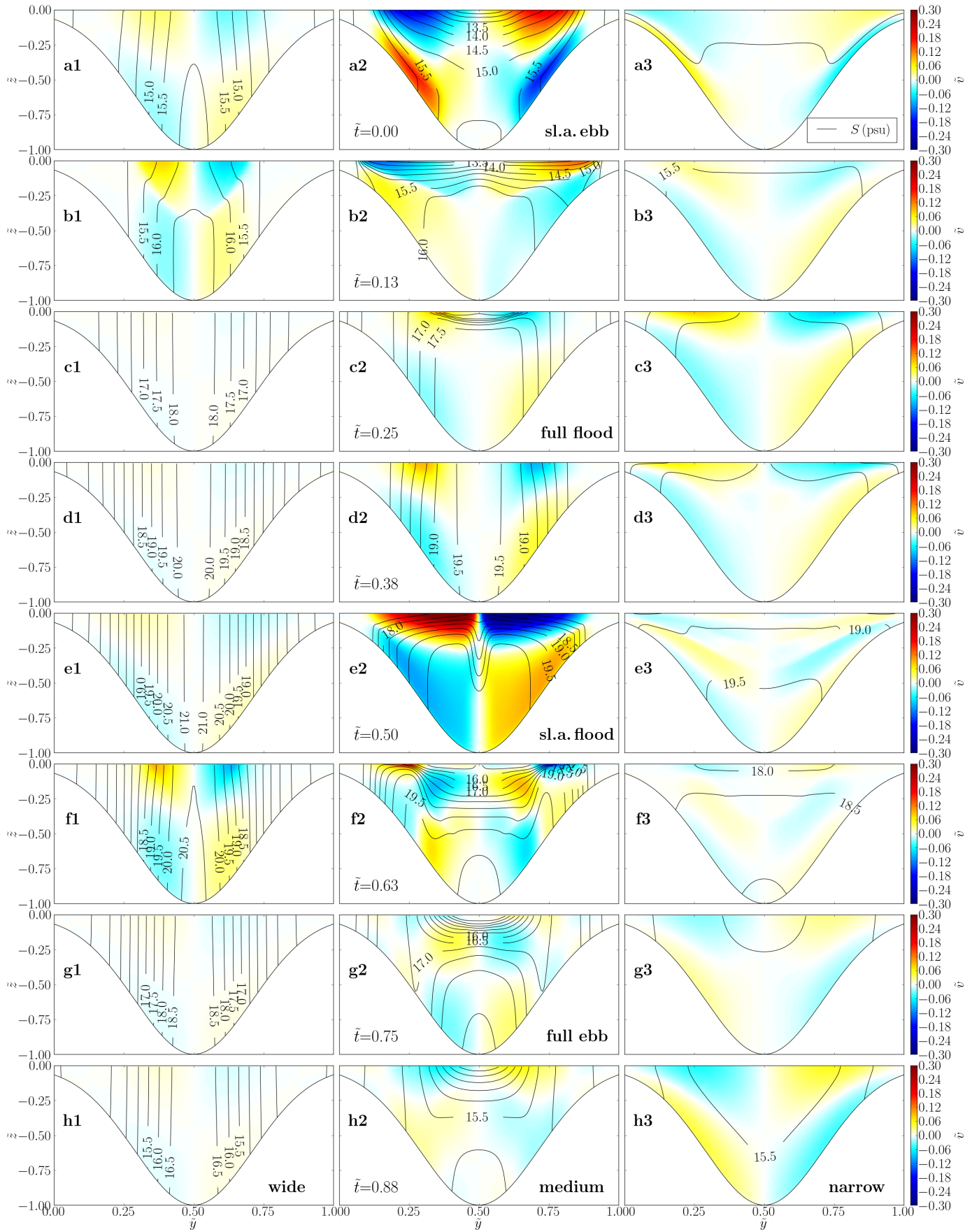
2.4.2.1. Stratification by transverse salinity advection

As explained above, the vertical shear of the longitudinal velocity is affected by the eddy viscosity, which itself is affected by the stratification. The observed change of the stratification pattern with only the aspect ratio (Fig. 2.4d1-d3) suggests the importance of transverse, stratifying as well as destratifying processes. In order to understand these processes, we now consider the lateral and vertical advection of salinity over one tidal cycle. Fig. 2.5 shows snapshots of the lateral velocity and the salinity.

We begin with the medium channel and the flood phase. The slope, $\partial_y H(y)$, causes laterally differential longitudinal advection of salinity, which builds a lateral salinity gradient with highest salinity at the thalweg (Fig. 2.5b2-e2). This generates flood-oriented transverse circulation (surface convergence) (c2-e2), which strains the salinity field (d2-e2) and induces strong stratification already shortly before slack after flood (e2).

The strong stratification in the centre of the channel persists throughout the ebb and into the flood phase (e2-h2, a2-c2). Laterally differential longitudinal advection during ebb builds a salinity gradient with lowest salinity at the thalweg, in the upper half of the cross-section (g2-a2). This generates ebb-oriented transverse circulation (h2-b2), which also enhances stratification (a2-b2).

Figure 2.5. (following page): From left to right: **1** wide ($\alpha = 0.0004$), **2** medium ($\alpha = 0.004$) and **3** narrow ($\alpha = 0.04$) channel; from top to bottom: non-dimensional lateral velocity (colour) and dimensional salinity (contours, interval 0.5 psu) at **a** $\tilde{t} = 0.00$ (slack after ebb), **b** 0.13, **c** 0.25 (full flood), **d** 0.38, **e** 0.50 (slack after flood), **f** 0.63, **g** 0.75 (full ebb) and **h** 0.88.



Considering the effect of stratification on eddy viscosity and thus vertical shear of horizontal velocities, the key leading to the maximum of the tidal straining circulation in the medium channel appears to be the matching length scales of half the channel width and the lateral salinity advection during the second half of flood (**c2-e2**), which leads to strong stratification already at the very beginning of the ebb phase (**e2**). Due to the stratification-shear feedback during ebb (enforcing each other until the gradient Richardson, Ri , number falls below 0.25, at the surface around full ebb, Fig. 2.4**e2**), the ebb viscosity is very low and thus the tidal asymmetry very strong.

The wide channel has a gentler slope so that the lateral gradients of the longitudinal velocity and thus of the salinity are smaller than in the medium channel. (Note that the salinity range over \tilde{y} needs to be ten times as large as in the medium channel to imply the same lateral salinity gradient.) Consequently, the transverse circulation is weaker so that, also considering the larger width, the salinity field is hardly strained (Fig. 2.5**a1,b1,f1**). Furthermore, the lateral salinity gradient and the transverse circulation are always flood-oriented. This is due to the positive feedback of the lateral gradients and the transverse circulation during flood (see Lerczak and Geyer 2004) and the high inertia of the large water body.

The narrow channel has a steeper slope so that the lateral gradients of the longitudinal velocity and thus of the salinity are larger than in the medium channel. (Note that the salinity range over \tilde{y} is much smaller than in the medium channel, but not by a factor of ten.) Consequently, the transverse circulation is stronger so that, also considering the smaller width, the salinity field is strained very fast, e.g. already before full flood (Fig. 2.5**b3-c3**). This fast straining leads to persistent stratification at the surface (Fig. 2.4**d3**) and thus to low eddy viscosity and negative shear during flood (Fig. 2.4**c3,b3**). (It should be noted that the overall stratification in the narrow channel is substantially weaker than in the medium channel.) During ebb, longitudinal SIPS adds (Fig. 2.5**f3**), but the stratification-shear feedback (see above) leads to $Ri < 0.25$ already before full ebb (Fig. 2.4**e3**) so that stratification is reduced by strong shear production of turbulence and the eddy viscosity is higher than during flood. This reverse stratification and eddy viscosity asymmetry leads to the reverse tidal straining circulation.

2.4.2.2. Distinction of the stratifying processes: particle tracking and mathematical decomposition

Fig. 2.5 clearly suggests but cannot prove that transverse salinity advection is the dominant stratifying process in the medium channel. By means of particle tracking, the contribution of transverse advection to the salinity redistribution can be visualised.

The results of the transverse particle tracking are presented in Fig. 2.6 for the second half of flood. Shown are the instantaneous positions of the particles, marked by dots, and their colour-coded salinity (see below and figure caption). The initially equidistant particle distribution (at slack after ebb, not shown) becomes inhomogeneous due to interpolation and truncation errors of the integration scheme. (Note that there is no con- or divergence in the transverse plane, $\partial_y v + \partial_z w = 0$ since $\partial_x u = 0$.) For the colour mapping of the particles (Fig. 2.6), we use the following salinity fields:

- a:** instantaneous, i.e. at present position and time (full flood, contours in Fig. 2.5**c**),
- b:** memorised, i.e. at previous position and time (full flood, particles as information carrier),
- c:** instantaneous (slack after flood, Fig. 2.5**e**).

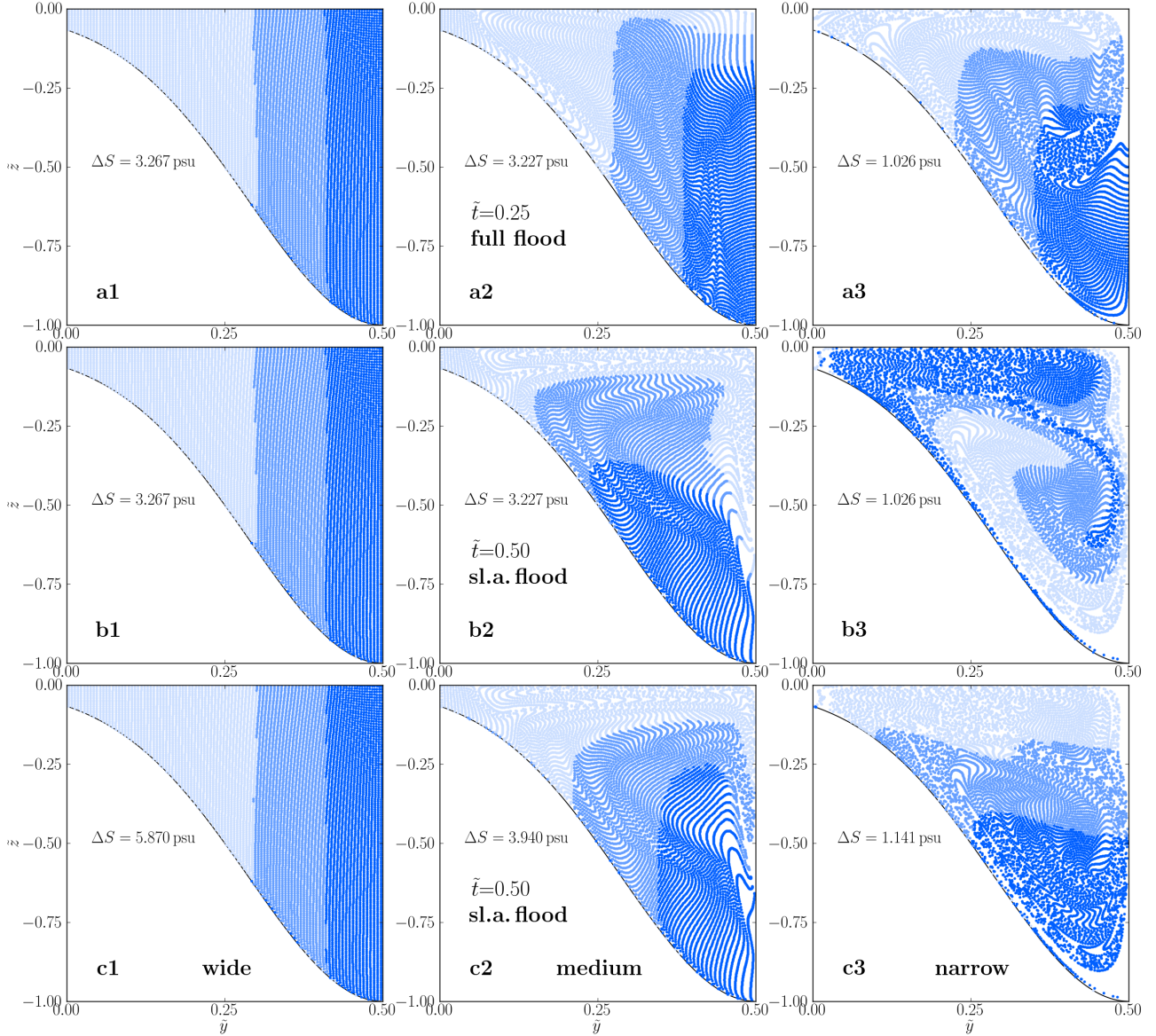


Figure 2.6.: From left to right: **1** wide ($\alpha_w = 0.0004$), **2** medium ($\alpha_m = 0.004$) and **3** narrow ($\alpha_n = 0.04$) channel; from top to bottom: **a** salinity at full flood (cp. contours in Fig. 2.5c), **b** hypothetical salinity at slack after flood if the salinity at full flood (**a**) is solely advected by transverse circulation (particle tracking) and **c** actual salinity at slack after flood (cp. Fig. 2.5e). The dots mark the particle positions at the given time. Their blue shadings indicate the freshest (light blue), middle and saltiest third (deep blue) of the particles. (The salinity range, ΔS , is given in each panel).

Thus, Fig. 2.6**b** shows the hypothetical salinity at slack after flood for the theoretical case that the salinity at full flood, **a**, is solely advected by transverse circulation, i.e. that longitudinal advection and salinity diffusion are ignored. (Please note again that only their direct influence on the particles is ignored; they still co-determine the transverse circulation.) **c** shows the actual salinity at slack after flood as it results from longitudinal and transverse advection, diffusion and their interaction.

The wide channel is vertically homogeneous at full flood with salinity increasing toward the thalweg (Fig. 2.6**a1**). The generated transverse circulation induces very weak stratification above the slopes at slack after flood (**b1**). Comparison of Fig. 2.6**b1** with **c1** indicates that this is the dominant stratifying process in this part of the tidal cycle.

The medium channel is also vertically homogeneous at full flood with salinity increasing toward the thalweg except for subsurface stratification at the thalweg (Fig. 2.6**a2**), which is a remainder from strong stratification during ebb (Fig. 2.4**d2**). The transverse circulation induces strong stable stratification at slack after flood except for the thalweg and the bottom at the slopes (Fig. 2.6**b2**). Comparison of Fig. 2.6**b2** with **c2** indicates that this is the dominant stratifying process here, too. The actual salinity field (**c2**) is vertically homogeneous above the bottom at the slopes due to turbulent diffusion and more saline toward the thalweg due to further laterally differential longitudinal advection.

The narrow channel is already weakly stratified in the upper centre of the channel at full flood (Fig. 2.6**a3**). The transverse circulation stirs the salinity field and induces unstable stratification at slack after flood (**b3**). The actual salinity field (**c3**) is not unstable, though, but stably stratified due to the negative shear close to the surface even during flood (section 2.4.1.3, Fig. 2.4**b3**).

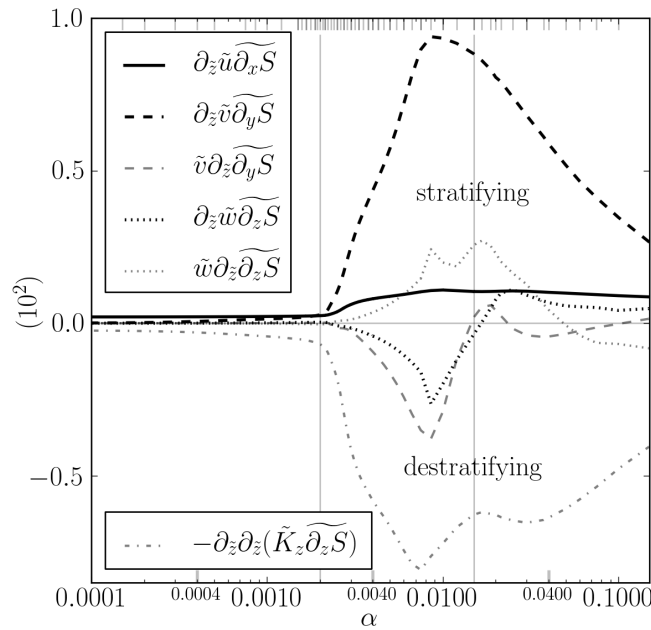


Figure 2.7.: Residual and cross-sectionally averaged non-dimensional stratifying (> 0) and destratifying terms (2.27). Vertical lines and bars as in Fig. 2.2.

Stratification by transverse salinity advection is composed of lateral and vertical straining and advection of stratification. The contributions from longitudinal, lateral and vertical straining and advection to the stratification can be distinguished when considering the residual of the vertical

gradient of the salinity budget equation (2.3):

$$\begin{aligned}
 0 &= \langle \partial_t \partial_z S \rangle + \langle \partial_z (u \partial_x S) \rangle + \langle \partial_z (v \partial_y S) \rangle + \langle \partial_z (w \partial_z S) \rangle \\
 &\quad - \langle \partial_z \partial_{y*} (K_{y*} \partial_{y*} S) \rangle - \langle \partial_z \partial_z (K_z \partial_z S) \rangle \\
 &= \underbrace{\langle \partial_z u \partial_x S \rangle}_{\substack{\text{long. strain.} \\ \rightarrow 1\text{SIPS}}} + \underbrace{\langle \partial_z v \partial_y S \rangle}_{\substack{\text{lat. strain.} \\ \rightarrow 2\text{SIPS}}} + \underbrace{\langle \partial_z w \partial_z S \rangle}_{\substack{\text{vert. strain.} \\ \rightarrow 3\text{SIPS}}} + \underbrace{\langle v \partial_y \partial_z S \rangle}_{\substack{\text{lat. advec.} \\ \rightarrow 2\text{APS}}} + \underbrace{\langle w \partial_z \partial_z S \rangle}_{\substack{\text{vert. advec.} \\ \rightarrow 3\text{APS}}} \\
 &\quad - \underbrace{\langle K_{y*} \partial_{y*} \partial_{y*} \partial_z S \rangle}_{\text{quasi-lat. diff.}} - \underbrace{\langle \partial_z \partial_z (K_z \partial_z S) \rangle}_{\text{vert. diff.}}.
 \end{aligned} \tag{2.27}$$

$K_z(y, z, t)$ is the vertical diffusivity of salinity. (Note that $\partial_x S$ and K_{y*} are constant here, see section 2.3.2.)

Without the residual, (2.27) is similar to the evolution equation of the lateral salinity gradient derived by Giddings et al. (2012, their (3)) and provides an alternative to the evolution equation of the potential density anomaly (Burchard and Hofmeister 2008; de Boer et al. 2008).

Since longitudinal SIPS is a universal process in all regions with longitudinal density gradients and tidal currents, we call it *primary strain-induced periodic stratification (1SIPS)* in the following. Accordingly, we suggest to call periodic stratification by lateral/vertical straining *secondary/tertiary strain-induced periodic stratification (2/3SIPS)*.

Laterally/vertically advected periodic stratification is abbreviated *2/3APS*. The combination of APS and SIPS is already known as *ASIPS* (de Boer et al. 2008; Howlett et al. 2011), in our case *2ASIPS* for laterally and *3ASIPS* for vertically advected and strain-induced periodic stratification.

All terms in (2.27) are non-dimensionalised by multiplication with $H_{\max}/(U_* |\partial_x S|) > 0$. The residual and cross-sectionally averaged non-dimensional straining, advection of stratification and vertical diffusion are shown in Fig. 2.7 (positive \equiv stratifying). (The quasi-lateral diffusion term is negligible and therefore omitted.)

In wide channels (without Coriolis forcing), 1SIPS is more important than 2- and 3ASIPS. In very wide channels, 2- and 3ASIPS are negligible.

In medium channels, 1SIPS is about four times as strong as in wide channels (feedback of transverse processes), but 2SIPS increases and dominates considerably, though it is partly compensated by negative 2APS, i.e. lateral advection of weaker stratification (from shoals to thalweg, not shown). Negative 3SIPS and positive 3APS approximately balance each other.

In narrow channels, 2SIPS is still the dominant stratifying term, but it decreases. Positive 3SIPS contributes about half as strong as 1SIPS. Close to the limit between medium and narrow channels ($\alpha \approx 0.02$), 3SIPS and positive 3APS, i.e. vertical advection of stronger stratification (from surface to bottom, not shown), concur so that 3ASIPS is about three times as important as 1SIPS.

2.4.2.3. Secondary strain-induced periodic stratification

Since 2SIPS is the dominant stratifying term except in wide channels (Fig. 2.7), it is now elucidated a bit further. It has a periodicity of $T/2$: In the medium channel, transverse circulation is generated (or rather turned into the orientation corresponding to the respective tidal phase) around full tides (Fig. 2.5c2, h2), when laterally differential longitudinal advection has already built a considerable lateral salinity gradient (schematic Fig. 2.8a, cp. Fig. 2.6a1, a2). As soon as lateral straining has flattened this gradient, stratification is maximum (Fig. 2.8b2). In the medium channel, this occurs

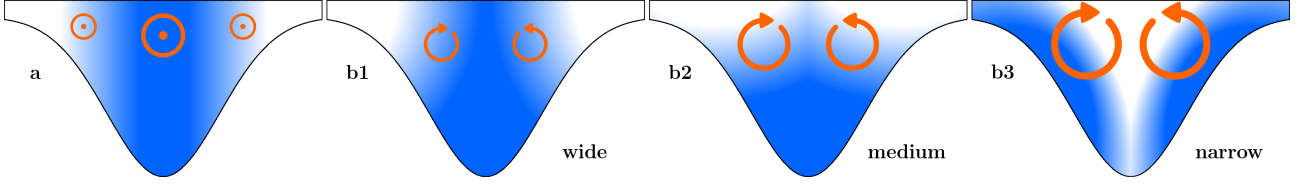


Figure 2.8.: Schematic of secondary straining: **a** laterally differential longitudinal advection (orange arrow-heads; figure orientation: looking down-estuary) and lateral salinity gradient (deeper blue shading indicates higher salinity) during flood; **b** transverse circulation and strained salinity field in **b1** wide, **b2** medium and **b3** narrow channels at slack after flood.

around slack tides (Fig. 2.5**b2,e2**, 2.6**b2**).

The further development depends on the tidal phase: After slack after ebb, during the first half of flood, stratification is decreased (Fig. 2.5**b2-d2**); after flood, during ebb, it is increased (**e2-g2**) due to 1SIPS (periodicity T).

In addition to multidirectional SIPS and APS, shear-induced turbulence (periodicity $T/2$) interferes with the stratification (highest shear, turbulent diffusion and destratification at full tides; cp. Fig. 2.4). Furthermore, all these processes interact non-linearly so that it is difficult to distinguish the effect of 2SIPS.

In wider channels, 2SIPS is weaker and limited to the slopes (Fig. 2.5**a1-b1,f1**, 2.6**b1**) because the length scale of the lateral velocity is smaller than half the channel width (Fig. 2.8**b1**). Lateral straining and stratification are maximum only after slack tides (Fig. 2.5**f1,b1**).

In narrower channels, 2SIPS sets in very early (Fig. 2.5**b3,f3**, 2.6**a3**) and is then subject to longitudinal shear (Fig. 2.4**a3,b3**) and turbulent diffusion (Fig. 2.6**b3-c3**). The length scale of the lateral velocity is larger than half the channel width so that transverse stirring occurs (Fig. 2.8**b3**, cp. Fig. 2.6**b3**).

2.4.3. Further results and discussion

2.4.3.1. Importance of transverse advection of salinity and momentum

Further evidence of the importance of transverse salinity advection for the maximum of the tidal straining circulation is provided by comparison of the full-physics experiment (A) with reduced experiments ignoring transverse advection of momentum (C), of salinity (F) and both (D; no lateral internal pressure gradient, i.e. no transverse circulation; also see section 3.2). The maximum of the tidal straining circulation still exists in experiment C but not in experiments D and F (Fig. 2.9**a**). This implies that salinity advection is more important for the phenomenon than momentum advection.

In experiment D, the intensity of the tidal straining circulation is constant over α , as expected: Without lateral internal pressure gradients, transverse processes are completely switched off so that the lateral dimension does not play a role. The intensities of all circulation contributions in experiment A (Fig. 2.2) remain constant at the values of experiment D (Fig. 2.9**a**) for $\alpha \lesssim 0.0003$ because then the slope, $\partial_y H$, is too small to cause significant lateral gradients of salinity and velocity. Thus, transverse processes are negligible (quasi-one-dimensional).

The maximum of the tidal straining circulation is due to a maximum of the viscosity-shear covariance in medium channels ($\alpha \approx \alpha_m = 0.004$; Fig. 2.9**b**, experiments A and C; characteristics

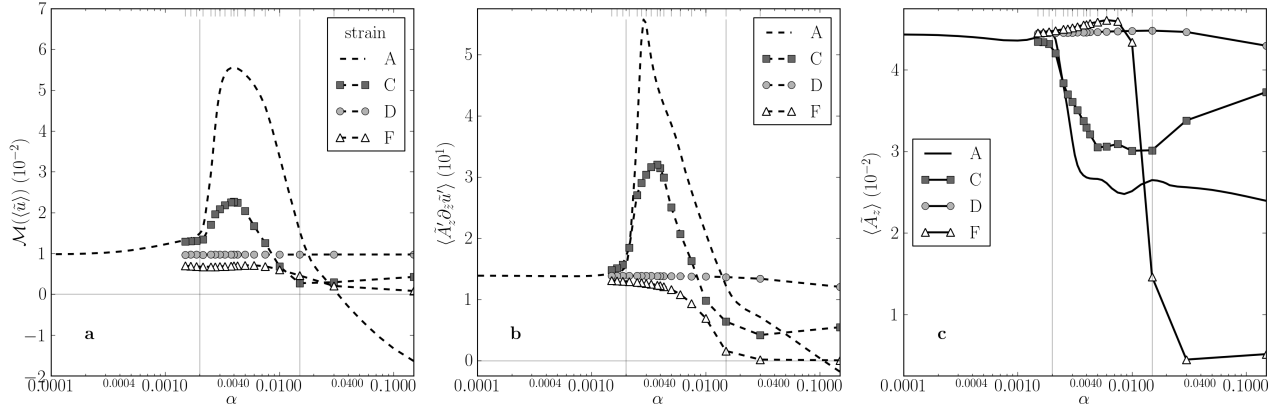


Figure 2.9.: Comparison of full and reduced experiments (A: full physics, C: no momentum advection, D: no lateral internal pressure gradient, F: no transverse salinity advection): **a** same as Fig. 2.2 but only tidal straining circulation, **b-c** thalweg average of non-dimensional **b** viscosity-shear covariance, **c** residual eddy viscosity. The short bars at upper abscissa mark the α values of the individual reduced experiments; vertical lines as in Fig. 2.2.

(i) and (ii) in section 2.4.1.3) as well as to a decrease of the residual eddy viscosity around the limit between wide and medium channels ($\alpha_1 = 0.002$; **c**; characteristic (iii); also see (2.22)).

Please see section 3.2 for a more thorough investigation of the reduced experiments, including a decomposition of the tidal straining circulation.

2.4.3.2. Generality of the results

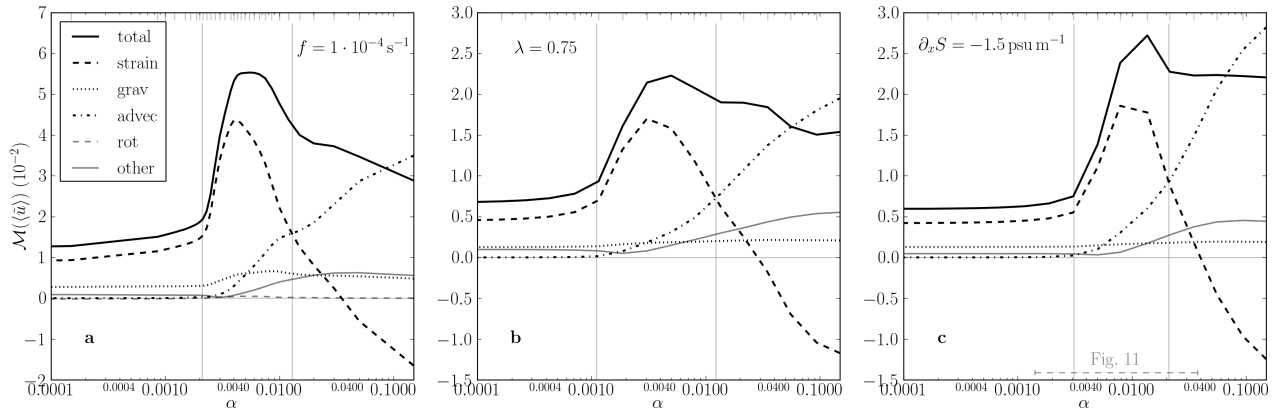
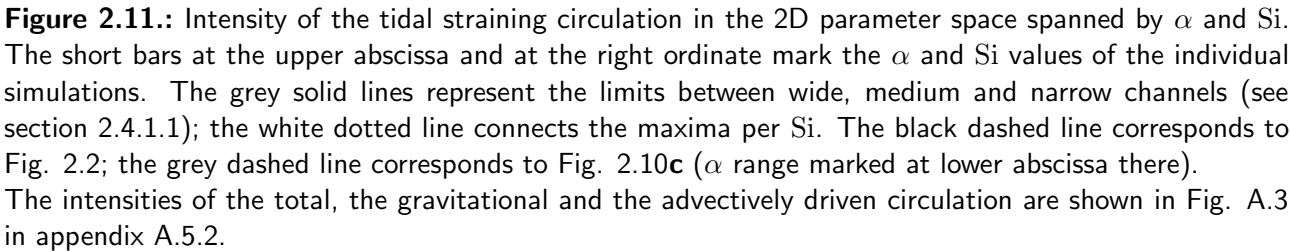


Figure 2.10.: Same as Fig. 2.2 but with different prescribed **a** Coriolis parameter, **b** depth profile, **c** salinity gradient.

In order to substantiate the generality of our findings, we carry out further simulations (experiment A) with different prescribed parameters, namely a non-zero Coriolis parameter, $f = 1 \cdot 10^{-4} \text{ s}^{-1}$ (inverse Ekman number $E_i = fH/U_* = 0.045$; Fig. 2.10a), a depth profile with steeper slopes and wider shoals, $\lambda = 0.75$ (dashed line in Fig. 2.1b; Fig. 2.10b), and half the longitudinal salinity gradient, $\partial_x S = -1.5 \text{ psu m}^{-1}$ ($S_i = 0.24$; Fig. 2.10c).



With Coriolis force (Fig. 2.10a), the intensity of the total residual and of the tidal straining circulation shows a reduction by about 20% (cp. Fig. 2.2) in the medium α range. The rotationally driven contribution, $\langle \tilde{u}_{\text{rot}} \rangle$ (see Burchard et al. 2011), is insignificant. This can be understood when considering the importance of friction relative to the local acceleration (see e.g. Winant 2008, their (A7)):

With $\langle \tilde{A}_z \rangle$ from Fig. 2.9c, (2.28) yields $\delta \approx 1.2$ (0.9) for the wide (medium, narrow) channel, i.e. large friction and negligible Coriolis force.

For decreasing Si , the intensity of the tidal straining circulation decreases (Fig. 2.11; cp. Burchard et al. 2011, 2014) and the maximum is shifted to narrower channels. The aspect ratio

of the channel with maximum tidal straining circulation appears to depend exponentially on the Simpson number: $\alpha_m \propto \exp(-Si)$ (white dotted line; note the logarithmic α scale in all Figs.) Assuming constant H , this can be rewritten as $W_m \propto \exp(Si)$.

A lower Si is equivalent to a smaller longitudinal salinity gradient, which via laterally differential longitudinal advection implies a smaller lateral salinity gradient. This leads to a weaker transverse circulation so that the secondary strain-induced periodic stratification, and thus the intensity of the tidal straining circulation, is maximum in a narrower channel. This functional chain is highly non-linear, though, e.g. because Si also affects the longitudinal gravitational circulation and the background stratification.

In a final step, we carry out three-dimensional simulations with non-zero river discharge and free surface elevation (section 2.4.4). These simulations qualitatively confirm the results obtained with the simplified two-dimensional model (cp. Fig. 2.2 and 2.13b).

It should be noted that the results presented in this paper apply to periodically, weakly stratified estuaries. In a permanently stratified estuary, for example, lateral straining probably has a much weaker additional effect on the stratification.

2.4.3.3. A note on stratification and mixing

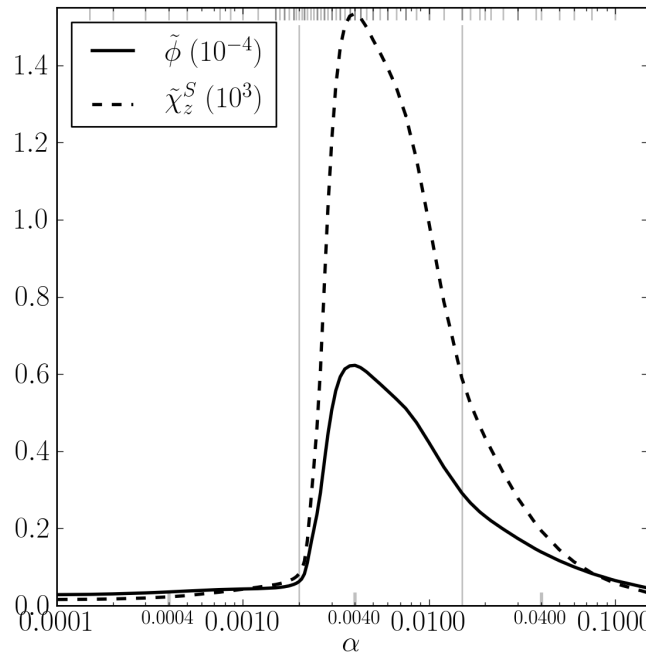


Figure 2.12.: Residual and cross-sectionally averaged non-dimensional potential density anomaly (2.30) and vertical mixing of salinity (2.32). Vertical lines and bars as in Fig. 2.2.

Stratification decreases the eddy viscosity, A_z , and thus the mixing of momentum (see section 1.3). It also decreases the eddy diffusivity, K_z , but not the mixing of salinity; this increases with stratification (see below, (2.31)). It should be noted that K_z is decreased more than A_z in a stably stratified water column, i.e. the turbulent Prandtl number is larger than one, $Pr = A_z/K_z > 1$ (Kundu and Cohen 2002).

The strength of stratification, i.e. the stability of a water column, can be measured by means of the potential density anomaly (e.g. Simpson et al. 1981; Burchard and Hofmeister 2008; de Boer

et al. 2008),

$$\phi = 1/H \int_{-H}^0 (\bar{\rho} - \rho) g z \, dz, \quad (2.29)$$

with $\bar{\rho}$ the vertically averaged density. We non-dimensionalise as follows:

$$\tilde{\phi} = \phi / (\rho_0 g H_{\max}) = 1 / (H H_{\max}) \int_{-H}^0 (\bar{\rho} - \rho) / \rho_0 z \, dz \quad (2.30)$$

with ρ_0 the reference density (see section 2.2.1).

According to Burchard et al. (2009) and Becherer and Umlauf (2011), vertical mixing of salinity can be defined as

$$\chi_z^S = 2K_z(\partial_z S)^2. \quad (2.31)$$

We non-dimensionalise as follows (cp. (2.17)):

$$\tilde{\chi}_z^S = \chi_z^S / \{H_{\max} U_* (\partial_x S)^2\} = 2\tilde{K}_z(\partial_z S / \partial_x S)^2. \quad (2.32)$$

The residual and cross-sectionally averaged non-dimensional potential density anomaly and vertical mixing are shown in Fig. 2.12. They behave very similar, i.e. both stratification and vertical mixing are weak in wide, strong in medium and moderate in narrow channels. They are maximum at the same aspect ratio as the intensity of the tidal straining circulation (Fig. 2.2; $\alpha_m = 0.004$).

2.4.4. Three-dimensional approach

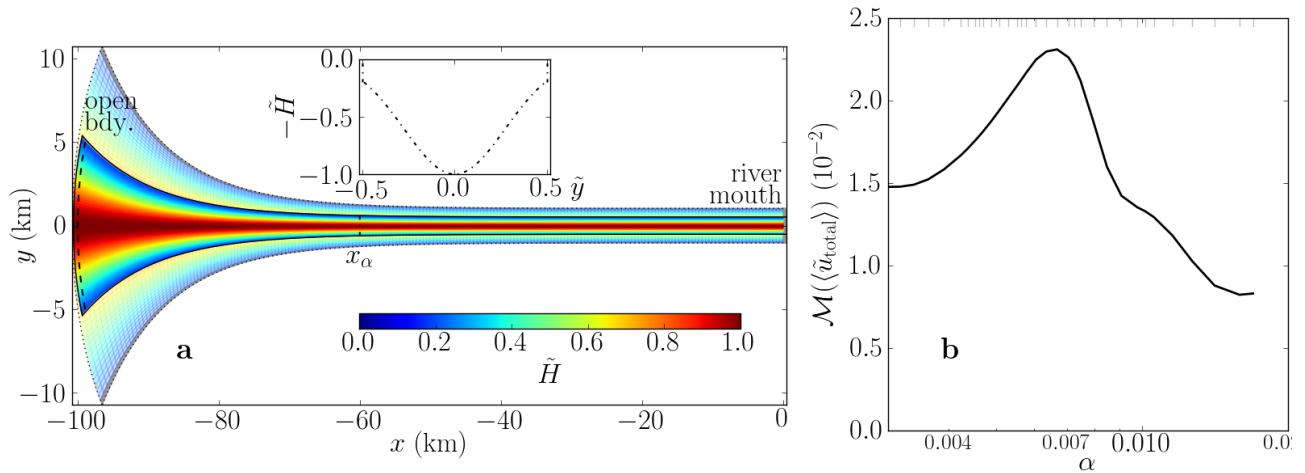


Figure 2.13.: **a** Topography of the three-dimensional model for $W_{\min} = 1$ km (2 km in lighter shading). **b** Measure of the intensity of the estuarine circulation for varying aspect ratio at $x_\alpha = -60$ km; the short bars at the upper abscissa mark the $\alpha(x_\alpha)$ values of the individual simulations.

Three-dimensional simulations are carried out by means of the General Estuarine Transport Model (GETM). The model domain has a horizontal resolution of 200×60 cells and a vertical resolution of 20 σ layers with zooming toward the bottom.

prescribed parameters			values / ranges
	L	length (from river mouth to open bdy.)	100 km
★	$W_{\max} = 10W_{\min}$	maximum width (open bdy.)	7.5 – 42.5 km
★	W_{\min}	minimum width (river mouth)	0.75 – 4.25 km
	H_{\max}	maximum water depth (thalweg)	15 m
	H_{\min}	minimum water depth (shoals)	3 m
	η_a	surface elevation amplitude at open bdy.	2 m
	S_a	salinity at open bdy.	32 psu
★	$Q = W_{\min} \cdot 0.1 \text{ m}^2 \text{ s}^{-1}$	river discharge ($S = 0$ psu)	75 – 425 $\text{m}^3 \text{ s}^{-1}$
★	$\alpha(x_\alpha) = H_{\max}/W(x_\alpha)$	aspect ratio at $x_\alpha = -60$ km	0.003 – 0.017

Table 2.4.: Parameters for the three-dimensional simulations. The stars mark varied parameters; others are invariant.

The topography is shown in Fig. 2.13a. The initial salinity decreases linearly from S_a at the open boundary, $x = -L$, to 0 at $x = -L/2$ and is 0 between $x = -L/2$ and the river mouth, $x = 0$. The prescribed parameters are listed in Tab. 2.4.

The model is forced by a constant river discharge and an M_2 tidal surface elevation at the open boundary (ω and T as in Tab. 2.1),

$$\eta_{\text{bdy}}(t) = \eta_a \sin(\omega t). \quad (2.33)$$

Simulations are started from rest and run for 20 tidal cycles to ensure periodicity.

The aspect ratio is varied by means of the width (about 30 simulations); the river discharge is scaled accordingly (see Tab. 2.4) in order to yield comparable residual velocities. The intensity of the estuarine circulation is analysed at $x_\alpha = -60$ km, which lies at the up-estuary end of the convergence zone.

It should be noted that the convergence increases with the width, but it is very weak at x_α (convergence number $\text{Co} = 2.9 \cdot 10^{-4} - 3.2 \cdot 10^{-4}$, cp. Burchard et al. 2014; i.e. increasing by a factor of 1.1 over the covered α range). Here, the amplitude of the cross-sectionally averaged longitudinal velocity is about 1.3 m s^{-1} and the residual cross-sectionally averaged longitudinal salinity gradient is about $-4 \cdot 10^{-4} \text{ psu m}^{-1}$. The salinity field exhibits weak primary SIPS (not shown, cp. Fig. 5.2c).

The impact of the aspect ratio on the intensity of the estuarine circulation is shown in Fig. 2.13b. The intensity has a maximum at $\alpha \approx 0.0067$. Like with the two-dimensional model (Fig. 2.2), this is due to a maximum of the tidal straining circulation (cp. section 5.3), which is again related to secondary SIPS (not shown, cp. Fig. 5.2i).

For conclusions, please be referred to section 6.1.

Chapter 3

More on the tidal straining circulation

The previous chapter explains how the intensity of the tidal straining circulation is maximum for a certain, medium aspect ratio due to secondary strain-induced periodic stratification (sections 2.4.1.3 and 2.4.2.1). In addition to that numerical study, an analytical derivation of the aspect ratio leading to maximum 2SIPS at slack after flood and thus to maximum intensity of the tidal straining circulation is presented here. Then, this circulation contribution is decomposed and further investigated by means of reduced numerical experiments (section 3.2).

3.1. Estimation of the aspect ratio leading to maximum intensity of the tidal straining circulation

Let us assume an initial state with zero transverse circulation, $v = w = 0$, and zero lateral and vertical buoyancy gradients, $\partial_y b = \partial_z b = 0$. An up-estuary velocity, $u > 0$ (flood direction), over a topography $\partial_y H > 0$ (left half of channel cross-section, looking down-estuary; Fig. 2.1a) is higher over the deeper part of the channel, i.e. $\partial_y u > 0$. Combined with a longitudinal buoyancy gradient, $[\partial_x b] > 0$ ([.] prescribed), this laterally differential longitudinal advection leads to a lateral buoyancy gradient, $\partial_y b < 0$ (saltier at thalweg). The related baroclinic pressure gradient drives a lateral circulation with $v < 0$ (toward shoal) near the bottom and, due to the thus created barotropic pressure gradient, $v > 0$ (toward thalweg) at the surface (also see section 1.4).

When vertical mixing reduces after full flood, $|\partial_z v|$ increases. At the surface, fresher water is moved toward the thalweg and, near the bottom, saltier water is moved toward the shoals so that stable stratification, $\partial_z b > 0$, is induced by the lateral circulation during flood. This is part of the process of *secondary strain-induced periodic stratification (2SIPS)* (sections 2.4.2.2, Fig. 2.8). Analogous processes act after full ebb, though with longitudinal velocities, lateral gradients and lateral velocities in the opposite directions. 2SIPS has a period of $T/2$ (with T the period of the longitudinal tidal current and primary, 1SIPS) and is maximum (i.e. strongest stratification) shortly after slack tides and minimum around full tides. (It should be noted that there are non-linear interactions with 1SIPS and other processes, see section 2.4.2.3.)

The idea is now to calculate or at least estimate that aspect ratio, $\alpha = H_{\max}/W$, for which the fresher water which moves toward the thalweg at the surface during flood (precisely, during the second half of the flood phase) just reaches the thalweg at slack after flood (3.1). This state means maximum possible stratification already at the beginning of the ebb phase and, due to the

consequently strong tidal asymmetry in viscosity and shear, a very strong tidal straining circulation (section 2.4.1.3).

If the fresher water does not reach the thalweg (α too small), stratification does not reach its optimum. If it reaches the thalweg before slack after flood and then moves further (downward at thalweg; α too large), stratification is maximum before slack after flood and then reduced by stirring.

Since the flood-induced lateral circulation experiences positive feedback (see Lerczak and Geyer 2004) and is thus stronger than the ebb-induced one, only the former is considered. Furthermore, too strong (ebb-induced) stratification at the beginning of the flood phase would weaken the tidal asymmetry and the intensity of the tidal straining circulation.

The tidal phase of interest is the second half of the flood phase, i.e. from full flood ($t = T/4$) till slack after flood ($t = T/2$). The vertical position of interest is the surface ($z = 0$). In the lateral direction, the half-cross-sectional average is used. The condition above can be written as follows:

$$v_{\text{int}} \frac{T}{4} = \frac{W}{2} \quad (3.1)$$

$$\text{with } v_{\text{int}} = \frac{4}{T} \int_{T/4}^{T/2} \frac{2}{W} \int_0^{W/2} v(z=0) dy dt. \quad (3.2)$$

Let us start with the equations (4a), (4b), (5), (6), (8) and (9) from Burchard et al. (2011) (cp. section 2.2.1) but ignoring mixing along σ layers ($A_s = 0$) and Coriolis ($f = 0$):

$$\partial_t u + \partial_y(uv) + \partial_z(uw) - \partial_z(A_z \partial_z u) = \int_z^0 [\partial_x b] dz' - [P_x], \quad (3.3)$$

$$\partial_t v + \partial_y(vv) + \partial_z(vw) - \partial_z(A_z \partial_z v) = \int_z^0 \partial_y b dz' - P_y, \quad (3.4)$$

$$b = -g\beta S, \quad (3.5)$$

$$\partial_y v + \partial_z w = 0, \quad (3.6)$$

$$\int_{-H}^0 v dz = 0, \quad (3.7)$$

$$\partial_t S + u[\partial_x S] + v\partial_y S + w\partial_z S - \partial_z(K_z \partial_z S) = 0. \quad (3.8)$$

For the cross-sectionally averaged longitudinal flow, the following condition applies:

$$\bar{u} = \frac{\int_0^W \int_{-H}^0 u dz dy}{\int_0^W H dy} = \frac{\int_0^{W/2} \int_{-H}^0 u dz dy}{\int_0^{W/2} H dy} = [U] \sin(\omega t). \quad (3.9)$$

Note that the bathymetry is considered to be symmetric with respect to $W/2$ and that river flow is ignored.

Following the chain of course described above,

$$u, \partial_y H \Rightarrow \partial_y u, \quad (3.10)$$

$$\partial_y u, [\partial_x b] \Rightarrow \partial_y b, \quad (3.11)$$

$$\partial_y b \Rightarrow v, \quad (3.12)$$

we now derive equations to solve the condition (3.1) for $\alpha = H_{\max}/W$.

First, the lateral barotropic pressure gradient function is calculated from (3.4). In agreement with the initial assumption of zero transverse circulation, advection and diffusion are ignored. For simplicity, the lateral buoyancy gradient is assumed to be depth-independent:

$$\begin{aligned} \partial_t v &= \int_z^0 \partial_y b \, dz' - P_y = -\partial_y b z - P_y & | \int_{-H}^0 dz, \text{ with (3.7) (rigid lid)} \\ 0 &= \frac{1}{2} \partial_y b H^2 - P_y H \\ P_y(y, t) &= \frac{1}{2} \partial_y b H \end{aligned} \quad (3.13)$$

Note that $\partial_y b(y, t)$ is zero at the thalweg so that P_y and v are also zero there.

Second, the longitudinal barotropic pressure gradient function is calculated from (3.3), again ignoring advection and diffusion and assuming the longitudinal buoyancy gradient to be constant:

$$\partial_t u = \int_z^0 [\partial_x b] \, dz' - [P_x] = -[\partial_x b] z - [P_x] \quad | \int_{-H}^0 dz \quad (3.14)$$

$$\begin{aligned} \int_{-H}^0 \partial_t u \, dz &= \frac{1}{2} [\partial_x b] H^2 - [P_x] H & | \int_0^{W/2} dy, \text{ with (3.9)} \\ [U] \omega \cos(\omega t) \int_0^{W/2} H \, dy &= \frac{1}{2} [\partial_x b] \int_0^{W/2} H^2 \, dy - \int_0^{W/2} [P_x] H \, dy \end{aligned} \quad (3.15)$$

For simplicity, the bathymetry is assumed to be linear with $H(0) = 0$ and $H(W/2) = H_{\max}$:

$$\begin{aligned} H(y) &= \frac{H_{\max}}{W/2} y = 2\alpha y, \\ \int_0^{W/2} H \, dy &= \frac{1}{4} \alpha W^2, \\ \int_0^{W/2} H^2 \, dy &= \frac{1}{6} \alpha^2 W^3. \end{aligned} \quad (3.16)$$

Inserting into (3.15) yields

$$\frac{1}{4} \alpha W^2 [U] \omega \cos(\omega t) = \frac{1}{12} \alpha^2 W^3 [\partial_x b] - 2\alpha \int_0^{W/2} [P_x] y \, dy. \quad (3.17)$$

Let us assume $[P_x]$ to be periodic in time (tidal part) and linear in the lateral direction (analogue to the baroclinic pressure gradient, $[\partial_x b]z$ (3.14), since the depth is linear):

$$\begin{aligned} [P_x](y, t) &= c_1 \cos(\omega t) + c_2 y, \\ \int_0^{W/2} [P_x] y \, dy &= \frac{1}{8} W^2 c_1 \cos(\omega t) + \frac{1}{24} W^3 c_2. \end{aligned} \quad (3.18)$$

Coefficient comparison with (3.17) and using (3.16) for substituting α yields

$$\begin{aligned} c_1 &= -[U]\omega, \quad c_2 = \alpha[\partial_x b], \\ [P_x](y, t) &= \frac{1}{2}[\partial_x b]H(y) - [U]\omega \cos(\omega t). \end{aligned} \quad (3.19)$$

Now, we follow the chain of course described above, starting with (3.10), i.e. the calculation of $\partial_y u$ at full flood. (3.3) is transformed under the following assumptions: $\partial_t u = 0$ (cp. (3.9) at $t = T/4$), $v = w = 0$ and constant A_z . The boundary conditions are $u(-H) = 0$ and $\partial_z u(0) = 0$:

$$\begin{aligned} -A_z \partial_z^2 u &= \int_z^0 [\partial_x b] dz' - [P_x] = -[\partial_x b]z - [P_x] & | \int_{z'}^0 dz \\ A_z \partial_z u &= \frac{1}{2}[\partial_x b]z'^2 + [P_x]z' & | \int_{-H}^z dz' \\ A_z u &= \frac{1}{6}[\partial_x b](z^3 + H^3) + \frac{1}{2}[P_x](z^2 - H^2) & | \frac{1}{A_z} \partial_y, \text{ with (3.19)} \\ \partial_y u &= \frac{1}{A_z} \partial_y H \left\{ \frac{1}{4}[\partial_x b](z^2 - H^2) + H[U]\omega \cos(\omega t) \right\} \end{aligned} \quad (3.20)$$

The next step is (3.11), i.e. the calculation of $\partial_y b$ at full flood. (3.8) is transformed using (3.5) and the assumptions $v = w = 0$ and $\partial_z b = 0$.

$$\begin{aligned} \partial_t b + u[\partial_x b] &= 0 & | \partial_y \\ \partial_t \partial_y b + [\partial_x b] \partial_y u &= 0 & | \int dt, \text{ with (3.20)} \\ \partial_y b &= -\frac{[\partial_x b]}{A_z} \partial_y H \left\{ \frac{1}{4}[\partial_x b](z^2 - H^2)t + H[U] \sin(\omega t) \right\} \end{aligned} \quad (3.21)$$

The second-to-last step is (3.12), i.e. the calculation of v . (3.4) is transformed using (3.13) and ignoring advection and diffusion for simplicity:

$$\begin{aligned} \partial_t v &= \int_z^0 \partial_y b dz' - P_y = -\partial_y b \left(z + \frac{1}{2}H \right) & | \int dt, \text{ with (3.21)} \\ v &= \frac{[\partial_x b]}{A_z} \partial_y H \left(z + \frac{1}{2}H \right) \left\{ \frac{1}{8}[\partial_x b](z^2 - H^2)t^2 - H \frac{[U]}{\omega} \cos(\omega t) \right\} \end{aligned} \quad (3.22)$$

Finally, the condition (3.1) is solved for α using (3.2):

$$\begin{aligned} \frac{W}{2} &= \int_{T/4}^{T/2} \frac{2}{W} \int_0^{W/2} v(z=0) dy dt & | \text{ with (3.22)} \\ &= -\frac{[\partial_x b]}{A_z W} \int_{T/4}^{T/2} \int_0^{W/2} \left\{ \frac{1}{32}[\partial_x b] \partial_y H^4 t^2 + \frac{1}{3} \partial_y H^3 \frac{[U]}{\omega} \cos(\omega t) \right\} dy dt & | \text{ with (3.16)} \\ &= -\frac{[\partial_x b]}{A_z W} \int_{T/4}^{T/2} \left\{ \frac{1}{32}[\partial_x b] H_{\max}^4 t^2 + \frac{1}{3} H_{\max}^3 \frac{[U]}{\omega} \cos(\omega t) \right\} dt \end{aligned}$$

$$\begin{aligned}
 &= -\frac{1}{3} \frac{[\partial_x b]}{A_z} \frac{H_{\max}^3}{W} \left\{ \frac{1}{32} [\partial_x b] H_{\max} t^3 + \frac{[U]}{\omega^2} \sin(\omega t) \right\} \Big|_{T/4}^{T/2} \quad \Big| \text{ with } \omega = \frac{2\pi}{T} \\
 &= -\frac{1}{12} \frac{[\partial_x b]}{A_z} \frac{H_{\max}^3}{W} T^2 \left(\frac{7}{512} [\partial_x b] H_{\max} T - \frac{[U]}{\pi^2} \right) \quad \Big| \cdot \frac{2W}{H_{\max}^2} \Big|^{-1/2} \\
 \alpha &= \left\{ \frac{1}{6} \frac{[\partial_x b]}{A_z} H_{\max} T^2 \left(\frac{[U]}{\pi^2} - \frac{7}{512} [\partial_x b] H_{\max} T \right) \right\}^{-1/2} \quad (3.23)
 \end{aligned}$$

For comparison with the model results, the following parameters are used (section 2.3.2, Tab. 2.1): $\partial_x S = -2 \cdot 10^{-4} \text{ psu m}^{-1}$ ($\Rightarrow \partial_x b = 1.5 \cdot 10^{-6} \text{ s}^{-2}$), $A_z = 1.5 \cdot 10^{-2} \text{ m}^2 \text{ s}^{-1}$ (residual cross-sectionally averaged eddy viscosity of very wide channel, quasi-onedimensional), $H_{\max} = 15 \text{ m}$, $T = 44714 \text{ s}$ and $[U] = U_t = 1 \text{ m s}^{-1}$. They yield

$$\alpha = 0.0048. \quad (3.24)$$

Considering the assumptions and simplifications made, this is remarkably close to $\alpha_m = 0.004$, where the intensity of the tidal straining circulation is maximum in the simulations (section 2.4.1.1, Fig. 2.2).

3.2. Detailed investigation of the tidal straining circulation and the reduced experiments

Since the tidal straining circulation is often the dominant contribution and responsible for the maximum of the estuarine circulation intensity in medium wide channels (section 2.4.1), it is investigated further. For that purpose, differences in shear, eddy viscosity and stratification between the full and the reduced experiments are analysed. The experiments are listed in Tab. 3.1 together with the respective intensity of the estuarine circulation contributions in the medium channel.

exp.	mom.	sal.	total	strain.	grav.	advec.	other
A	☑	☑	6.769	5.556	0.560	0.534	0.118
C	☐	☑	2.676	2.270	0.408	0.000	-0.001
D	☐	☐	1.335	0.971	0.278	0.000	0.086
F	☑	☐	1.016	0.696	0.255	-0.002	0.068

Table 3.1.: Measure of the intensity of the residual longitudinal circulation contributions, $\mathcal{M}(\langle \tilde{u}_i \rangle)$ (10^{-2}), for the different experiments in the maximum-straining scenario (medium wide channel, $\alpha = 0.004$; other parameters as in Tab. 2.1). The checked boxes, ☑, indicate the process/-es which is/are included (☐ excluded) in the respective experiment (mom. momentum, sal. transverse salinity advection; cp. section 2.3.1).

It should be noted that experiment D is not just a combination of the experiments C and F. Instead of excluding both momentum advection (C) and transverse salinity advection (F), the lateral internal pressure gradient is excluded from the lateral momentum equation (D; section 2.3.1, appendix A.4). Thus, there is no transverse circulation in experiment D ($v = w = 0$) but in the experiments C and F ($v, w \neq 0$ and $\partial_z v, \partial_y w \neq 0$). This has consequences for the eddy viscosity and diffusivity and should be kept in mind (also see section 3.2.3F).

Please also note that these experiments are purely theoretical. They do not have an analogue in real estuaries and cannot even be conducted in a laboratory, to my knowledge. Still, their analysis can give important insights into the interaction of otherwise inseparable processes.

3.2.1. Method: Decomposition of the tidal straining circulation

The driver of the tidal straining circulation is the covariance of the eddy viscosity and the vertical shear of the longitudinal velocity divided by the residual viscosity,

$$\mathcal{A}_{\text{strain}} = -\langle A'_z \partial_z u' \rangle / \langle A_z \rangle, \quad (2.22)$$

so that Burchard and Schuttelaars (2012) called it *covariance circulation*. Following their method, the tidal straining circulation in an experiment \mathcal{E} can be decomposed into the contribution from a reduced experiment \mathcal{R} (C, D or F; see section 2.3.1 or next section) and three contributions arising from the differences in viscosity and shear between the reduced and the full or less reduced experiment (A, C or F). Note that Burchard and Schuttelaars (2012) only used the full experiment, A, as \mathcal{E} , but here also C and F are compared to D.

$[A'_z]_{\mathcal{E}}$ ($[A'_z]_{\mathcal{R}}$) denotes the eddy viscosity fluctuation, $A'_z = A_z - \langle A_z \rangle$, resulting from experiment \mathcal{E} (\mathcal{R}); $[u']_{\mathcal{E}}$ ($[u']_{\mathcal{R}}$) denotes the longitudinal velocity fluctuation from experiment \mathcal{E} (\mathcal{R}). The differences in the viscosity and velocity fluctuations between the experiments are

$$\begin{aligned} [A'_z]_{\mathcal{E}-\mathcal{R}} &= [A'_z]_{\mathcal{E}} - [A'_z]_{\mathcal{R}} \\ \text{and } [u']_{\mathcal{E}-\mathcal{R}} &= [u']_{\mathcal{E}} - [u']_{\mathcal{R}}. \end{aligned}$$

Thus, the covariance of eddy viscosity and vertical shear of the longitudinal velocity resulting from experiment \mathcal{E} can be decomposed:

$$\begin{aligned} &\langle [A'_z]_{\mathcal{E}} \partial_z [u']_{\mathcal{E}} \rangle \\ &= \langle [A'_z]_{\mathcal{R}} \partial_z [u']_{\mathcal{R}} \rangle + \langle [A'_z]_{\mathcal{R}} \partial_z [u']_{\mathcal{E}-\mathcal{R}} \rangle + \langle [A'_z]_{\mathcal{E}-\mathcal{R}} \partial_z [u']_{\mathcal{R}} \rangle + \langle [A'_z]_{\mathcal{E}-\mathcal{R}} \partial_z [u']_{\mathcal{E}-\mathcal{R}} \rangle. \end{aligned} \quad (3.25)$$

Recursively inserting (3.25) into $\mathcal{A}_{\text{strain}}$ (2.22), the result into $\langle \tilde{u}_{\text{strain}} \rangle$ (2.20) and this into $\mathcal{M}(\langle \tilde{u}_{\text{strain}} \rangle)$ (2.25) yields

$$\mathcal{M}_{\mathcal{E},\mathcal{E}} = \mathcal{M}_{\mathcal{R},\mathcal{R}} + \mathcal{M}_{\mathcal{R},\mathcal{E}-\mathcal{R}} + \mathcal{M}_{\mathcal{E}-\mathcal{R},\mathcal{R}} + \mathcal{M}_{\mathcal{E}-\mathcal{R},\mathcal{E}-\mathcal{R}}. \quad (3.26)$$

For the sake of convenience, the term $\mathcal{M}_{\mathcal{E},\mathcal{E}}$ represents $\mathcal{M}(\langle \tilde{u}_{\text{strain}} \rangle_{\mathcal{E},\mathcal{E}})$ calculated with

$$[\mathcal{A}_{\text{strain}}]_{\mathcal{E},\mathcal{E}} = -\langle [A'_z]_{\mathcal{E}} \partial_z [u']_{\mathcal{E}} \rangle / \langle A_z \rangle_{\mathcal{E}}.$$

It should be noted that the residual eddy viscosity used in γ (2.21) and $\mathcal{A}_{\text{strain}}$ (2.22) is that from experiment \mathcal{E} also in the four terms on the right-hand side, e.g. the term $\mathcal{M}_{\mathcal{R},\mathcal{E}-\mathcal{R}}$ represents $\mathcal{M}(\langle \tilde{u}_{\text{strain}} \rangle_{\mathcal{R},\mathcal{E}-\mathcal{R}})$ calculated with

$$[\mathcal{A}_{\text{strain}}]_{\mathcal{R},\mathcal{E}-\mathcal{R}} = -\langle [A'_z]_{\mathcal{R}} \partial_z [u']_{\mathcal{E}-\mathcal{R}} \rangle / \langle A_z \rangle_{\mathcal{E}}.$$

This decomposition (3.26) allows to quantify the contribution of

$$\begin{aligned} \mathcal{M}_{\mathcal{R},\mathcal{E}-\mathcal{R}} & \text{ shear fluctuations,} \\ \mathcal{M}_{\mathcal{E}-\mathcal{R},\mathcal{R}} & \text{ viscosity fluctuations and} \\ \mathcal{M}_{\mathcal{E}-\mathcal{R},\mathcal{E}-\mathcal{R}} & \text{ the viscosity-shear covariance} \end{aligned}$$

added to the dynamics of the reduced experiment, \mathcal{R} , by the process(es) included in experiment \mathcal{E} but not in experiment \mathcal{R} .

In order to quantify the contribution of changes of the residual eddy viscosity, an additional term is introduced here: $\mathcal{M}_{\mathcal{R},\mathcal{R}^*}$ represents $\mathcal{M}(\langle \tilde{u}_{\text{strain}} \rangle_{\mathcal{R},\mathcal{R}^*})$ calculated with the residual viscosity from experiment \mathcal{R} in γ (2.21) and $\mathcal{A}_{\text{strain}}$ (2.22),

$$[\mathcal{A}_{\text{strain}}]_{\mathcal{R},\mathcal{R}^*} = -\langle [A'_z]_{\mathcal{R}} \partial_z [u']_{\mathcal{R}} \rangle / \langle A_z \rangle_{\mathcal{R}}.$$

It should be noted that $\mathcal{M}_{\mathcal{E},\mathcal{E}}$ and $\mathcal{M}_{\mathcal{R},\mathcal{R}^*}$ (Tab. 3.2) slightly differ from $\mathcal{M}(\langle \tilde{u}_{\text{strain}} \rangle)$ (Tab. 3.1; Fig. 2.9a) because a simplified analysis is applied. However, this does not affect the meaning of the decomposition results.

3.2.2. Results and discussion of the tidal straining decomposition

Before interpreting the results, please recall which processes are (not) included in the different experiments (e.g. left part of Tab. 3.1). The results of the decomposition (3.26) are shown in Tab. 3.2. They are explained line by line, focussing on those pairs of experiments where \mathcal{E} and \mathcal{R} differ only by transverse salinity advection (A-F and C-D). For these pairs, the process of secondary strain-induced periodic stratification (2SIPS) is included in experiment \mathcal{E} but not in experiment \mathcal{R} . Please recall that 2SIPS plays an important role for the maximum of the intensity of the tidal straining circulation in medium wide channels (section 2.4.2).

	\mathcal{E}	\mathcal{R}	$\mathcal{M}_{\mathcal{E},\mathcal{E}}$	$\mathcal{M}_{\mathcal{R},\mathcal{E}-\mathcal{R}}$	$\mathcal{M}_{\mathcal{E}-\mathcal{R},\mathcal{R}}$	$\mathcal{M}_{\mathcal{E}-\mathcal{R},\mathcal{E}-\mathcal{R}}$	$\mathcal{M}_{\mathcal{R},\mathcal{R}}$	$\mathcal{M}_{\mathcal{R},\mathcal{R}^*}$	mom.	sal.
$\mathcal{M}_{\dots} (10^{-2})$	A	C	5.556	6.153	-1.336	-2.648	3.386	2.273	✓	□
	A	D	5.556	5.844	-0.889	-1.578	2.179	0.992	✓	✓
	A	F	5.556	4.682	-0.583	-0.215	1.673	0.715	□	✓
	C	D	2.273	0.191	0.028	0.533	1.521	0.992	□	✓
	F	D	0.715	-0.159	-0.093	0.061	0.906	0.992	✓	□
$\mathcal{M}_{\dots}/\mathcal{M}_{\mathcal{E},\mathcal{E}}$	A	C	1.000	1.107	-0.240	-0.477	0.609	0.409	✓	□
	A	D	1.000	1.052	-0.160	-0.284	0.392	0.179	✓	✓
	A	F	1.000	0.843	-0.105	-0.039	0.301	0.129	□	✓
	C	D	1.000	0.084	0.012	0.234	0.669	0.436	□	✓
	F	D	1.000	-0.222	-0.130	0.085	1.267	1.387	✓	□

Table 3.2.: Measure of the intensity of the covariance contributions for different pairs of experiments \mathcal{E} and \mathcal{R} in the maximum-straining scenario (medium wide channel, $\alpha = 0.004$; other parameters as in Tab. 2.1). The checked boxes, ✓, in the right columns indicate the process/-es which is/are added when going from experiment \mathcal{R} to experiment \mathcal{E} (mom. momentum, sal. transverse salinity advection).

The upper half contains $\mathcal{M}(\langle \tilde{u}_{\text{strain}} \rangle_{\dots}) (10^{-2})$; the lower half contains relative values with respect to $\mathcal{M}_{\mathcal{E},\mathcal{E}}$ (subscripts as in section 3.2.1).

C-D $\mathcal{M}_{\mathcal{R},\mathcal{R}}$ (calculated with $1/\langle A_z \rangle_{\mathcal{E}}$) is larger than $\mathcal{M}_{\mathcal{R},\mathcal{R}^*}$ (calculated with $1/\langle A_z \rangle_{\mathcal{R}}$) by a factor of about 1.5. This means that transverse salinity advection significantly decreases the residual eddy viscosity, i.e. that it increases the residual stratification (Fig. 3.1e**C,fC** vs. **eD,fD**, also Fig. 2.9c) by means of laterally and vertically advected and strain-induced periodic stratification (2/3ASIPS, section 2.4.2.2; e.g. Fig. 3.3e**C** vs. **eD**).

The contribution of changing viscosity fluctuations is comparably unimportant ($\mathcal{M}_{\mathcal{E}-\mathcal{R},\mathcal{R}}$, 1.2% of $\mathcal{M}_{\mathcal{E},\mathcal{E}}$). Changes of shear fluctuations contribute 8.4% ($\mathcal{M}_{\mathcal{R},\mathcal{E}-\mathcal{R}}$), the increased viscosity-shear covariance 23% ($\mathcal{M}_{\mathcal{E}-\mathcal{R},\mathcal{E}-\mathcal{R}}$) (Fig. 3.2b**C,cC** vs. **bD,cD**).

Thus, when momentum advection is excluded, the main effects of transverse salinity advection are a reduction of the residual eddy viscosity and an increase of the viscosity-shear covariance, both of which contribute positively to the tidal straining circulation so that its intensity is more than doubled ($\mathcal{M}_{\mathcal{E},\mathcal{E}}$ vs. $\mathcal{M}_{\mathcal{R},\mathcal{R}^*}$).

F-D When transverse salinity advection is excluded, momentum advection has a negative effect on the intensity of the tidal straining circulation. The residual eddy viscosity increases slightly ($\mathcal{M}_{\mathcal{R},\mathcal{R}}$ smaller than $\mathcal{M}_{\mathcal{R},\mathcal{R}^*}$, Fig. 3.1e**F** vs. **eD**, also Fig. 2.9c) and changes of both viscosity and shear fluctuations contribute negatively ($\mathcal{M}_{\mathcal{E}-\mathcal{R},\mathcal{R}}$, $\mathcal{M}_{\mathcal{R},\mathcal{E}-\mathcal{R}}$) even though neither the shear nor the viscosity appear to change much (at the thalweg, Fig. 3.2b**F,cF** vs. **bD,cD**). Only the viscosity-shear covariance increases slightly ($\mathcal{M}_{\mathcal{E}-\mathcal{R},\mathcal{E}-\mathcal{R}}$) but not enough to balance the negative contributions.

A-F As C and D (see above), A and F differ only by transverse salinity advection; in contrast to C and D, A and F do include momentum advection. The intensity of the tidal straining circulation (increased by a factor of about 2.3 from D to C) is increased by a factor of about 7.8 from F to A and the covariance decomposition is totally different. Only the reduction of the residual eddy viscosity is comparable ($\mathcal{M}_{\mathcal{R},\mathcal{R}}$ larger than $\mathcal{M}_{\mathcal{R},\mathcal{R}^*}$ by a factor of about 2.3 vs. 1.5) and again due to an increase of the residual stratification (Fig. 3.1e**A,fA** vs. **eF,fF**, also Fig. 2.9c).

The viscosity-shear covariance (significantly increased from D to C) slightly decreases from F to A. The contribution of changing viscosity fluctuations (small but positive there) is negative here. Changes of shear fluctuations due to transverse salinity advection, on the other hand, contribute 10 times as much when momentum advection is included (Fig. 3.2b**A** vs. **bF**).

It should be noted at this point that, even though these terms can be separated mathematically, they still interact (similar to the estuarine circulation contributions; section 2.3.3, page 13), e.g. the eddy viscosity affects the shear, which influences the stratification and thus again the viscosity. This makes the interpretation difficult. Please also see **A-C** and section 3.2.3.

A-C The effect of momentum advection is also very different when transverse salinity advection is included instead of excluded (F-D). Only the negative contribution of changing viscosity fluctuations is comparable.

The intensity of the tidal straining circulation (decreased from D to F) is increased by a factor of about 2.4 from C to A. The residual eddy viscosity (slightly increased there) is slightly decreased here due to an increase of the residual stratification (Fig. 3.1e**A,fA** vs. **eC,fC**, also Fig. 2.9c). The viscosity-shear covariance (slightly increased from D to F) is significantly decreased from C to A. Changes of shear fluctuations, on the other hand, (negative there) are the dominant positive contribution here (Fig. 3.2b**A** vs. **bC**).

As in the comparison of the pair of experiments A-F to the pair C-D (above), the contribution from changing, i.e. increasing shear fluctuations is much larger (and positive) when both momentum advection and transverse salinity advection are included in experiment \mathcal{E} (i.e. $\mathcal{E}=A$). The two processes appear to have a positive feedback on each other in such a way that shear fluctuations and the intensity of the tidal straining circulation are largest when both processes are present. (Viscosity fluctuations also change more if $\mathcal{E}=A$, but these changes contribute negatively.) In fact, including only momentum advection (F) gives a smaller intensity of the tidal straining circulation than including neither momentum nor transverse salinity advection (D; Tab. 3.1).

A-D When both momentum advection and transverse salinity advection are added, the contributions from changing shear fluctuations, viscosity fluctuations, viscosity-shear covariance and residual eddy viscosity lie between the respective contributions when only one of the processes is added (Tab. 3.2, values in line A-D between those in lines A-C and A-F).

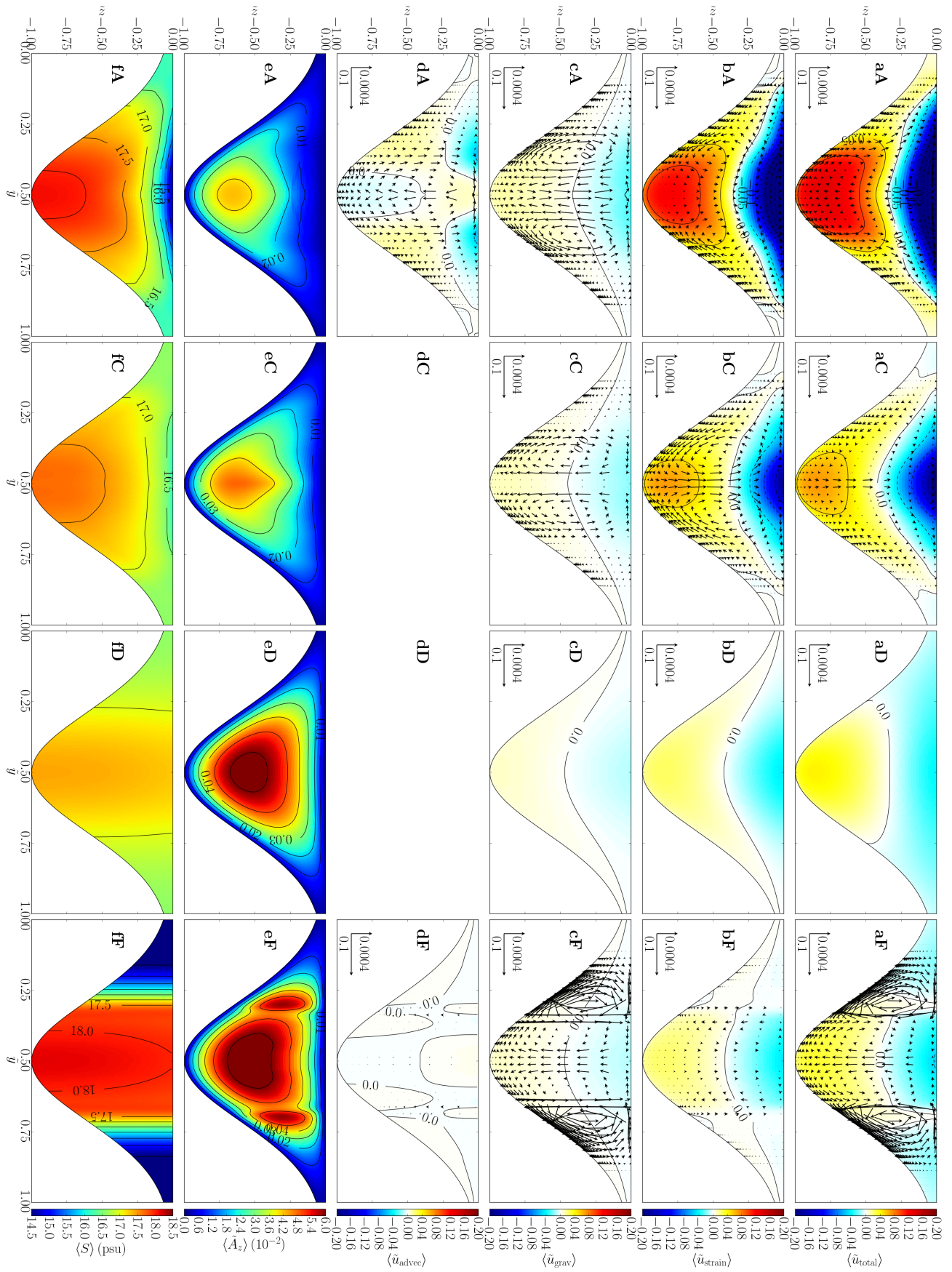
3.2.3. Interplay of momentum advection and transverse salinity advection

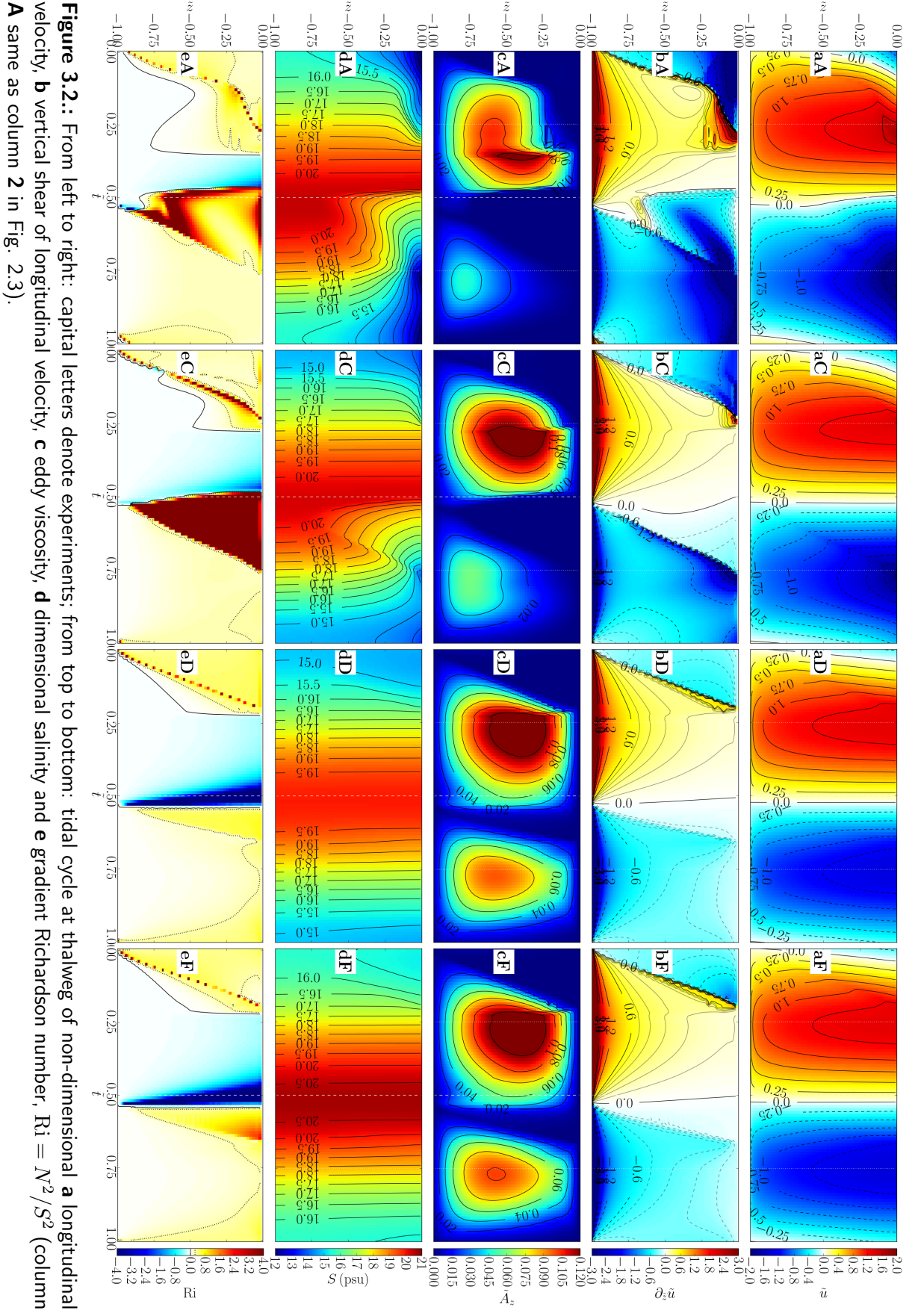
Why is the effect of momentum advection or transverse salinity advection on the shear fluctuations and, thus, on the intensity of the tidal straining circulation much stronger when the repectively other process is included ($\mathcal{E} = A$)? To understand this, please recall the mechanisms causing transverse and the advectively driven circulation (section 1.4). Each experiment is discussed with respect to these mechanisms, focussing on the tidal phase slack after flood. Stratification at that time is crucial for strong (negative) vertical shear of the longitudinal velocity during ebb, which causes a strong tidal straining circulation (section 2.4.1).

A In the full experiment, the mechanisms act as described in the introduction (section 1.4). Laterally differential longitudinal advection of salinity, $\partial_y(u\partial_x S) = \partial_y u \partial_x S$ ($\partial_x S$ constant), builds a lateral salinity gradient, $\partial_y S$ (2.3), which generates a lateral circulation, v (2.2). During flood, this circulation is surface-convergent (colour in Fig. 3.3c**A-eA**). It advects both low longitudinal momentum and low salinity from the shoals toward the thalweg, at the surface, so that isotachs (of u) and isohalines are approximately parallel to each other there and in the centre of the channel at slack after flood (contours in Fig. 3.4e**A**). (At the bottom, $u = 0$ and $\partial_z S = 0$ as required by the bottom boundary conditions.) This parallelity strongly enforces the shear-stratification feedback (sections 1.2 and 1.3): The low salinity at the surface gets lower by already ebb-directed longitudinal flow and the high salinity above the bottom gets higher by still flood-directed flow. This increase of stratification reduces the eddy viscosity and thus promotes the negative shear during ebb.

C Lateral circulation is generated as in experiment A, but it advects only the salinity so that isotachs and isohalines are approximately perpendicular to each other at the surface and in the centre of the channel at slack after flood (Fig. 3.4e**C**). Thus, there is no feedback increasing both

Figure 3.1. (following page): From left to right: capital letters denote experiments; from top to bottom: residual profile of non-dimensional **a** estuarine circulation, **b** tidal straining circulation, **c** gravitational circulation, **d** advectively driven circulation (zero in experiments C and D), **e** eddy viscosity and **f** dimensional salinity (column **A** same as column **2** in Fig. 2.3).





stratification and shear. The weaker stratification does not reduce the eddy viscosity that much, compared to A (cp. Fig. 3.2**cA** vs. **cC**). This explains why the lateral velocities are slightly smaller in C than in A (cp. Fig. 3.3**A** vs. **C** except **e** because $\partial_y S$ already nearly diminished at the surface at slack after flood in A). The smaller lateral velocities are then also responsible for the weaker stratification at slack after flood (negative feedback).

Thus, 2SIPS is weaker in C than in A, but it is still strong enough to create an ebb-flood asymmetry of eddy viscosity and shear (Fig. 3.2**bC,cC**) and a (smaller) maximum in the intensity of the tidal straining circulation (Fig. 2.9**a**).

D There is no lateral circulation (Fig. 3.3**D**) and thus no transverse advection of momentum or salinity, of course. Besides this, the probably most striking difference to the other experiments are the small lateral salinity gradients, particularly at full flood (Fig. 3.4**cD**). They can be explained as follows:

Laterally differential longitudinal advection builds a lateral salinity gradient, as above (e.g. fresher at thalweg at slack after ebb, Fig. 3.4**aD**), but this gradient is not reduced by any transverse circulation. Thus, the opposing advection during the consecutive tidal phase first has to erode that lateral salinity gradient before it can build the opposing gradient typical for this phase (e.g. more saline at thalweg at slack after flood, Fig. 3.4**eD**).

The erosion of the “old” lateral salinity gradient takes about the first half of the flood phase (minimum $\partial_y S$ around full flood, Fig. 3.4**cD**) and a bit longer during the ebb phase (not shown). One could argue that the reason for this difference is that the lateral salinity gradient is larger at slack after flood than at slack after ebb (Fig. 3.4**eD** vs. **aD**), but this is again related to the different erosion times themselves. To understand why the system is flood-dominated, other variables need to be considered. The orientation of isotachs and isohalines with respect to each other turns out to play an important role here, too (parallelity as in **A** or perpendicularity as in **C**).

Without transverse circulation, any difference between flood and ebb must be related to longitudinally generated asymmetries, i.e. to primary strain-induced periodic stratification (1SIPS). This is the only stratifying process here and, though it is comparably weak (e.g. Fig. 2.7), it causes a sufficient tidal asymmetry in stratification, eddy viscosity and shear (Fig. 3.2**bD-dD**) to generate a weak tidal straining circulation (Fig. 3.1**bD**).

Due to 1SIPS, shear is slightly stronger during (late) ebb than during (late) flood, in the upper part of the water column (Fig. 3.2**bD**). In cross-sectional view, the isotachs of u are more V-shaped during ebb and more U-shaped during flood (Fig. 3.4**gD,aD** vs. **cD,dD**). The isohalines are weakly A-shaped around full ebb (**gD**), weakly V-shaped around slack after ebb (**aD**; both stably stratified) and about vertical from full flood till slack after flood (**cD-eD**, homogeneous). Thus, the isotachs and isohalines are approximately perpendicular to each other around full ebb (**gD**) and parallel to each other during flood (**aD-eD**).

When the isotachs of u are parallel to the isohalines, the velocity field is much more effective both in eroding the salinity gradients (early flood, highest up-estuary velocity meets lowest salinity, Fig. 3.4**aD-cD**) and in enforcing the salinity gradients (late flood, highest velocity meets highest salinity, **cD-eD**; also see **A**), compared to when they are perpendicular (ebb, **gD**). Therefore, the salinity field is flood-dominated, i.e. the residual salinity increases toward the thalweg (Fig. 3.1**fD**).

F Lateral circulation is generated as in the experiments A and C, but it advects only the momentum. Thus, as in D, 1SIPS is the only stratifying process here so that stratification is weak and eddy

viscosity is high (Fig. 3.1e**F**,**fF**, 3.2c**F**,**dF**). The cross-sectionally averaged residual eddy viscosity is slightly higher in F than in D because shear (S^2) is slightly higher and stratification (N^2) is weaker in F, causing higher turbulent kinetic energy (not shown).

The high eddy viscosity reduces not only the vertical shear of the longitudinal velocity (cp. tidal straining circulation, section 1.3) but of course also the vertical shear of the lateral velocity. Thus, the lateral velocities are considerably smaller in F than in A and C (Fig. 3.3e**F** vs. e**A**,**eC**) so that the transverse advection of longitudinal momentum is weak here. Consequently, the isotachs of u in experiment F more resemble those in D than those in A and C (Fig. 3.4).

Considering these similarities to D, why is the lateral salinity gradient much stronger (Fig. 3.1f**F**) and almost always flood-oriented in F so that the transverse circulation is also almost always flood-oriented, i.e. surface-convergent (Fig. 3.3**F**)? The transverse circulation is surface-divergent only in the centre of the channel during early flood (Fig. A.1 in appendix A.5.1). This coincides with maximum stratification and maximum negative shear (Fig. 3.2b**F**,**dF**). (Note that stratification and shear are weak, compared to A and C.)

The differences to D are a higher eddy viscosity, a weaker stratification and a weak, mostly surface-convergent transverse advection of longitudinal momentum (see above). The orientation of the transverse circulation is already a consequence of the lateral salinity gradient. It should be noted again that the (non-linear) interactions between shear, stratification and eddy viscosity as well as between longitudinal and transverse processes make it very difficult or even impossible to identify one variable or process as the origin of the results, even in reduced experiments.

The salinity field in F is flood-dominated for the same reasons as in D: The isotachs of u and the isohalines are more parallel during (early) flood than during (early) ebb (Fig. 3.4a**F**-**gF**, particularly Fig. A.2 in appendix A.5.1). However, the reason for the persisting flood-orientation in F cannot be found here. The system appears to be quite sensitive to small changes in shear, stratification and eddy viscosity. Further analyses are needed to fully explain this.

To summarise, only if both advection of momentum and transverse advection of salinity are included, longitudinal velocity and salinity “synchronise” in terms of their isolines’ orientation. Their parallelity strongly enforces the shear-stratification feedback during ebb and thus the tidal straining circulation (see **A**).

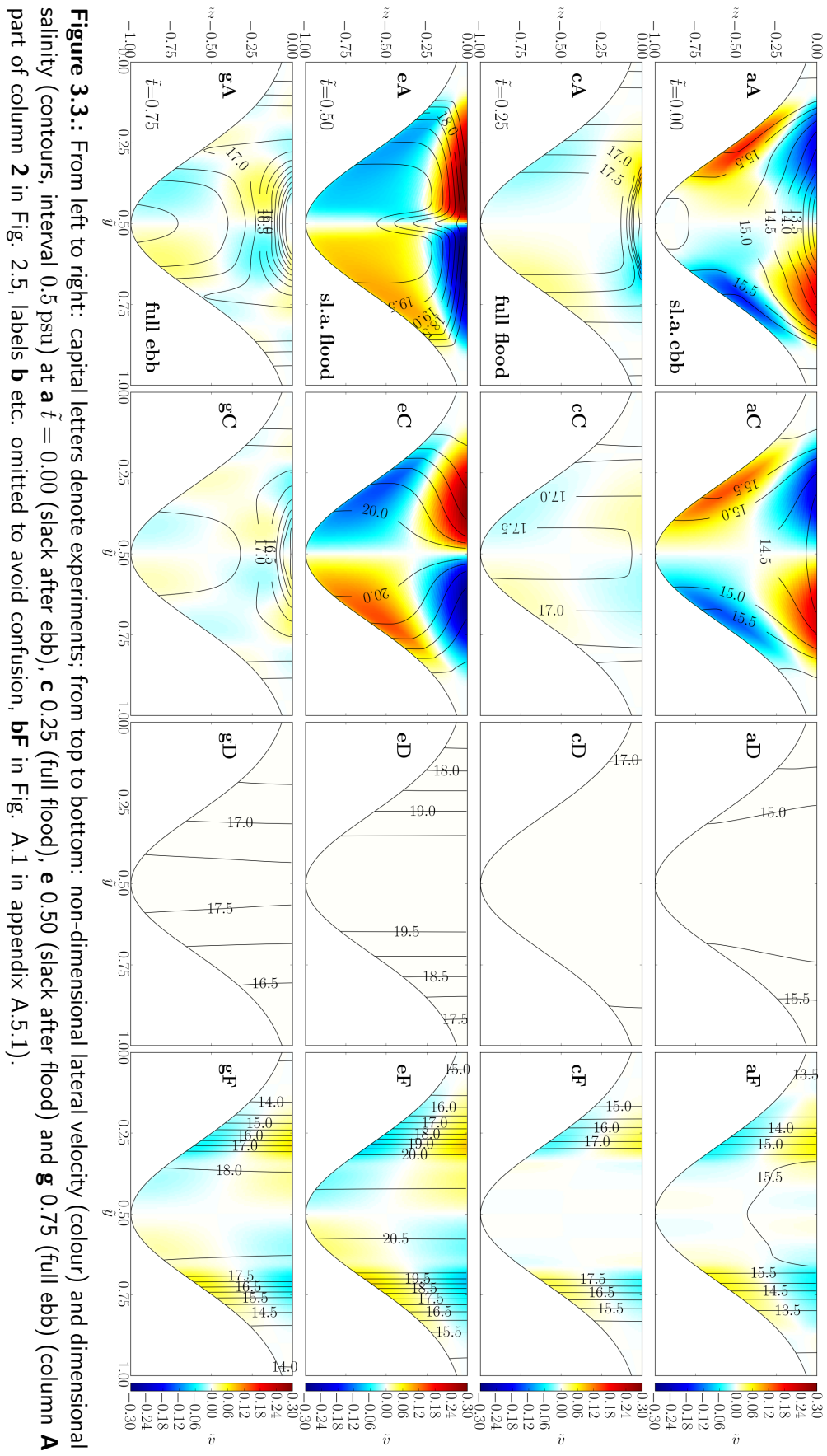
3.2.4. Gravitational and advectively driven circulation in the reduced experiments

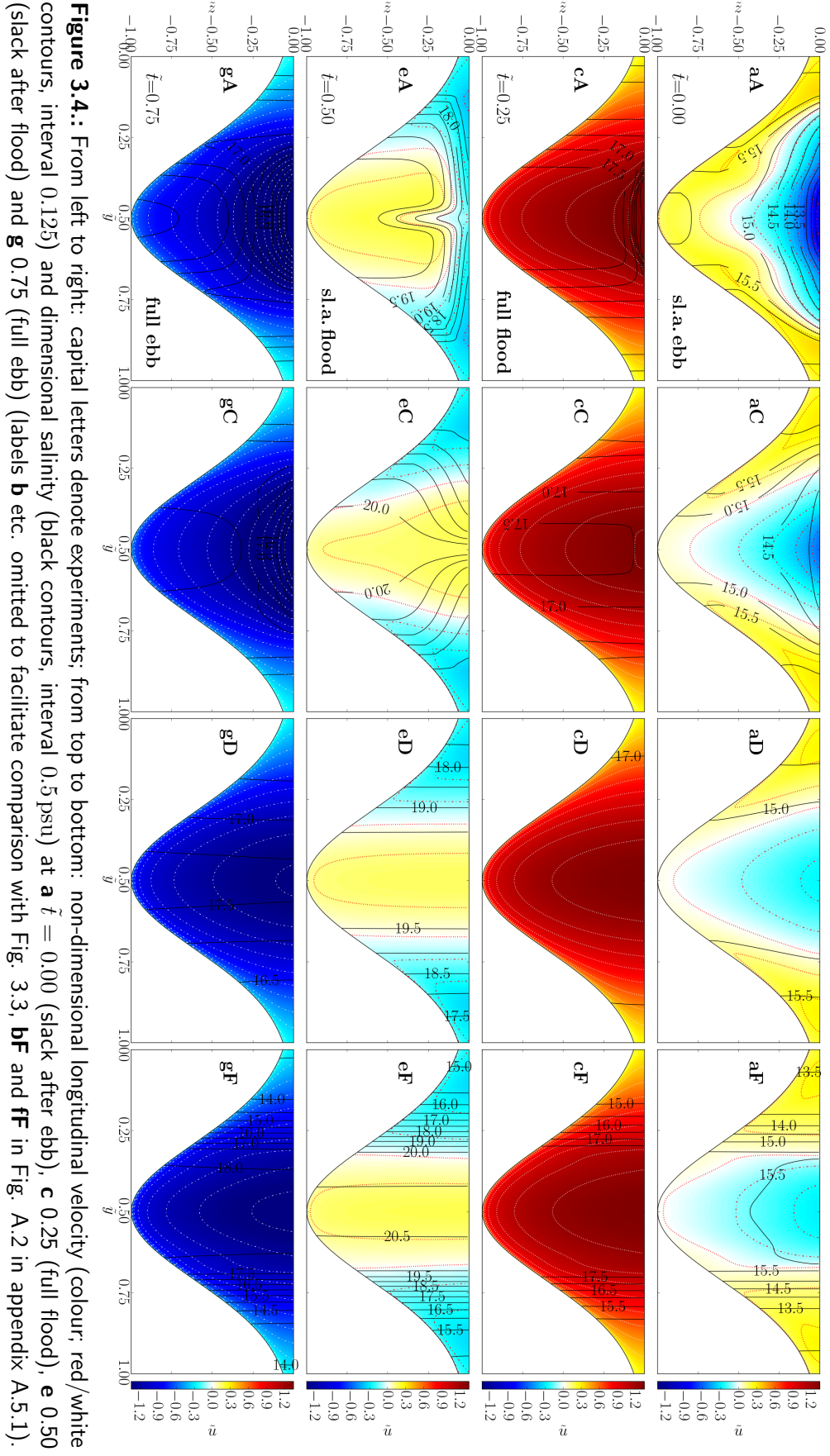
As the tidal straining circulation, also the gravitational circulation has the highest intensity when both momentum advection and transverse salinity advection are included (experiment A) and the lowest intensity when only momentum advection is included (F; Tab. 3.1, Fig. 3.1c**A**-**cF**). Considering

$$\mathcal{A}_{\text{grav}} = \int_z^0 \int_{\hat{z}}^0 \langle \partial_x b \rangle d\hat{z} dz / \langle A_z \rangle, \quad (2.23)$$

this can only be related to changes of the residual eddy viscosity since $\partial_x b$ is constant and unchanged. As shown in Fig. 3.1e**A**-**eF** (also Fig. 2.9c), the residual eddy viscosity increases when going from experiment A to C, C to D and D to F.

The advectively driven circulation is zero in the experiments C and D because it is based on the





transverse momentum advection, i.e. on v and w , which are zero in C and D,

$$\mathcal{A}_{\text{advec}} = \left\{ - \int_z^0 \partial_y \langle uv \rangle d\hat{z} + \langle uw \rangle \right\} / \langle A_z \rangle. \quad (2.24)$$

It is approximately zero in experiment F because v (and w , not shown) is not properly reversing there (Fig. 3.3F vs. A, also see section 3.2.3F) as it is necessary for the advectively driven circulation (section 1.4).

Chapter 4

Impact of other parameters on the residual along-channel circulation

There are numerous parameters which characterise an estuary and the circulation in it, as indicated in the first two chapters. The impact of the aspect ratio and the Simpson number on the residual longitudinal circulation is explained in chapter 2. The impact of the non-dimensional quasi-lateral diffusivity, the minimum-to-maximum depth ratio and the full width at half maximum depth is described here (sections 4.2-4.4). The impact of the unsteadiness number, Un , and the bottom roughness length, z_0^b , was investigated by Burchard et al. (2011, also Si, W) so that all seven non-dimensional numbers are covered now (cp. Tab. 2.1).

4.1. Convergence and other circulation contributions

The impact of lateral convergence can also be investigated with the two-dimensional model (section 2.2.1) if the longitudinal momentum equation (2.1) is extended accordingly. Please be referred to Burchard et al. (2014, equation (3), section 3.3). The convergence contribution to the estuarine circulation can then be calculated by means of the decomposition method (section 2.3.3, (2.18), (2.20); Burchard and Hetland 2010; Burchard et al. 2011).

Instead, one can also use the “error circulation”. Theoretically, the sum of all circulation contributions should equal the total residual longitudinal circulation. The discrepancy,

$$\langle \tilde{u}_{\text{err}} \rangle = \langle \tilde{u}_{\text{total}} \rangle - \sum_i \langle \tilde{u}_i \rangle, \quad (4.1)$$

arises from numerical errors, e.g. discretisation, interpolation and truncation. If this error of the full decomposition ((2.18) containing all terms of the momentum equation (2.1)) is very small, the larger error of an incomplete decomposition (e.g. not containing the convergence term) can be considered to equal the missing contribution (e.g. the convergence circulation, Burchard et al. 2014),

$$\langle \tilde{u}_{\text{conv}} \rangle = \langle \tilde{u}_{\text{err}} \rangle. \quad (4.2)$$

The other circulation in (2.18) (Fig. 2.2, 4.1) is the sum of the error and the contributions from quasi-lateral mixing and local run-off (see Burchard et al. 2011).

4.2. Impact of the quasi-lateral diffusivity

As mentioned in section 2.2.3, the intensity of the estuarine circulation depends on the non-dimensional quasi-lateral diffusivities of momentum and salinity (also see appendix A.3),

$$\tilde{A}_{y*} = A_{y*}/(WU_*). \quad (2.11)$$

Note that the RMS friction velocity, U_* , scales with the water depth, H_{\max} (via invariant Si and Un, Tab. 2.1), and that the cross-sectional area, A , scales with the width, W , and the water depth (A.13). Thus, the dimensional quasi-lateral diffusivity scales with the area,

$$A_{y*} = \tilde{A}_{y*} W U_* \propto \tilde{A}_{y*} W H_{\max} \propto \tilde{A}_{y*} A.$$

In order to investigate the impact of the quasi-lateral diffusivities of momentum and salinity on the estuarine circulation, about 50 simulations are carried out with varied diffusion coefficients. They are assigned by means of the namelist file, `getm.inp`:

$$\begin{aligned} \text{Am} &= A_{y*}, \\ \text{salt_AH} &= K_{y*} = A_{y*}. \end{aligned}$$

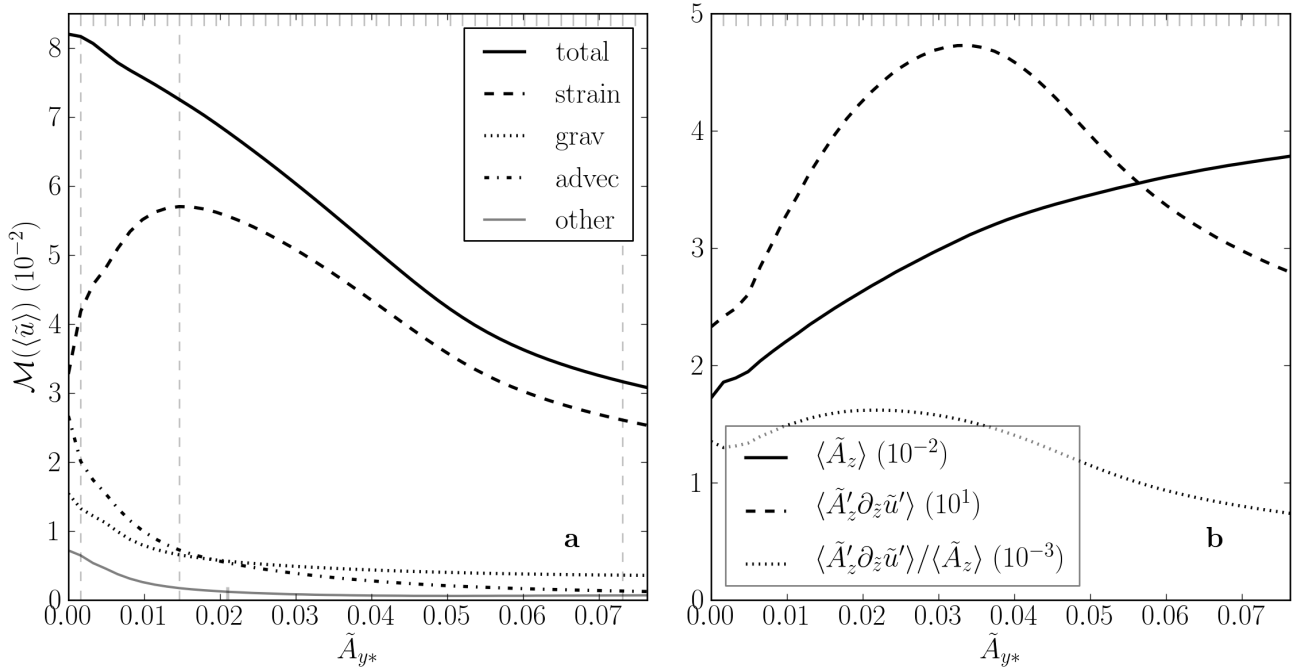


Figure 4.1: **a** Measure of the intensity of the residual longitudinal circulation contributions for varying non-dimensional quasi-lateral diffusivity ($\alpha = 0.004$, other parameters as in Tab. 2.1). The short bars at the upper abscissa mark the \tilde{A}_{y*} values of the individual simulations and the short bar at the lower abscissa marks the reference value ($\tilde{A}_{y*} = 0.021$). The three vertical lines mark the simulations shown in the following figures.

b Thalweg average of non-dimensional viscosity-shear covariance, residual eddy viscosity and their ratio.

The results are shown in Fig. 4.1a. The intensity of the gravitational circulation and the

intensity of the advectively driven circulation decrease with increasing quasi-lateral diffusivity. The intensity of the tidal straining circulation has a maximum at $\tilde{A}_{y*} \approx 0.015$ ($A_{y*} = 1.8 \text{ m}^2 \text{ s}^{-1}$). To explain this behaviour, residual profiles and tidal cycles of eddy viscosity and salinity are of particular interest (Fig. 4.2e1-f3, 4.3c1-d3).

The decrease of the intensity of the gravitational circulation can only be related to changes of the residual eddy viscosity, $\langle A_z \rangle$ (2.23) (also see section 3.2.4). This increases with increasing \tilde{A}_{y*} (Fig. 4.1b, 4.2e1-e3) due to decreasing stratification (Fig. 4.2f1-f3, explained below).

The decrease of the intensity of the advectively driven circulation is also related to the increase of $\langle A_z \rangle$, but furthermore to the decrease of lateral gradients of the longitudinal and lateral velocities, $\partial_y \langle uv \rangle$ (2.24), associated with the increasing quasi-lateral diffusivity of momentum (not shown; cp. (2.1), (2.2)). This explains why the intensity of the advectively driven circulation decreases faster than the intensity of the gravitational circulation (Fig. 4.1a).

For the intensity of the tidal straining circulation, there is also a second contribution: The viscosity-shear covariance has a maximum at $\tilde{A}_{y*} \approx 0.033$ (thalweg average, Fig. 4.1b, explained below). For $\tilde{A}_{y*} \gtrsim 0.015$, the negative effect ($\langle A_z \rangle$ increasing with \tilde{A}_{y*}) dominates; for $\tilde{A}_{y*} \lesssim 0.015$, the positive effect ($\langle A'_z \partial_z u' \rangle$ increasing with \tilde{A}_{y*}) dominates (cross-sectional average, Fig. 4.1a).

Why does the residual eddy viscosity increase with increasing quasi-lateral diffusivity, i.e. why does the stratification decrease? As shown in section 2.4.2.2, lateral straining, $\partial_z v \partial_y S$, is the dominant contribution to vertical stratification (2SIPS). Thus, the decrease of the lateral salinity gradients, $\partial_y S$, associated with the increasing quasi-lateral diffusivity of salinity (cp. (2.3)), directly leads to a decrease of the vertical salinity gradients. Additionally, decreased lateral salinity gradients generate weaker transverse circulation, v (which is also affected by the increased quasi-lateral diffusivity of momentum), so that the maximum possible stratification is not reached (Fig. 4.4e3 vs. e2). (This is similar to a channel whose aspect ratio is too small for optimum stratification at slack after flood (wide channel, section 2.4.2.1).)

Why does the viscosity-shear covariance has a maximum for a certain quasi-lateral diffusivity? For very low \tilde{A}_{y*} , the stratification is very strong (see above) during both ebb and flood. It is induced by lateral straining already before slack after flood (Fig. 4.4e1), persists throughout the ebb phase and till after full flood, at the surface (Fig. 4.3d1). This leads to low residual eddy viscosity (Fig. 4.2e1), low viscosity fluctuations (Fig. 4.3c1) and strong shear and shear fluctuations (b1). (It should be noted that the simulation with zero quasi-lateral diffusivity gives “spiky” fields of velocity and salinity etc., i.e. with steep and reversing gradients in the lateral direction.) When \tilde{A}_{y*} is slightly increased, the stratification is slightly weaker and does not persist as long. Thus, the main change can be observed in the second half of the flood phase when the thalweg becomes unstably stratified (Fig. 4.3e2); the eddy viscosity increases and the shear decreases (b2,c2 vs. b1,c1). The positive effect on the eddy viscosity fluctuations appears to dominate, compared to the negative effect on the shear fluctuations. As soon as the entire second half of the flood phase is unstably stratified, neither the eddy viscosity nor the shear in this phase are significantly affected when \tilde{A}_{y*} is further increased. Thus, beyond that point, the main change can be observed in the ebb phase when stratification becomes very weak shortly after full ebb (Fig. 4.3d3); the eddy viscosity increases and the shear decreases (b3,c3 vs. b2,c2). This has a negative effect on both the eddy viscosity fluctuations and the shear fluctuations. Therefore, the viscosity-shear covariance and the intensity of the tidal straining circulation have a maximum for a low to medium quasi-lateral diffusivity.

The decrease of the intensity of the tidal straining circulation for very low \tilde{A}_{y*} is compensated by the increase of the intensity of the gravitational and the advectively driven circulation so that

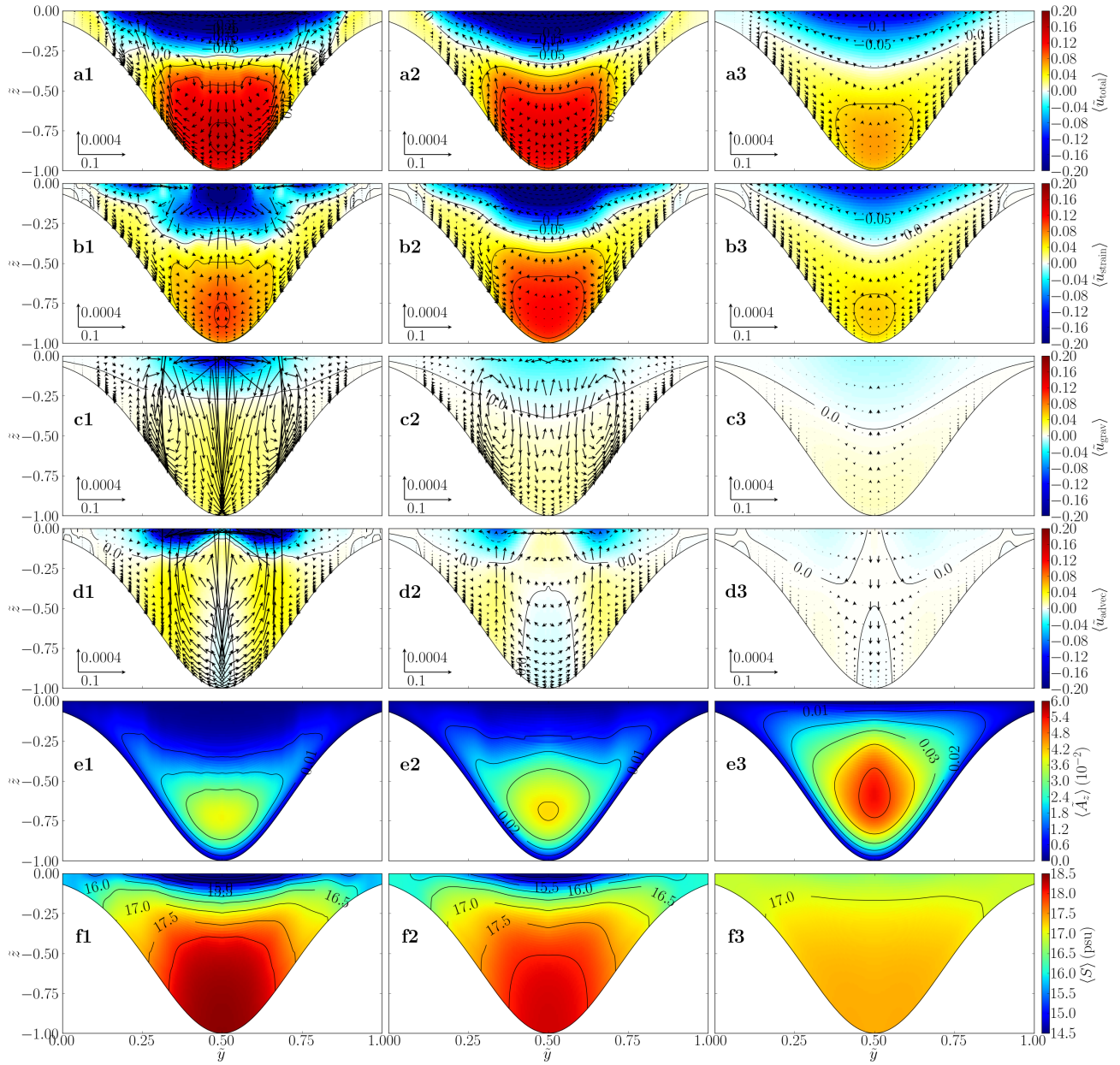


Figure 4.2.: From left to right: **1** $\tilde{A}_{y*} = 0.16 \cdot 10^{-2}$, **2** $1.46 \cdot 10^{-2}$ and **3** $7.31 \cdot 10^{-2}$ (vertical lines in Fig. 4.1a); from top to bottom: residual profile of non-dimensional **a** estuarine circulation, **b** tidal straining circulation, **c** gravitational circulation, **d** advectively driven circulation, **e** eddy viscosity and **f** dimensional salinity.

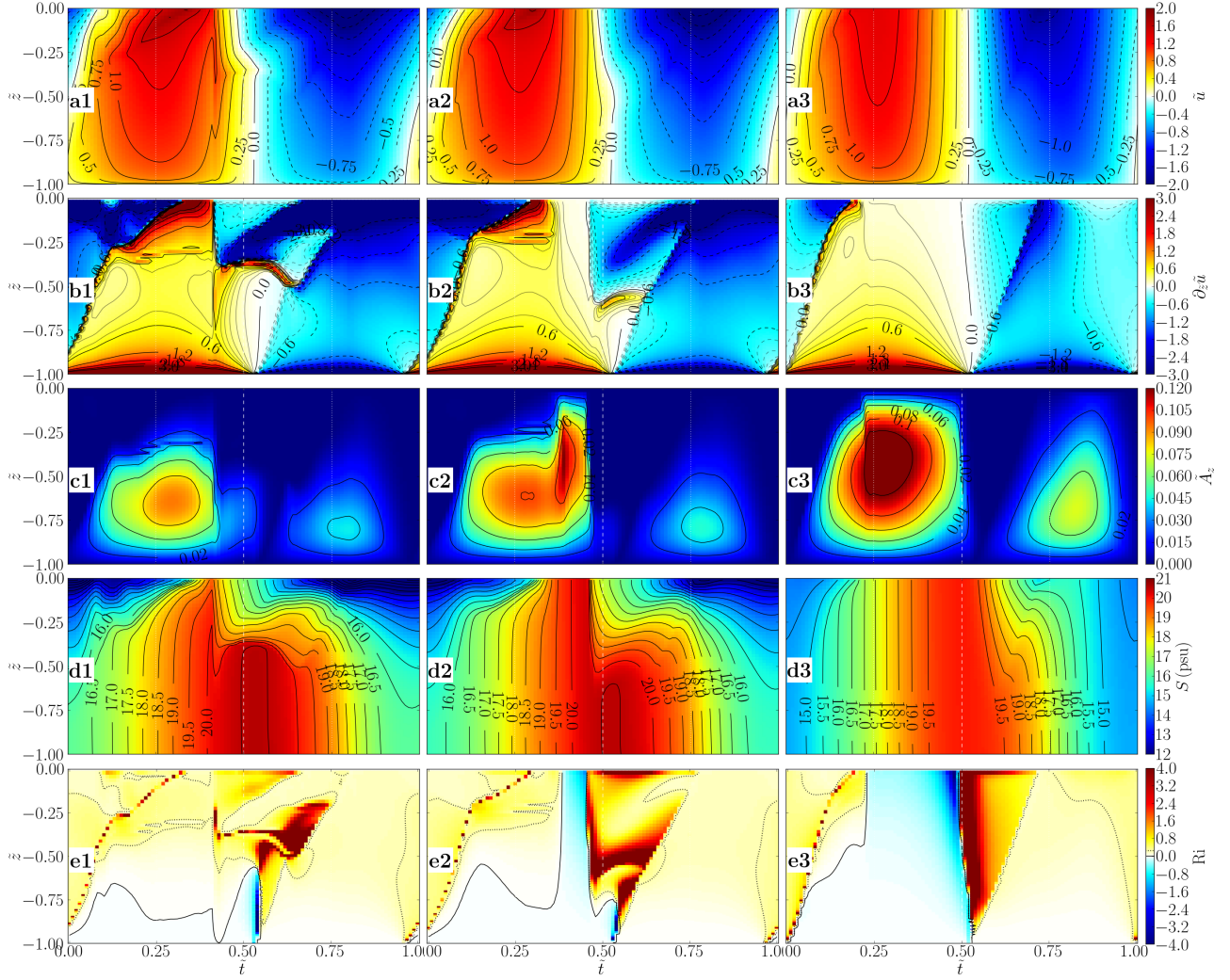


Figure 4.3.: From left to right: **1** $\tilde{A}_{y*} = 0.49 \cdot 10^{-2}$, **2** $1.46 \cdot 10^{-2}$ and **3** $4.39 \cdot 10^{-2}$ (vertical lines in Fig. 4.1a); from top to bottom: tidal cycle at thalweg of non-dimensional **a** longitudinal velocity, **b** vertical shear of longitudinal velocity, **c** eddy viscosity, **d** dimensional salinity and **e** gradient Richardson number, $Ri = N^2/S^2$.

the total, estuarine circulation decreases with increasing \tilde{A}_{y*} over the entire range (Fig. 4.1a). For very high \tilde{A}_{y*} , lateral gradients of the longitudinal velocity and the salinity are very weak. This is comparable to a very wide channel and also resembles a one-dimensional situation (section 2.4.1).

4.3. Impact of the minimum-to-maximum depth ratio

Three non-dimensional numbers describe the channel shape and determine the slope steepness: λ (2.12), \tilde{H}_{\min} (2.13) and α (2.14) (see sections 2.2.2, 2.2.3). Here, the focus is on \tilde{H}_{\min} .

$\tilde{H}_{\min} = H_{\min}/H_{\max}$ (2.13) is the ratio of the minimum water depth (at the shores) to the maximum water depth (at the thalweg, Fig. 2.1b). The half-cross-sectionally averaged channel

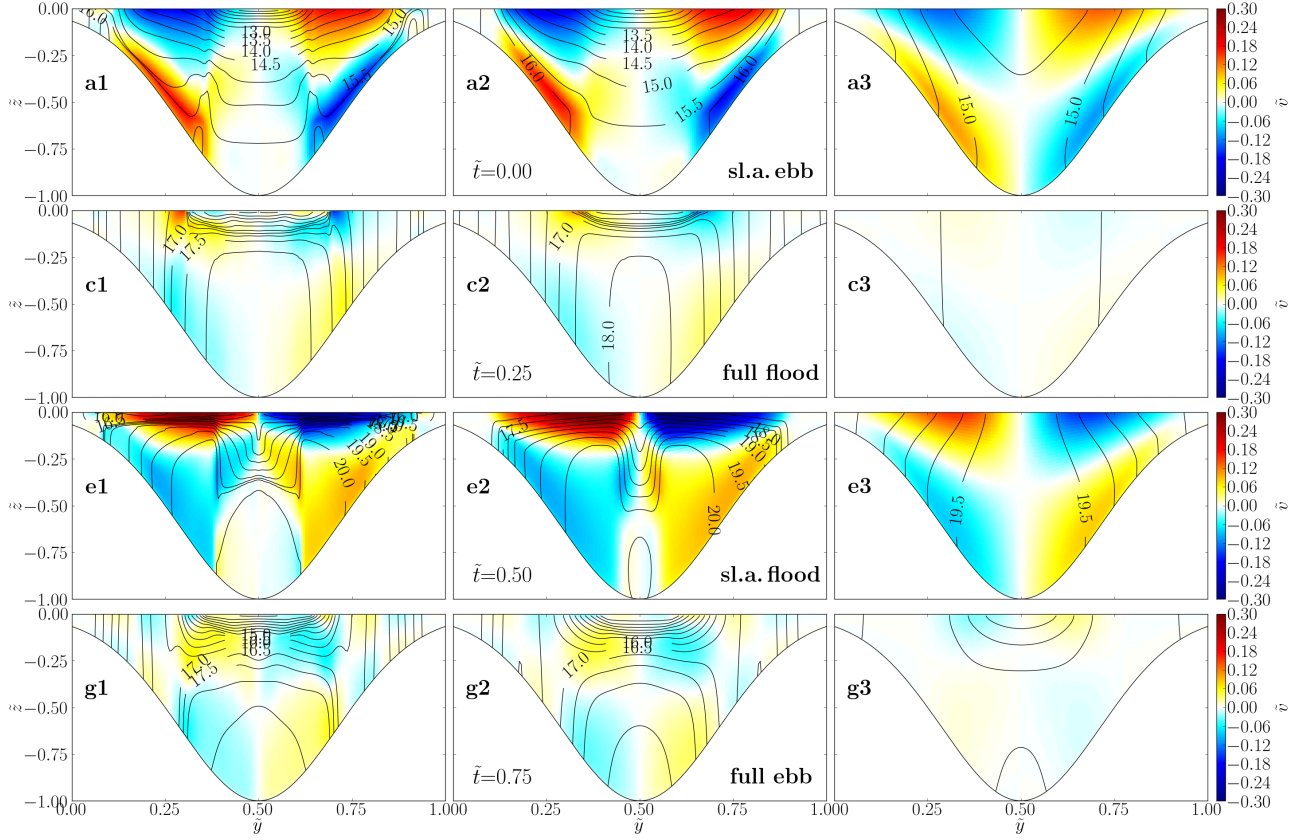


Figure 4.4.: From left to right: **1** $\tilde{A}_{y*} = 0.49 \cdot 10^{-2}$, **2** $1.46 \cdot 10^{-2}$ and **3** $4.39 \cdot 10^{-2}$ (vertical lines in Fig. 4.1a); from top to bottom: non-dimensional lateral velocity (colour) and dimensional salinity (contours, interval 0.5 psu) at **a** $\tilde{t} = 0.00$ (slack after ebb), **c** 0.25 (full flood), **e** 0.50 (slack after flood) and **g** 0.75 (full ebb) (labels **b** etc. omitted to avoid confusion with Fig. 2.5).

slope,

$$s := \overline{\partial_y H} = \frac{H_{\max} - H_{\min}}{W/2} = 2\alpha \left(1 - \tilde{H}_{\min}\right), \quad (4.3)$$

is proportional to α as well as to $(1 - \tilde{H}_{\min})$. The impact of α on the intensity of the tidal straining circulation is mainly based on the impact of the channel slope on the laterally differential longitudinal advection and thus on the strength of the transverse circulation (sections 2.4.2.1, 3.1). Thus, one can hypothesise that the effect of varying $(1 - \tilde{H}_{\min})$ is the same as the effect of varying α .

\tilde{H}_{\min} is varied by means of H_{\min} so that no other non-dimensional number is affected (cp. Tab. 2.1). It is limited to $0 < \tilde{H}_{\min} < 0.5$ ($0 < H_{\min} < H_{\max}/2$ (2.9)). (Otherwise there is no FWHM $\neq W$.) The results of 120 simulations covering the two-dimensional parameter space spanned by α and \tilde{H}_{\min} are shown in Fig. 4.5.

The channel slope increases from the upper left to the lower right corner of the depicted parameter space ((4.3), contours in Fig. 4.5b). The gravitational circulation is hardly affected (**c**); the advectively driven circulation increases with the slope (**d**; also see Fig. 2.2 and associated descriptions). The tidal straining circulation is maximum for medium channel slopes, s_m , but the value depends on the aspect ratio and the minimum depth in such a way that it increases with α and with

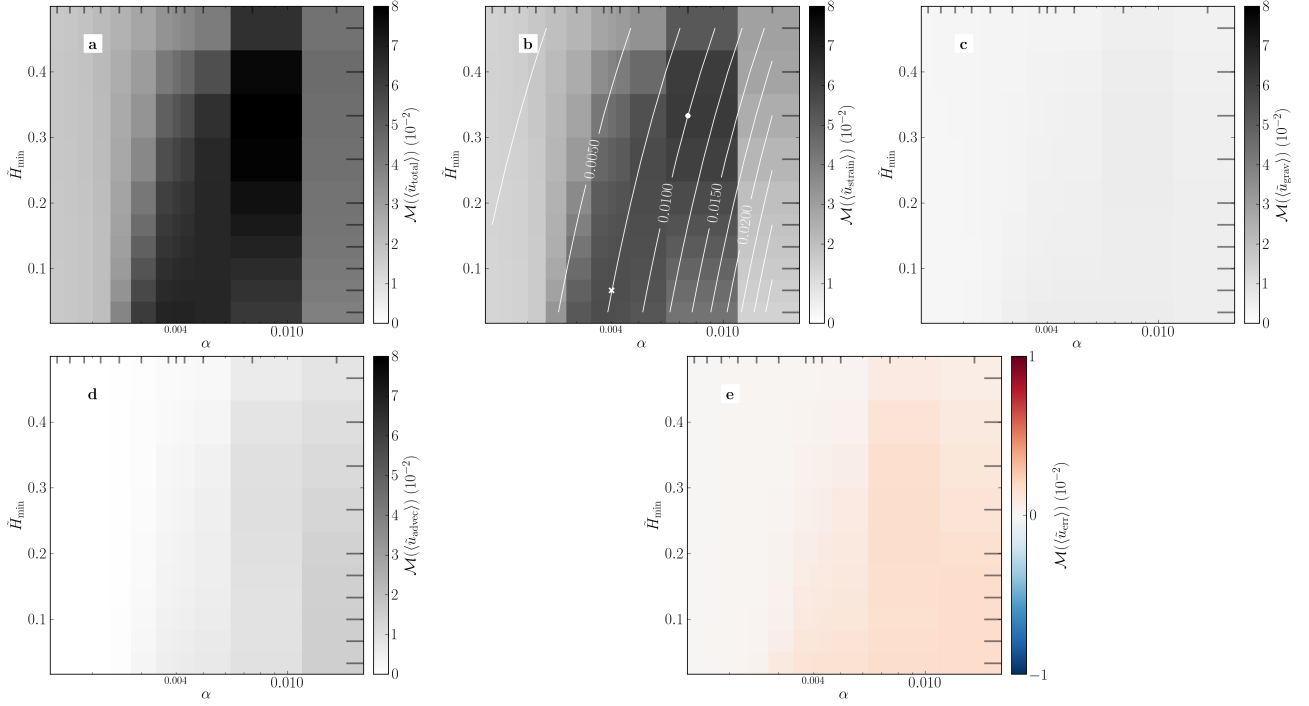


Figure 4.5.: Measure of the intensity of the residual longitudinal circulation contributions in the 2D parameter space spanned by the aspect ratio and the minimum-to-maximum water depth ratio (other parameters as in Tab. 2.1). **a** Total, **b** tidal straining, **c** gravitational, **d** advectively driven and **e** error circulation.

The contours in **b** are isolines of the average channel slope (4.3); the white cross marks the maximum tidal straining circulation for $\tilde{H}_{\min} = 0.067$ (Fig. 2.2) and the white dot marks the maximum for a larger \tilde{H}_{\min} . The short bars at the upper abscissa and at the right ordinate mark the α and \tilde{H}_{\min} values of the individual simulations.

\tilde{H}_{\min} . For example, $s_m = 0.0075$ for $\tilde{H}_{\min} = 0.067$ ($\alpha = 0.0040$, white cross in Fig. 4.5b) and $s_m = 0.0100$ for $\tilde{H}_{\min} = 0.333$ ($\alpha = 0.0075$, white dot). This can be explained as follows:

Not only the channel slope influences the laterally differential longitudinal advection and thus the strength of the transverse circulation, but also the depth itself affects the velocities via bottom friction. It should be noted that the bottom roughness length, z_0^b , is not varied. (Scaling z_0^b with the now varied mean water depth instead of the invariant maximum water depth (Tab. 2.1) might have been a better choice for proving the hypothesis, above. Also see the final discussion in section 4.4.) When \tilde{H}_{\min} increases, the velocities at the thalweg are not (directly) changed, but the (depth-averaged) velocities at the shoals are increased due to the reduced influence of bottom friction in the upper layer. Thus, the decrease of the lateral gradient of the longitudinal velocity, $\partial_y u$, due to increasing \tilde{H}_{\min} is larger than the increase of $\partial_y u$ due to increasing α so that the slope remains invariant,

$$|\partial_y u| \downarrow_{\tilde{H}_{\min} \uparrow} < |\partial_y u| \uparrow_{\alpha \uparrow, s \rightarrow}.$$

In order to compensate this imbalance and to reach maximum (over α) intensity of the tidal straining circulation for a larger \tilde{H}_{\min} , α needs to increase more than just as much as required for invariant s . Therefore s_m increases with \tilde{H}_{\min} and α .

4.4. Impact of the full width at half maximum depth

$\lambda = 1 - \text{FWHM}/W$ (2.12) is that fraction of the channel width where the water depth is shallower than half the maximum depth, $H(y) \leq H_{\max}/2$ (cp. Fig. 2.1b). A larger λ means wider shoals and steeper maximum slopes in the centre of the channel. Vice versa, a smaller λ means no shoals but steepest slopes close to the shores and gentler slopes toward the thalweg. (Note that the half-cross-sectionally averaged channel slope (4.3) does not change with λ .)

Let us consider the case of a larger λ . The steeper maximum slopes mean larger lateral gradients of longitudinal velocity and thus salinity, but these gradients are confined to the centre of the channel. The lateral gradients above the flat shoals are small and not related to the local slope ($\partial_y H \approx 0$) but to lateral mixing with the channel centre (at the edge of each shoal). Consequently, the lateral velocities are higher in the centre of the channel and lower above the shoals, compared to a smaller λ . Please note that velocities, and thus also the longitudinal circulation intensities, are very low above the shallow shoals due to bottom friction (see section 4.3).

If the shoals are ignored in the calculation of the circulation contributions, one may expect that a channel with a larger λ yields circulation intensities similar to those of a channel with a larger α (no shoals to ignore). If the shoals are not ignored in the calculation, the weak circulation above the shoals drastically reduces the cross-section-wide measure of the circulation intensities (2.25). Note that, in (2.25), the watercolumn-wise measure,

$$\mathcal{M}_z(\langle \tilde{u}_i \rangle)(y) = -\frac{4}{H^2(y)} \int_{-H(y)}^0 \langle \tilde{u}_i \rangle(y, z) \left\{ z + \frac{H(y)}{2} \right\} dz, \quad (4.4)$$

is not weighted with the water depth when laterally averaged,

$$\mathcal{M}(\langle \tilde{u}_i \rangle) = \frac{1}{W} \int_0^W \mathcal{M}_z(y) dy. \quad (4.5)$$

I therefore suggest an alternative measure taking the relative water depth into account:

$$\begin{aligned} \mathcal{M}_H(\langle \tilde{u}_i \rangle) &= \frac{1}{W} \int_0^W \frac{H(y)}{H_{\text{mean}}} \mathcal{M}_z(y) dy \\ &= -\frac{1}{A} \int_0^W \frac{4}{H(y)} \int_{-H(y)}^0 \langle \tilde{u}_i \rangle(y, z) \left\{ z + \frac{H(y)}{2} \right\} dz dy \end{aligned} \quad (4.6)$$

with the mean water depth $H_{\text{mean}} = \frac{1}{W} \int_0^W H(y) dy$ (A.14) and the cross-sectional area $A = \int_0^W H(y) dy$ (A.11) (see appendix A.2.2). The depth-weighted measure, \mathcal{M}_H (4.6), has the same properties as the original (2.25) (Burchard et al. 2011).

Unfortunately, this was a last-minute idea and is not yet implemented so that all results are based on the original measure (2.25). The results of about 80 simulations covering the two-dimensional parameter space spanned by α and λ are shown in Fig. 4.6. The intensity of all circulation contributions decreases with increasing λ as expected with the unweighted measure.

Another issue with these simulations is that varying λ implies varying H_{mean} and W_{mean} so that the non-dimensionalisation with H_{\max} and $W = W_{\max}$ (Tab. 2.1) might be problematic, particularly in view of the impact of the quasi-lateral diffusivities (section 4.2). Tab. 4.1 lists the circulation intensities for three different λ and two different non-dimensionalisations.

4.4. Impact of the full width at half maximum depth

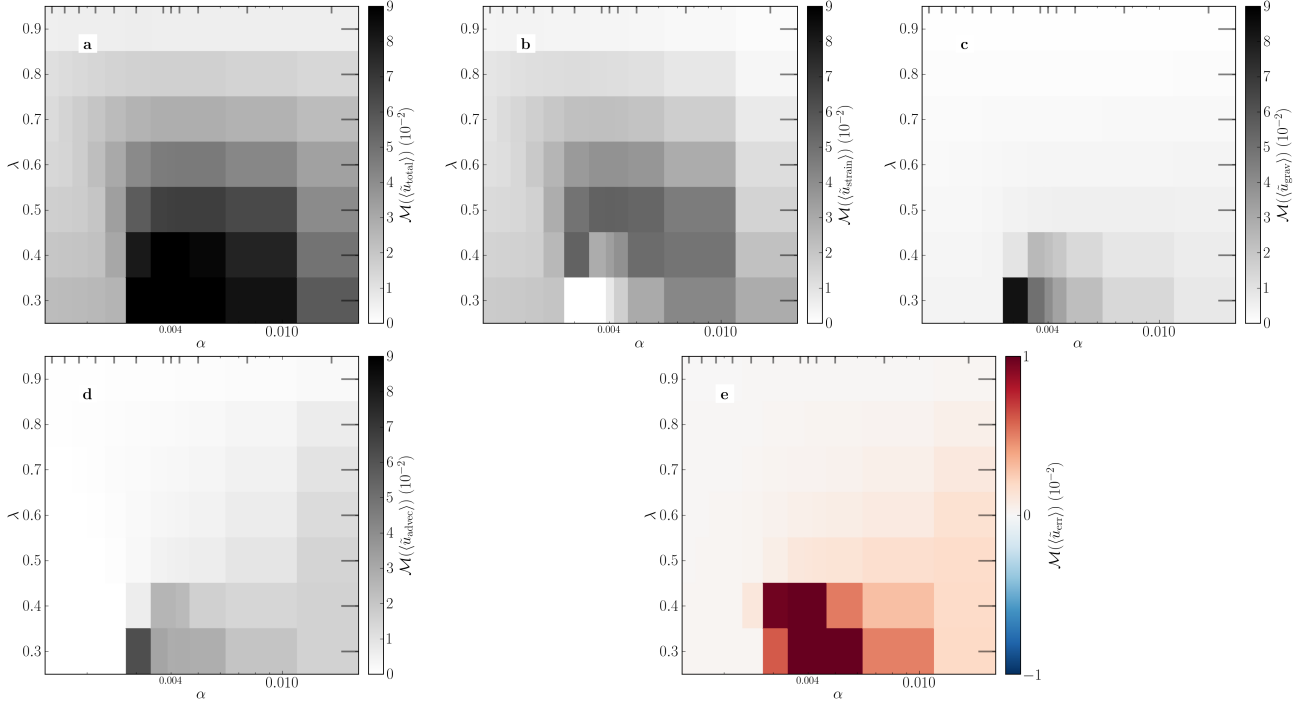


Figure 4.6.: Measure of the intensity of the residual longitudinal circulation contributions in the 2D parameter space spanned by the aspect ratio and $\lambda = 1 - \text{FWHM}/W$ (2.12) (other parameters as in Tab. 2.1). **a** Total, **b** tidal straining, **c** gravitational, **d** advectively driven and **e** error circulation. The short bars at the upper abscissa and at the right ordinate mark the α and λ values of the individual simulations.

For $\lambda = 0.7$, H_{mean} and W_{mean} are smaller than for $\lambda = 0.5$ (ratio $r = 0.668$). For invariant non-dimensional numbers based on the mean water depth and channel width, z_0^b and U_t have to be multiplied with r and A_{y*} with r^2 , i.e. these parameters are smaller than for $\lambda = 0.5$. For $\lambda = 0.3$, the opposite is the case ($r = 1.273$).

These changes of bottom friction, velocities and quasi-lateral diffusion affect the entire dynamics. The trend of the intensity of the total, the gravitational and the advectively driven circulation even reverses, compared to non-dimensionalisation based on the maximum depth and width. (Note again that the unweighted measure (2.25) is used here.) Therefore, the choice of the scaling should be given more thought (also see section 6.2).

λ	total		strain.		grav.		advec.		run-off		error	
0.7	1.703	4.297	0.720	-0.012	0.138	1.166	0.622	2.564	0.167	0.130	0.056	0.483
0.5	3.104	3.104	1.664	1.664	0.265	0.265	0.893	0.893	0.195	0.195	0.087	0.087
0.3	3.814	2.477	1.899	1.489	0.410	0.193	1.179	0.599	0.206	0.145	0.122	0.051

Table 4.1.: Measure of the intensity of the estuarine circulation contributions for different λ and non-dimensionalisations. For the white columns, the non-dimensional numbers are based on $H = H_{\text{max}}$ and $W = W_{\text{max}}$ (i.e. same model input for all λ , Tab. 2.1*); for the grey columns, they are based on $H = H_{\text{mean}}$ and $W = W_{\text{mean}}$ (i.e. varied z_0^b , U_t , A_{y*} ; fixed at reference value $\lambda = 0.5$).

*It should be noted that $W = 1000 \text{ m}$ and $\partial_x S = -2 \cdot 10^{-4} \text{ psu m}^{-1}$ here.

Chapter 5

Decomposition of the estuarine circulation for free surface elevation

The two-dimensional model presented and used in the previous chapters has a constant surface elevation, $\eta(y, t) = 0$ (rigid lid, see section 2.2.1). This simplification is not problematic for the investigations made in this study (cp. section 2.4.4). Its advantage is a straightforward tidal averaging and decomposition of the total residual circulation in z coordinates (section 2.3.3).

For more realistic applications, the rigid-lid assumption would be an oversimplification. Therefore, an advanced mathematical framework is developed which allows for tidal averaging and circulation decomposition in σ coordinates. The method is applied to three-dimensional simulations.

5.1. Mathematical framework

For the sake of shortness, the lateral dimension is ignored in the derivation of the equations. The missing terms are added at the end (section 5.1.4).

5.1.1. Dynamic equations and boundary conditions in σ coordinates

The two-dimensional longitudinal-vertical dynamic equation for the horizontal velocity component u is formulated in σ coordinates as

$$\begin{aligned} & \partial_t (Du) + \partial_x (Du^2) + \partial_\sigma (Du\omega) - \partial_x (A_x \partial_x (Du)) - \partial_\sigma \left(\frac{A_z}{D} \partial_\sigma u \right) \\ &= \int_\sigma^0 D^2 \partial_x^* b \, d\sigma' - gD \partial_x \eta, \end{aligned} \quad (5.1)$$

see Burchard and Petersen (1997), with $\sigma = (z - \eta)/D$, the depth $D(x) = H(x) + \eta(x, t)$, the bottom coordinate $-H(x)$ and the time-dependent free surface elevation $\eta(x, t)$. The temporally and spatially variable vertical eddy viscosity is denoted by $A_z (= A_\sigma)$ and the constant in time and space quasi-horizontal eddy viscosity is denoted by A_x .

The incompressibility condition is formulated as

$$\partial_t (D) + \partial_x (Du) + \partial_\sigma (D\omega) = 0. \quad (5.2)$$

In (5.1) and (5.2),

$$\omega = \partial_t^* \sigma + u \partial_x^* \sigma + \frac{w}{D} \quad (5.3)$$

is the grid-related vertical velocity, with w denoting the vertical velocity component with respect to z coordinates. ∂ denotes derivatives with respect to constant σ coordinates and ∂^* denotes derivatives with respect to constant geopotential z coordinates.

For the kinematic boundary conditions, the grid-related vertical velocity vanishes at the surface and the bottom,

$$\begin{aligned} \omega &= 0 \quad \text{for } \sigma = 0, \\ \omega &= 0 \quad \text{for } \sigma = -1. \end{aligned} \quad (5.4)$$

As dynamic boundary conditions, a flux condition at the surface and the no-slip condition at the bottom are used,

$$\begin{aligned} \frac{A_z}{D} \partial_\sigma u &= \frac{\tau^s}{\rho_0} \quad \text{for } \sigma = 0, \\ u &= 0 \quad \text{for } \sigma = -1, \end{aligned} \quad (5.5)$$

with the surface stress, τ^s .

5.1.2. Eulerian residual velocity

To obtain a tidal averaging operator, we first define the Eulerian transport as

$$M(x, t) = D(x, t) \int_{-1}^0 u(x, \sigma, t) d\sigma,$$

following Zimmerman (1979). In accordance with Longuet-Higgins (1969), we define the Eulerian transport between the bottom and a certain σ layer as

$$M_\sigma(x, t) = D(x, t) \int_{-1}^\sigma u(x, \sigma', t) d\sigma'.$$

The Eulerian transport velocity, U , and the Eulerian transport velocity between the bottom and a certain σ layer, U_σ , can then be defined as

$$U(x, t) = \frac{M(x, t)}{D(x, t)} \quad \text{and} \quad U_\sigma(x, t) = \frac{M_\sigma(x, t)}{(1 + \sigma)D(x, t)},$$

which is in accordance with the respective definitions by Longuet-Higgins (1969) and Zimmerman (1979). The Eulerian residual transport, \bar{M} , and the Eulerian residual transport between the bottom and a certain σ layer, \bar{M}_σ , can then be defined as

$$\bar{M}(x, t) = \langle M(x, t) \rangle \quad \text{and} \quad \bar{M}_\sigma(x, t) = \langle M_\sigma(x, t) \rangle,$$

with the temporal averaging operator $\langle \cdot \rangle$ defined as

$$\langle X(x, \sigma, t) \rangle = \frac{1}{T} \int_{t-T/2}^{t+T/2} X(x, \sigma, \tau) d\tau \quad \text{or} \quad \langle Y(x, t) \rangle = \frac{1}{T} \int_{t-T/2}^{t+T/2} Y(x, \tau) d\tau \quad (5.6)$$

for any two-dimensional variable X or one-dimensional variable Y , with the tidal period T .

Next, we define the Eulerian residual transport velocity, \bar{U} , and the Eulerian residual transport velocity between the bottom and a certain σ layer, \bar{U}_σ ,

$$\bar{U}(x, t) = \frac{\bar{M}(x, t)}{\langle D(x, t) \rangle} \quad \text{and} \quad \bar{U}_\sigma(x, t) = \frac{\bar{M}_\sigma(x, t)}{(1 + \sigma) \langle D(x, t) \rangle}.$$

It should be noted that the definition for \bar{U} is identical to the definition given by Zimmerman (1979, his equation (6)).

In extension to the definition of the Eulerian transport between the bottom and a certain σ layer, M_σ , we define now the the Eulerian transport within a $\Delta\sigma$ band around a certain σ layer, $M_{\sigma, \Delta\sigma}$, as

$$M_{\sigma, \Delta\sigma} = M_{\sigma+\Delta\sigma/2} - M_{\sigma-\Delta\sigma/2}.$$

In analogy, we also define the Eulerian residual transport within a $\Delta\sigma$ band around a certain σ layer $\bar{M}_{\sigma, \Delta\sigma}$, as

$$\bar{M}_{\sigma, \Delta\sigma} = \bar{M}_{\sigma+\Delta\sigma/2} - \bar{M}_{\sigma-\Delta\sigma/2}.$$

The according Eulerian transport velocity and Eulerian residual transport velocity within a $\Delta\sigma$ band around a certain σ layer are then given by

$$U_{\sigma, \Delta\sigma} = \frac{M_{\sigma, \Delta\sigma}}{\Delta\sigma D} \quad \text{and} \quad \bar{U}_{\sigma, \Delta\sigma} = \frac{\bar{M}_{\sigma, \Delta\sigma}}{\Delta\sigma \langle D \rangle}.$$

For the limit of $\Delta\sigma \rightarrow 0$, $U_{\sigma, \Delta\sigma}$ converges to the local velocity value $u(x, \sigma, t)$. In the same way, $\bar{U}_{\sigma, \Delta\sigma}$ converges to a local velocity value which we here define as the Eulerian residual velocity profile:

$$\bar{u}(x, \sigma, t) = \frac{\langle D(x, t) u(x, \sigma, t) \rangle}{\langle D(x, t) \rangle}, \quad (5.7)$$

which is an approximation of the Eulerian residual transport velocity in an infinitesimal layer around a certain σ level.

We further define for any variable the fluctuating deviation from the tidal mean,

$$X' = X - \langle X \rangle, \quad Y' = Y - \langle Y \rangle.$$

For clarity, arguments will be dropped from here onwards.

With this, the tidal mean transport velocity, u_m , can be calculated as

$$u_m = \int_{-1}^0 \bar{u} d\sigma. \quad (5.8)$$

For periodic conditions, u_m is equal to the tidally averaged run-off velocity $\langle u_r \rangle$.

In the following, it will be shown how the tidal mean velocity profile \bar{u} can be dynamically decomposed into contributions from the terms in the momentum equation (5.1).

5.1.3. Decomposition of the total residual longitudinal circulation

To resolve the momentum budget for \bar{u} , (5.1) is first vertically integrated from a position σ in the water column up to the surface such that after application of the surface boundary conditions (5.4) and (5.5) and rearrangement of terms the following expression is obtained:

$$\begin{aligned} \frac{A_z}{D} \partial_\sigma u = & -\partial_t \int_\sigma^0 Du d\sigma' - \partial_x \int_\sigma^0 Du^2 d\sigma' + Du\omega \\ & + \partial_x \int_\sigma^0 A_x \partial_x (Du) d\sigma' + \int_\sigma^0 \int_{\sigma'}^0 D^2 \partial_x^* b d\sigma'' d\sigma' \\ & + g\sigma D \partial_x \eta + \frac{\tau^s}{\rho_0}. \end{aligned}$$

In the next step, temporal averaging according to (5.6) is carried out:

$$\begin{aligned} \langle A_z/D^2 \rangle \partial_\sigma \langle Du \rangle = & -\Delta(Du) - \partial_x \int_\sigma^0 \langle Du^2 \rangle d\sigma' + \langle Du\omega \rangle \\ & + \partial_x \int_\sigma^0 A_x \partial_x \langle Du \rangle d\sigma' + \int_\sigma^0 \int_{\sigma'}^0 \langle D^2 \partial_x^* b \rangle d\sigma'' d\sigma' \\ & + g\sigma \langle D \partial_x \eta \rangle + \frac{\langle \tau^s \rangle}{\rho_0} - \left\langle (A_z/D^2)' \partial_\sigma (Du)' \right\rangle, \end{aligned}$$

with the remaining non-stationarity term

$$\Delta(Du) = \frac{1}{T} \int_\sigma^0 \left((Du)_{t+T/2} - (Du)_{t-T/2} \right) d\sigma'$$

and the decomposition

$$\left\langle \frac{A_z}{D} \partial_\sigma u \right\rangle = \left\langle \frac{A_z}{D^2} \partial_\sigma (Du) \right\rangle = \langle A_z/D^2 \rangle \partial_\sigma \langle Du \rangle + \left\langle (A_z/D^2)' \partial_\sigma (Du)' \right\rangle.$$

In a third step, division by $\langle A_z/D^2 \rangle$, subsequent vertical integration from the bottom to a position σ in the water column and division by $\langle D \rangle$ is carried out, using the dynamic bottom

boundary condition (5.5). This yields

$$\bar{u} = \frac{\langle Du \rangle}{\langle D \rangle} = \sum_{i=0}^5 \int_{-1}^{\sigma} \mathcal{A}_i d\sigma' + g \frac{\langle D \partial_x \eta \rangle}{\langle D \rangle} \int_{-1}^{\sigma} \frac{\sigma'}{\langle A_z/D^2 \rangle} d\sigma' \quad (5.9)$$

with

$$\begin{aligned} \mathcal{A}_0 &= -\frac{\Delta(Du)}{\langle A_z/D^2 \rangle \langle D \rangle}, \\ \mathcal{A}_1 &= -\frac{\langle (A_z/D^2)' \partial_{\sigma} (Du)' \rangle}{\langle A_z/D^2 \rangle \langle D \rangle}, \\ \mathcal{A}_2 &= \frac{\int_{\sigma}^0 \int_{\sigma'}^0 \langle D^2 \partial_x^* b \rangle d\sigma'' d\sigma'}{\langle A_z/D^2 \rangle \langle D \rangle}, \\ \mathcal{A}_3 &= \frac{\langle \tau^s \rangle / \rho_0}{\langle A_z/D^2 \rangle \langle D \rangle}, \\ \mathcal{A}_4 &= -\frac{\partial_x \int_{\sigma}^0 \langle Du^2 \rangle d\sigma'}{\langle A_z/D^2 \rangle \langle D \rangle} + \frac{\langle Du\omega \rangle}{\langle A_z/D^2 \rangle \langle D \rangle}, \\ \mathcal{A}_5 &= \frac{\partial_x \int_{\sigma}^0 A_x \partial_x \langle Du \rangle d\sigma'}{\langle A_z/D^2 \rangle \langle D \rangle}. \end{aligned} \quad (5.10)$$

Using (5.8) to eliminate the barotropic pressure gradient, (5.9) can be reformulated as

$$\bar{u} = \sum_{i=0}^5 \left\{ \int_{-1}^{\sigma} \mathcal{A}_i d\sigma' - \gamma \int_{-1}^0 \int_{-1}^{\sigma} \mathcal{A}_i d\sigma' d\sigma \right\} + \gamma u_m \quad (5.11)$$

with

$$\gamma = \frac{\int_{-1}^{\sigma} \frac{\sigma'}{\langle A_z/D^2 \rangle} d\sigma'}{\int_{-1}^0 \int_{-1}^{\sigma} \frac{\sigma'}{\langle A_z/D^2 \rangle} d\sigma' d\sigma}.$$

The terms \mathcal{A}_i (5.10) characterise the **0** non-stationary, **1** tidal straining, **2** gravitational, **3** wind-driven, **4** advectively driven and **5** quasi-horizontal mixing circulation (\bar{u}_i); the term γu_m in (5.11) is the local run-off (cp. Burchard et al. 2011).

5.1.4. Lateral terms

Lateral advection, $\partial_y(Duv)$, and lateral diffusion, $-\partial_y(A_y \partial_y(Du))$, are missing in (5.1), but they are treated analogue to longitudinal advection and diffusion in the entire derivation. Thus, they can

simply be re-added at the end. The advective and the diffusive term become

$$\begin{aligned}\mathcal{A}_4 &= -\frac{\partial_x \int_{\sigma}^0 \langle Du^2 \rangle d\sigma'}{\langle A_z/D^2 \rangle \langle D \rangle} - \frac{\partial_y \int_{\sigma}^0 \langle Duv \rangle d\sigma'}{\langle A_z/D^2 \rangle \langle D \rangle} + \frac{\langle Du\omega \rangle}{\langle A_z/D^2 \rangle \langle D \rangle}, \\ \mathcal{A}_5 &= \frac{\partial_x \int_{\sigma}^0 A_x \partial_x \langle Du \rangle d\sigma'}{\langle A_z/D^2 \rangle \langle D \rangle} + \frac{\partial_y \int_{\sigma}^0 A_y \partial_y \langle Du \rangle d\sigma'}{\langle A_z/D^2 \rangle \langle D \rangle}.\end{aligned}\tag{5.12}$$

It should be noted that $A_x = A_y = \text{const.}$ in the model.

5.2. Method:

Three-dimensional simulation, analysis and notation

The model is described in section 2.4.4 (Tab. 2.4). Here, the width and the river discharge are invariant and set to the values leading to maximum estuarine circulation (Fig. 2.13b),

$$W_{\max} = 19 \text{ km}, \quad W_{\min} = 1.9 \text{ km}, \quad Q = 190 \text{ m}^3 \text{ s}^{-1}.$$

The global river discharge, $Q = \int_{-W/2}^{W/2} q(y) dy$, is distributed over the (60) grid cells at the river mouth ($x = 0 \text{ km}$) in such a way that the local discharge, $q(y)$, is proportional to the local water depth, $H(x, y)$. Please note that this distribution required the implementation of a new river discharge weighting scheme into GETM, see appendix B.1.

It should be noted that wind is not included here, i.e. $\bar{u}_3 = \mathcal{A}_3 = 0$.

For the two-dimensional, rigid-lid model (previous chapters), the decomposition of the total residual circulation was implemented into GETM, i.e. calculated online. For the three-dimensional, free-surface model, it is implemented into the post-processing routines, i.e. calculated offline.

The offline calculation has the advantage that it needs do be done only for the cross-sections of interest. Furthermore, in a complex realistic model where a channel of interest does not necessarily align with the coordinate system, the decomposition can be applied to arbitrary cross-sections after rotation and interpolation of the velocities and other required variables.

A disadvantage might arise from the coarse(r) temporal resolution provided by the model output. For example, in the two-dimensional model (section 2.3.1), the output time step is 200 times as large as the computation time step in GETM, and in the three-dimensional model (section 2.4.4), it is 500 times as large.

To get a feeling for the error made due to this problem, I applied the decomposition method ((5.11), (5.10) and (5.12)) to the two-dimensional, rigid-lid model (section 2.3.1, $dt = T/100$) and compared the results with those of the online calculation. The measures of the intensities of all circulation contributions differed only after the fifth decimal place (e.g. 0.01% relative difference between the tidal straining measures) and the cross-sectional views could not be distinguished. I conclude that the coarser resolution is not a problem as long as it is not too coarse. (The numeral meaning of that could be found by further increasing the output time step.)

Non-dimensionalisation and notation The longitudinal velocity, u , and the vertical eddy viscosity, A_z , are non-dimensionalised as before ((2.16) and (2.17)), but here the tidal current amplitude,

U_t , is not a prescribed constant. It is calculated as the mean of the maximum (flood) and the absolute value of the minimum (ebb) cross-sectionally averaged longitudinal velocity at the respective cross-section.

Since the bar denoting the Eulerian residual, \bar{u} ((5.7), (5.11)), somewhat interferes with the tilde denoting the non-dimensional value, \tilde{u} (2.16), triangular brackets are used instead of the bar,

$$\langle u \rangle \equiv \bar{u} \text{ (5.7)}, \quad \text{for the presentation of the residual results.} \quad (5.13)$$

! This must not be confused with the tidal averaging operator (5.6). From here onward, $\langle \tilde{u} \rangle$, $\langle \tilde{A}_z \rangle$, $\langle S \rangle$ etc. denote Eulerian residuals (5.7).

5.3. Results and discussion of the estuarine circulation decomposition

x (km)	total	strain.	grav.	advec.	h.mix.	run-off	non-st.	sum	error	err./tot.
-60	2.311	1.451	0.230	-0.081	0.001	-0.128	0.001	1.474	0.837	0.362
-40	5.327	3.976	0.344	0.191	-0.003	0.599	-0.020	5.087	0.240	0.045

Table 5.1.: Measure of the intensity of the residual longitudinal circulation contributions, $\mathcal{M}(\langle \tilde{u}_i \rangle)$ (10^{-2}), at two different cross-sections.

The results of the decomposition are listed in Tab. 5.1. The error (last two table columns, (4.1)) is large for the cross-section at $x = -60$ km (x_α in Fig. 2.13a) and comparably small at $x = -40$ km. This is at least partly due to the missing convergence term (4.2), which increases with the width (cp. section 2.4.4), i.e. with increasing distance from the river mouth ($x = 0$ km).

Considering that the convergence is weak, another part of the error might be due to the bending of the coordinate system from approximately cartesian at the river mouth to curvilinear at the open boundary (Fig. 2.13a). This non-perpendicularity is ignored here because the deflection appeared to be small.

The amplitude of the cross-sectionally averaged longitudinal velocity is about 1.3 m s^{-1} at $x = -60$ km and 1.1 m s^{-1} at $x = -40$ km, i.e. decreasing in the up-river direction due to frictional damping. The residual cross-sectionally averaged longitudinal salinity gradient is about $\partial_x S = -4 \cdot 10^{-4} \text{ psu m}^{-1}$ at both locations.

Since the error is much smaller at $x = -40$ km, only this cross-section is considered further. The profiles of the estuarine circulation contributions are shown in Fig. 5.1. (The quasi-horizontal mixing circulation, $\langle \tilde{u}_5 \rangle$ resulting from \mathcal{A}_5 in (5.12), is very weak and therefore omitted.)

In agreement with the intensity measures (Tab. 5.1, lower row), the tidal straining circulation (Fig. 5.1b) is the dominant contribution, followed by the local run-off (e) and the gravitational circulation (c). The other contributions do not play a significant role. (The absolute value of the measure of their intensity is larger then that of the error circulation.)

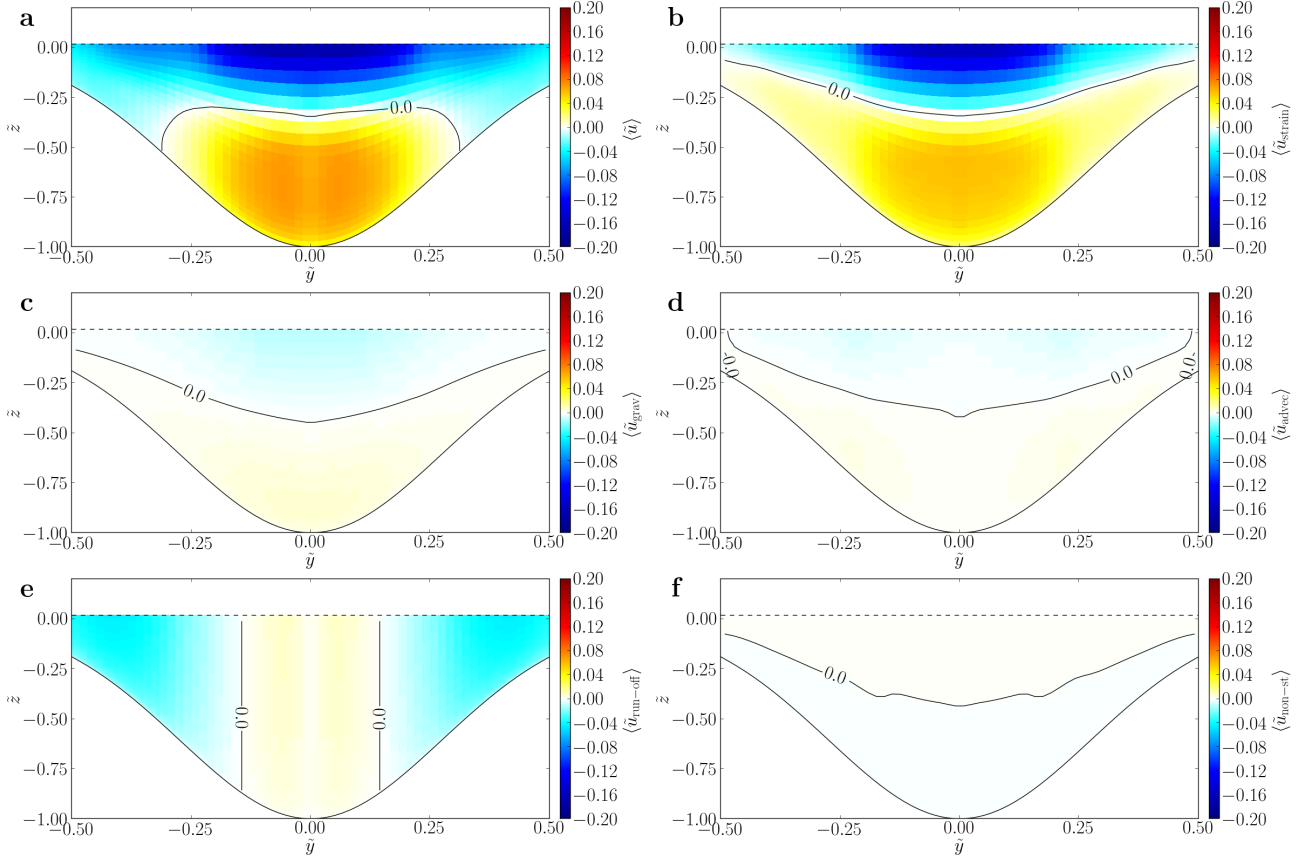


Figure 5.1.: Residual longitudinal circulation contributions at $x = -40$ km. **a** Total, **b** tidal straining, **c** gravitational, **d** advectively driven, **e** local run-off and **f** non-stationary circulation.

5.4. Further results and discussion

For completeness, the residual eddy viscosity and salinity are shown in Fig. 5.2 (e,f). The stratification is weak but stable and the eddy viscosity resembles that in the narrow channel in chapter 2 (Fig. 2.3e3). Note that the circulation profiles (Fig. 5.1a-d) do not resemble those in the narrow channel (Fig. 2.3a3-d3) but more those in a wide to medium channel.

The tidal cycles of salinity and eddy viscosity at the thalweg (Fig. 5.2 c,d) most resemble those in the medium channel (Fig. 2.4c2,d2). The same holds for the tidal cycles of the longitudinal velocity and its vertical shear (Fig. 5.2 a,b vs. Fig. 2.4a2,b2). The stratification and the tidal asymmetries of eddy viscosity and shear are slightly larger there than here.

The ebb dominance (Fig. 5.2 a) is due to the river discharge with a tidally and cross-sectionally averaged velocity of about -0.01 m s^{-1} .

The fast onset of stratification around high water (Fig. 5.2 d), i.e. around slack after flood (a), suggests that the process of secondary strain-induced periodic stratification (2SIPS) is important here, too (cp. section 2.4.2.1). Snapshots of the lateral velocity and salinity are shown in Fig. 5.3. The transverse circulation is surface convergent and very strong before and around slack after flood (h-j) so that a strong stable stratification is induced, which persists at the thalweg till after full ebb (i-n, cp. Fig. 2.5e2-g2).

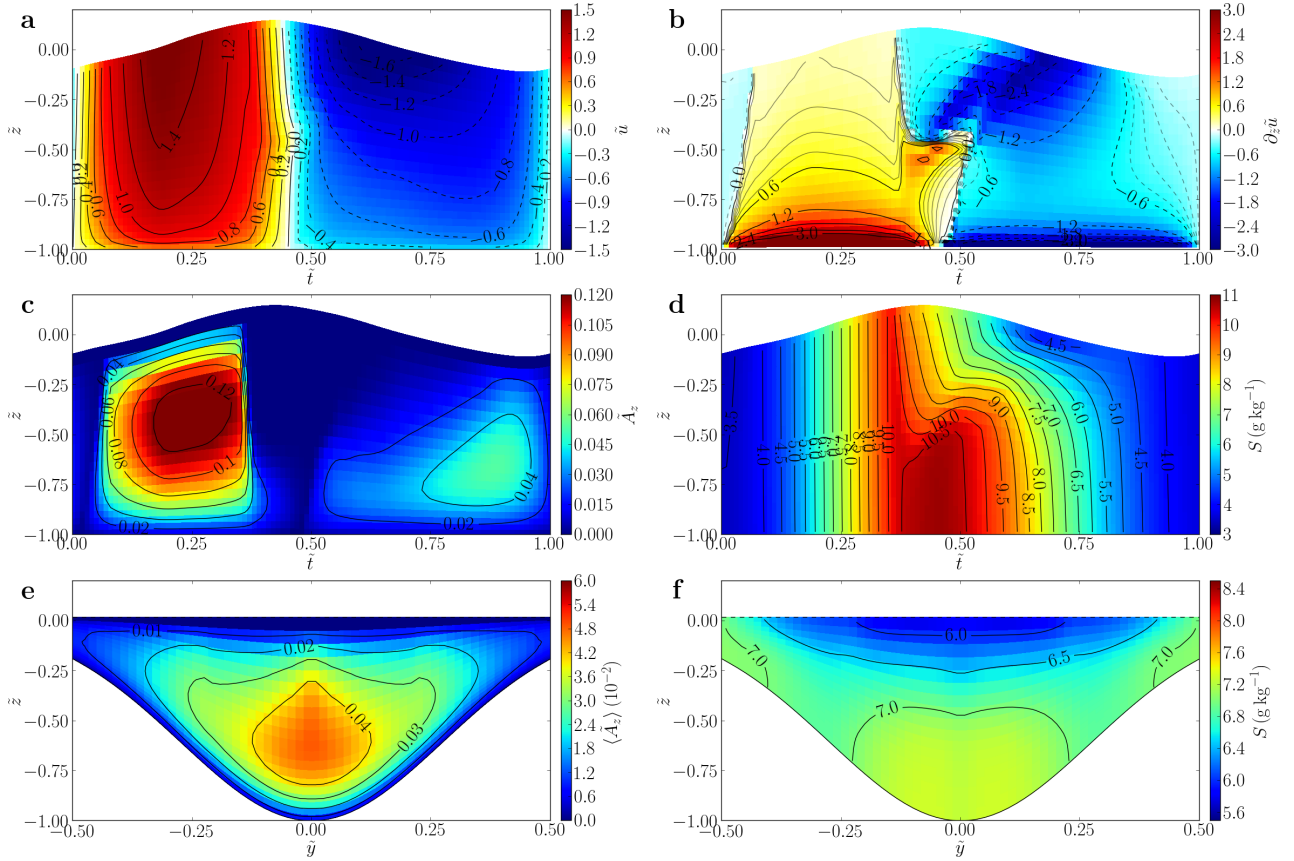


Figure 5.2.: **a-d** Tidal cycles at thalweg of **a** non-dimensional longitudinal velocity, **b** vertical shear of **a**, **c** non-dimensional eddy viscosity and **d** dimensional salinity; **e-f** residual **e** non-dimensional eddy viscosity and **f** dimensional salinity at $x = -40$ km.

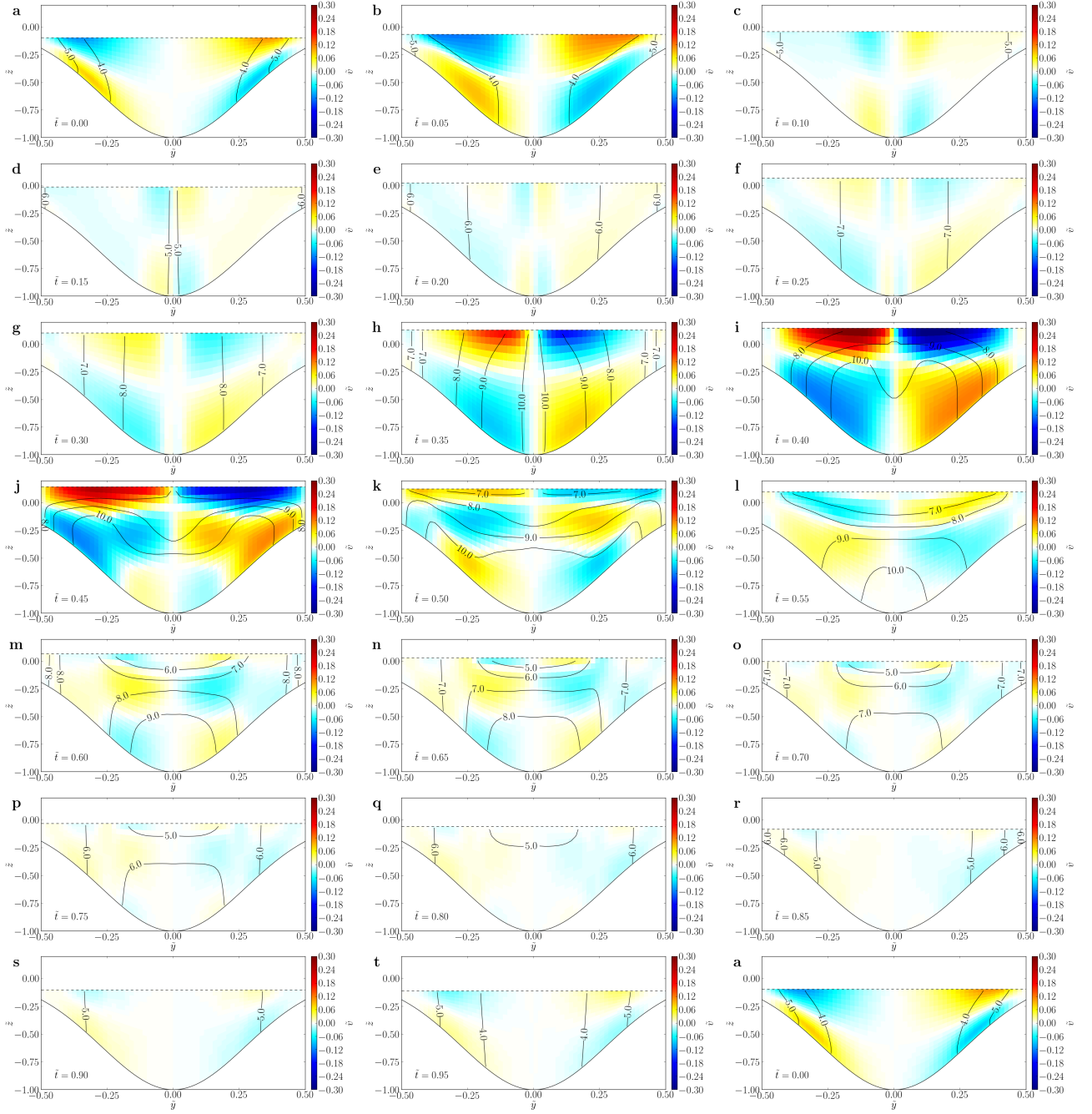


Figure 5.3.: Snapshots of non-dimensional lateral velocity (colour) and dimensional salinity (contours, interval 0.5 psu) at $x = -40$ km. The time is given in the lower left corner of each frame (a $\tilde{t} = 0.00$, b $\tilde{t} = 0.05$ etc.).

Chapter 6

Conclusion and outlook

6.1. Recapitulation

Generally, stratification in an estuary is induced by the vertical shear of the longitudinal ebb currents (faster and thus fresher at the surface) and increased during the ebb phase (longitudinally, primary strain-induced periodic stratification, 1SIPS). However, the surface-convergent transverse circulation during flood can induce stratification, too (mainly laterally, secondary, 2SIPS): It transports fresher water from the shoals (fresher there due to laterally differential longitudinal advection) to the thalweg, at the surface, and spreads the saltier water from the thalweg in the deep channel and along the bottom of the slopes. For a certain, medium aspect ratio ($\alpha \approx 0.004$ for our set of non-dimensional numbers), the two bodies of fresher water just merge at the thalweg (at the surface) at slack after flood so that the stratification is very strong already at the beginning of the ebb phase.

It should be noted that the dominance of 2SIPS over 1SIPS in medium and narrow channels implies that the consideration of only longitudinal forcing parameters, e.g. $\partial_x b$ and U_* in the Simpson number, is not sufficient for a prediction of the stratification.

Strong stratification during ebb suppresses the eddy viscosity and gives rise to strong shear. Thus, the tidal asymmetry of stratification, eddy viscosity and shear is high and drives an intense longitudinal tidal straining circulation in medium channels. Since this is the dominant contribution to the total residual longitudinal circulation in tidally energetic, weakly (primarily) stratified estuaries, the estuarine circulation is maximum in these medium channels.

In wide channels, 2SIPS and other transverse processes are very weak, i.e. hardly any additional stratification is induced, so that the tidal straining circulation is comparably weak. Very wide channels are laterally homogeneous and resemble a one-dimensional situation.

In narrow channels, transverse processes (mainly 2SIPS and vertically, tertiary advected and strain-induced periodic stratification, 3ASIPS) are very strong and stable stratification is induced already before full flood and persists throughout ebb. 1SIPS further increases the stratification, but this also gives rise to the shear, which eventually produces turbulence and thus decreased stratification and increased eddy viscosity during ebb. This reverse tidal asymmetry of eddy viscosity leads to a reverse tidal straining circulation.

The total, estuarine circulation does not reverse because the advectively driven contribution is the dominant one in narrow channels. As suggested by Lerczak and Geyer (2004), the intensity of the advectively driven circulation increases with the aspect ratio.

The complex dynamics of the tidal straining circulation can be further investigated by means of reduced experiments ignoring certain processes, e.g. the transverse advection of salinity. This theoretical investigation reveals that the orientation of the isotachs of longitudinal velocity and of the isohalines with respect to each other plays an important role. If they are aligned, the shear-stratification feedback during the ebb phase is much stronger so that the ebb-flood asymmetry of shear and stratification is high. Thus, the synchronous transverse advection of momentum and salinity is essential for a strong tidal straining circulation.

The impact of the aspect ratio on the residual longitudinal circulation is based on the impact of the channel slope, $\partial_y H$, which increases with increasing α . The slope can also be changed by varying the ratio of the minimum to the maximum water depth; the slope can be increased by decreasing this ratio, e.g. by decreasing H_{\min} . The results of such a variation are comparable to those of varying α , but the change of the local non-dimensional bottom roughness length at the shores, z_0^b/H_{\min} , (if $\tilde{z}_0^b = z_0^b/H_{\max}$) needs to be taken into account. The same holds for the other parameters which are scaled with the water depth or the channel width and also when other geometrical parameters are varied, e.g. $\lambda = 1 - \text{FWHM}/W$.

An increase of the (non-dimensional) quasi-lateral diffusivity, A_{y*} , has a damping impact on all circulation contributions except the tidal straining circulation, which exhibits maximum intensity for low to medium diffusivity. The damping of the other contributions is associated with the decrease of residual stratification, i.e. with the increase of residual eddy viscosity. This also causes the damping of the tidal straining circulation for medium to high diffusivities. The maximum for low to medium diffusivities is associated with a maximum of the viscosity-shear covariance.

The investigations summarised above are conducted with a two-dimensional, rigid-lid model. A decomposition of the estuarine circulation is also possible for more realistic, three-dimensional models with free surface elevation. To this, the calculation is based on σ coordinates and the instantaneous as well as the residual water depth need to be considered. The impact of the aspect ratio on the total residual longitudinal circulation shown with the two-dimensional model can also be found with a three-dimensional, free-surface model.

6.2. Applicability to reality

The applicability of a highly idealised model to a real estuary is limited in terms of predicting estuarine circulation, stratification or other processes or variables. However, it is the simplification of complex systems which allows the fundamental research necessary to understand the individual mechanisms of complex dynamics.

The simplified two-dimensional model used in this study could not only reveal but (help to) explain the dependency of estuarine circulation on the depth-to-width ratio of an estuarine channel. An additional, three-dimensional model confirmed the results, both the outcome and the origin.

The concept of non-dimensional numbers is certainly useful to eliminate the impact of other parameters in the theoretical investigation of the impact of one parameter of interest. However, it is problematic when compared to a real estuary. For example, the bottom roughness length does not scale with the water depth, but it depends on the physical and biological nature of the local sea

floor. (Considering photophilic plants only, the bottom roughness length could actually be larger in shallow and smaller in deeper water.) Similarly, the horizontal diffusivity does not scale (positively) with the channel width, but it depends on along-channel irregularities, e.g. variations of the width or jetties (Burchard, pers. comm.). In this regard, also the isotropy of the horizontal diffusivity ($A_x = A_y$) is questionable.

6.3. Future prospects

The simulation of a realistic modification scenario would be very interesting. For example, one could compare circulations, stratification and other processes and variables in an estuary between a natural setup without a navigational channel and an anthropogenic setup with such a deep channel. Similarly, the effect of land reclamation could be analysed in detail.

Such studies would be immensely valuable for a proper management of estuaries. For example, considering the impact of a channel's depth-to-width ratio, it is possible that the estuarine circulation increases after a navigational channel has been dredged. This is likely to increase the up-estuary sediment transport so that the channel and an adjacent harbour could silt up faster than before the dredging. It would therefore be very useful to know in advance which consequences are to be expected or even which dredging depth or location is optimal in terms of future up-estuary sediment transport.

Such studies require detailed knowledge of all parameters and their dependencies, e.g. the change of the bottom roughness length in case of dredging. Thus, field observations as well as laboratory experiments are needed.

Considering the possible effect of dredging on the estuarine circulation, i.e. the effect of the channel shape on the circulation, one can also ask reversely: How does the estuarine circulation affect the channel shape? In this regard, simulations including sediment transport and morphodynamics are in order. Even an idealised two-dimensional model like the one used in this study could, combined with a morphodynamic model, help to find out what shape an estuarine channel tends to in terms of a stable state. As indicated above, the knowledge of such a state would be very valuable for estuarine management.

Appendix A

About the two-dimensional model

A.1. Alternative equation of state

Burchard et al. (2011) used the linear equation of state as implemented in GETM:

$$\rho = \rho_0 + \text{dtr0}(T - T_0) + \text{dsr0}(S - S_0) \quad (\text{A.1})$$

with $\rho_0 = 1025 \text{ kg/m}^3$ the reference density, $S_0 = 15 \text{ psu}$ the reference salinity and $\text{dsr0} = 0.78 \text{ kg/m}^3/\text{psu}$ the saline expansion coefficient. Note that we set the thermal expansion coefficient to zero, $\text{dtr0} = 0$, so that the temperature dependency is ignored. (The temperature in our estuary is constant, anyway.)

An approximate linear equation of state for the buoyancy is

$$b = -g\beta S \quad (\text{A.2})$$

with $\beta = 7.8 \cdot 10^{-4}/\text{psu}$ the haline contractivity. In order to obtain this as an exact result from the equation of state and the definition of the buoyancy,

$$b := -g \frac{\rho - \rho_0}{\rho_0}, \quad (\text{A.3})$$

we use an alternative equation of state here:

$$\rho = \rho_0 + \rho_0\beta S \quad (\text{A.4})$$

The implementation with an additional `eqstate_method=0` selectable in the file `getm.inp` is shown in Src. A.1. (!ef denotes my source code modifications.)

Source code A.1: GETMDIR/src/3d/eqstate.F90

```
1 <snip>
2 ! !INTERFACE:
3   subroutine do_eqstate()
4 <snip>
5   select case (eqstate_method)
6 !ef alt.eq.st.: (added)
7     case (0)
```

```

8      forall(i=imin-HALO:imax+HALO,j=jmin-HALO:jmax+HALO,az(i,j) .gt. 0) &
9          rho(i,j,1:kmax) = rho_0 + rho_0*beta*S(i,j,1:kmax)
10 !ef alt.eq.st.
11     case (1)
12         forall(i=imin-HALO:imax+HALO,j=jmin-HALO:jmax+HALO,az(i,j) .gt. 0) &
13             rho(i,j,1:kmax) = rho_0 +
14                 dtr0*(T(i,j,1:kmax)-T0) + dsr0*(S(i,j,1:kmax)-S0)
15 <snip>
16     end select
17 <snip>
18 end subroutine do_eqstate
19 <snip>

```

A.2. Calculation of the channel geometry

A.2.1. Coefficients of the Gaussian curve

The coefficients in (2.8) are determined by the conditions (2.9). c_1 and c_2 can be calculated analytically:

$$c_1 = H_{\max} - c_2, \quad (\text{A.5})$$

$$c_2 = \frac{H_{\max} - H_{\min}}{1 - \exp\left(-c_3 \frac{W^2}{4}\right)}. \quad (\text{A.6})$$

c_3 can be found numerically by means of the bisection method using the following equation, which was derived from (2.8) and the third condition (2.9) with (A.5) and (A.6) inserted:

$$\lambda = 1 - \frac{2}{W} \sqrt{-\frac{1}{c_3} \ln \left(1 - \frac{1}{2} H_{\max} \frac{1 - \exp\left(-c_3 \frac{W^2}{4}\right)}{H_{\max} - H_{\min}} \right)}. \quad (\text{A.7})$$

For invariant λ (2.12) and \tilde{H}_{\min} (2.13), c_1 and c_2 have to scale with H_{\max} and c_3 has to scale with $1/W^2$. Thus, $H(y)$ (2.8) scales with H_{\max} as expected.

A.2.2. Cross-sectional area and mean depth

For simplicity, we shift the Gaussian curve (2.8) by $W/2$ to the left:

$$H(y) = c_1 + c_2 \exp(-c_3 y^2). \quad (\text{A.8})$$

The integral of this expression,

$$\int H(y) dy = c_1 y + \frac{c_2}{2} \sqrt{\frac{\pi}{c_3}} \operatorname{erf}(\sqrt{c_3} y), \quad (\text{A.9})$$

contains the error function, which can be approximated as follows:

$$\begin{aligned} \operatorname{erf}(x) &= \frac{2}{\sqrt{\pi}} \int_0^x \exp(-t^2) dt \\ &\approx \operatorname{sign}(x) \sqrt{1 - \exp\left(-x^2 \frac{\frac{4}{\pi} + ax^2}{1 + ax^2}\right)} \\ \text{with } a &= \frac{8(\pi - 3)}{3\pi(4 - \pi)} \approx 0.140012. \end{aligned} \quad (\text{A.10})$$

Thus, the cross-sectional area can be calculated semi-analytically (semi due to c_3 , see section A.2.1):

$$A = \int_0^W H(y) dy = 2 \int_0^{W/2} H(y) dy \quad (\text{A.11})$$

$$= 2 \left[c_1 y + \frac{c_2}{2} \sqrt{\frac{\pi}{c_3}} \operatorname{erf}(\sqrt{c_3} y) \right]_0^{W/2} = c_1 W + c_2 \sqrt{\frac{\pi}{c_3}} \operatorname{erf}\left(\frac{\sqrt{c_3} W}{2}\right) \quad (\text{A.12})$$

The area scales with W and H_{\max} (see end of last section for scaling of c_1 - c_3),

$$A \propto W H_{\max}. \quad (\text{A.13})$$

The mean depth can be formulated as

$$H_{\text{mean}} = \frac{2}{W} \int_0^{W/2} H(y) dy = \frac{A}{W} \propto H_{\max}. \quad (\text{A.14})$$

In post-processing, the cross-sectional area can also be derived from the grid spacing, i.e. the grid cell width in the across-channel direction, dy , and the grid cell height, dz :

$$A = \sum_{y,z} dy dz. \quad (\text{A.15})$$

A.3. Dimensional analysis

The estuary at hand is characterised by the nine parameters given in Tab. 2.1 and, added here for completeness, the Coriolis parameter, $f = 2\Omega \sin \varphi$ with φ the latitude and $\Omega = 2\pi/T_E$ the rotation rate of the Earth (rotation period $T_E = 23.93$ d, one sidereal day). (Please recall that the quasi-lateral diffusivity of salinity equals that of momentum, $K_{y*} = A_{y*}$.) These ten parameters involve two dimensions: the length dimension, L with $[L] = \text{m}$ (meter), and the time dimension, T with $[T] = \text{s}$ (second). Their combinations can be described by means of a dimension matrix, the entries of which are the powers of the dimensions, e.g. $(1, 0)$ for the width, $[W] = \text{m} = \text{m}^1 \text{s}^0$. The dimension matrix for the ten parameters is shown in Tab. A.1.

The order of this matrix is two. Consequently, the estuary can be characterised by $10 - 2 = 8$ linearly independent non-dimensional numbers (Buckingham 1914; Brand 1957; Kalagnanam et al. 1994). These form a fundamental system of the dimension matrix. All of these eight non-dimensional

	W	FWHM	H_{\max}	H_{\min}	z_0^b	ω	f	$\partial_x b$	U_*	A_{y*}
m	1	1	1	1	1	0	0	0	1	2
s	0	0	0	0	0	-1	-1	-2	-1	-1

Table A.1.: Dimension matrix for the ten parameters characterising the two-dimensional system.

numbers are products of powers of the ten variables, e.g. the aspect ratio:

$$\alpha = H_{\max}/W = W^{-1} \text{FWHM}^0 H_{\max}^1 H_{\min}^0 (z_0^b)^0 \omega^0 f^0 (\partial_x b)^0 U_*^0 A_{y*}^0. \quad (\text{A.16})$$

There are infinitely many possible fundamental systems. An appropriate and in part commonly used one (e.g. Burchard 2009; Burchard et al. 2011) is described by the fundamental matrix shown in Tab. A.2.

	W	FWHM	H_{\max}	H_{\min}	z_0^b	ω	f	$\partial_x b$	U_*	A_{y*}
Si	0	0	2	0	0	0	0	1	-2	0
Un	0	0	1	0	0	1	0	0	-1	0
\tilde{z}_0^b	0	0	-1	0	1	0	0	0	0	0
\tilde{A}_{y*}	-1	0	0	0	0	0	0	0	-1	1
$1 - \lambda$	-1	1	0	0	0	0	0	0	0	0
\tilde{H}_{\min}	0	0	-1	1	0	0	0	0	0	0
α	-1	0	1	0	0	0	0	0	0	0
E_i	0	0	1	0	0	0	1	0	-1	0

Table A.2.: Fundamental matrix of the system. The names and equations of the first seven non-dimensional numbers are given in Tab. 2.1, of E_i in (A.17).

$$E_i = f H_{\max} / U_* \quad (\text{A.17})$$

is the inverse Ekman number (Burchard 2009).

A note on the model grid size Besides these physical parameters and numbers, numerical properties of the applied model can influence the results. Preliminary self-similarity tests for this study revealed an unexpected dependency on the longitudinal grid size, dx , for which no explanation could be found. (Please recall that the slice model lies in the y - z plane and that all variables are homogeneous in the x direction, see Burchard et al. 2011.) The problem is solved by keeping the non-dimensional longitudinal grid size, $\widetilde{dx} = dx/W$, constant. For the sake of convenience, it is assigned the same value as the non-dimensional lateral grid size,

$$\widetilde{dx} = \widetilde{dy} = dy/W = 1/J \quad (\text{A.18})$$

with $J = 200$ the invariant number of grid boxes in the lateral direction. Thus, the base area of each grid box is a square with $dx = dy = W/J$.

A.4. Implementation of the reduced experiments

The reduced experiments (sections 2.3.1, 2.4.3.1, 3.2) are implemented by commenting out the respective calls of the advection routine or by ignoring the lateral internal pressure gradient in the lateral momentum budget:

C: no advection of longitudinal and lateral momentum, Src. A.2,

D: no effect of the lateral internal pressure gradient on the lateral momentum, Src. A.3,

F: no transverse advection of salinity, Src. A.4.

(`!ef` denotes my source code modifications.)

It should be noted that the slice model in GETM lies in the x - z plane instead of in the y - z plane. This means that `vv` is the longitudinal velocity, u (both positive up-river), and `uu` is the lateral velocity, $-v$ (cp. Fig. 2.1a).

Please also note that commenting out the call of the advection routine for salinity (experiment F, lines 6-8 in Src. A.4) does not affect the longitudinal advection of salinity. That routine does not actually advect salinity longitudinally because the salinity field in the x - z slice model is homogeneous in the y direction ($dS/dy=0$). Longitudinal advection of salinity with a constant longitudinal salinity gradient, `dys_const`, has already been implemented by Hans Burchard (`!hb`; lines 18, 41, 50, 58 in Src. A.4).

Similarly, there is no longitudinal advection of momentum because the velocity fields are homogeneous in that direction. Therefore, “no advection of momentum” has the same meaning as “no transverse advection of momentum” (experiment C).

Source code A.2: GETMDIR/src/3d/uv_advect_3d.F90 (experiment C)

```

1 <snip>
2 ! !INTERFACE:
3   subroutine uv_advect_3d(hor_adv,ver_adv,adv_split,n)
4 <snip>
5 !ef expC: (comment out)
6 !   call do_advection_3d(dt,uuEx,uadv,vadv,wadv,huadv,hvadv,hoadv,hnadv,&
7 !                       dxuadv,dxvadv,dyuadv,dyvadv,area_inv,&
8 !                       azadv,auadv,avadv,hor_adv,ver_adv,adv_split,AH)
9 !ef expC.
10  uuEx=-(uuEx*hun-uu)/dt ! Here, uuEx is the advection term.
11 <snip>
12 !ef expC: (comment out)
13 !   call do_advection_3d(dt,vvEx,uadv,vadv,wadv,huadv,hvadv,hoadv,hnadv,&
14 !                       dxuadv,dxvadv,dyuadv,dyvadv,area_inv,&
15 !                       azadv,auadv,avadv,hor_adv,ver_adv,adv_split,AH)
16 !ef expC.
17  vvEx=-(vvEx*hvn-vv)/dt ! Here, vvEx is the advection term.
18 <snip>
19  end subroutine uv_advect_3d
20 <snip>
```

Source code A.3: GETMDIR/src/3d/uu_momentum_3d.F90 (experiment D)

```

1 <snip>
```

```

2  ! !INTERFACE:
3      subroutine uu_momentum_3d(n,bdy3d)
4  <snip>
5  !ef expD: (idpdx=0)
6  !
7      ex(k)=dry_u(i,j)*(ex(k)-uuEx(i,j,k)+ip_fac*idpdx(i,j,k))
8      ex(k)=dry_u(i,j)*(ex(k)-uuEx(i,j,k))
9  !ef expD.
10 <snip>
11 end subroutine uu_momentum_3d
12 <snip>

```

Source code A.4: GETMDIR/src/3d/salinity.F90 (experiment F)

```

1  <snip>
2  ! !INTERFACE:
3      subroutine do_salinity(n)
4  <snip>
5  !ef expF: (comment out)
6  !      call do_advection_3d(dt,S,uu,vv,ww,hun,hvn,ho,hn,      &
7  !          delxu,delxv,delyu,delyv,area_inv,az,au,av,      &
8  !          salt_hor_adv,salt_ver_adv,salt_adv_split,salt_AH)
9  !ef expF.
10 <snip>
11 ! Advection and vertical diffusion and of salinity
12 <snip>
13 !hb dys: (added)
14     do j=jmin,jmax
15         do i=imin,imax
16             do k=1,kmax
17 <snip>
18                 dys(i,j,k)=dys_const
19 <snip>
20             end do
21         end do
22     end do
23 !hb dys.
24 <snip>
25     do j=jmin,jmax
26         do i=imin,imax
27             if (az(i,j) .eq. 1) then
28                 if (kmax.gt.1) then
29 ! Auxilury terms, old and new time level,
30                     do k=1,kmax-1
31                         auxo(k)=2.*(1-cnpar)*dt*(nuh(i,j,k)+avmols)/ &
32                             (hn(i,j,k+1)+hn(i,j,k))
33                         auxn(k)=2.* cnpar *dt*(nuh(i,j,k)+avmols)/ &
34                             (hn(i,j,k+1)+hn(i,j,k))
35                     end do
36 ! Matrix elements for surface layer
37                     k=kmax
38                     a1(k)=-auxn(k-1)
39                     a2(k)=hn(i,j,k)+auxn(k-1)
40                     a4(k)=S(i,j,k)*(hn(i,j,k)-auxo(k-1))+S(i,j,k-1)*auxo(k-1) &
41                         -vv(i,j,k)*dys(i,j,k)*dt !hb dys (added)
42 ! Matrix elements for inner layers

```

```

43         do k=2,kmax-1
44             a3(k)=-auxn(k )
45             a1(k)=-auxn(k-1)
46             a2(k)=hn(i,j,k)+auxn(k)+auxn(k-1)
47             a4(k)=S(i,j,k+1)*auxo(k) &
48                 +S(i,j,k )*(hn(i,j,k)-auxo(k)-auxo(k-1)) &
49                 +S(i,j,k-1)*auxo(k-1) &
50                 -vv(i,j,k)*dys(i,j,k)*dt !hb dys (added)
51         end do
52 !         Matrix elements for bottom layer
53         k=1
54         a3(k)=-auxn(k )
55         a2(k)=hn(i,j,k)+auxn(k)
56         a4(k)=S(i,j,k+1)*auxo(k) &
57             +S(i,j,k )*(hn(i,j,k)-auxo(k)) &
58             -vv(i,j,k)*dys(i,j,k)*dt !hb dys (added)
59 <snip>
60         end if
61     end if
62 end do
63 end do
64 <snip>
65 end subroutine do_salinity
66 <snip>

```

A.5. Further figures

A.5.1. Reduced experiment F (to section 3.2.3F)

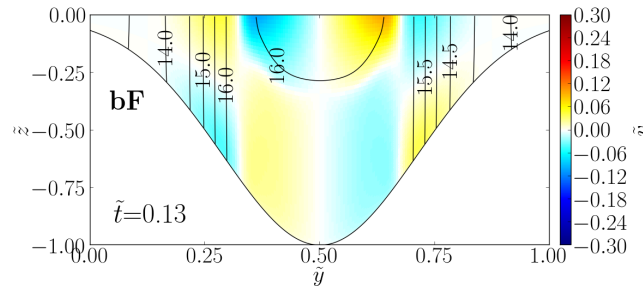


Figure A.1.: Non-dimensional lateral velocity (colour) and dimensional salinity (contours, interval 0.5 psu) in experiment F at $\tilde{t} = 0.13$ (to Fig. 3.3).

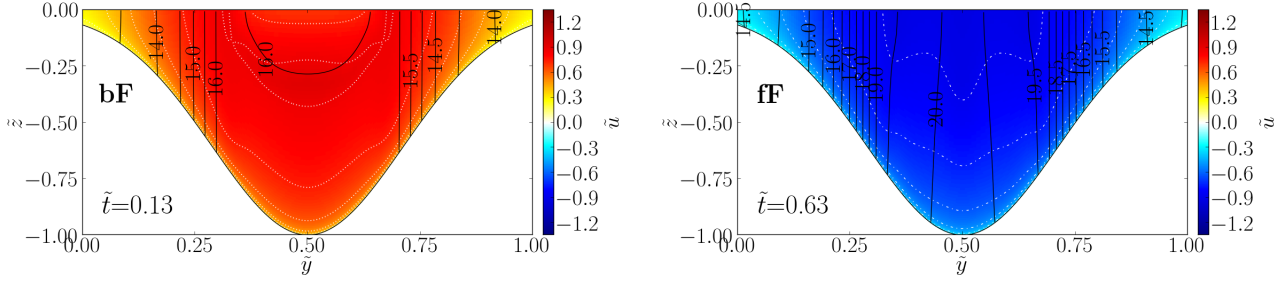


Figure A.2.: Non-dimensional longitudinal velocity (colour) and dimensional salinity (contours, interval 0.5 psu) in experiment F at **bF** $\tilde{t} = 0.13$ and **fF** 0.63 (to Fig. 3.4).

A.5.2. Impact of the aspect ratio, α , and the Simpson number, Si (to section 2.4.3.2)

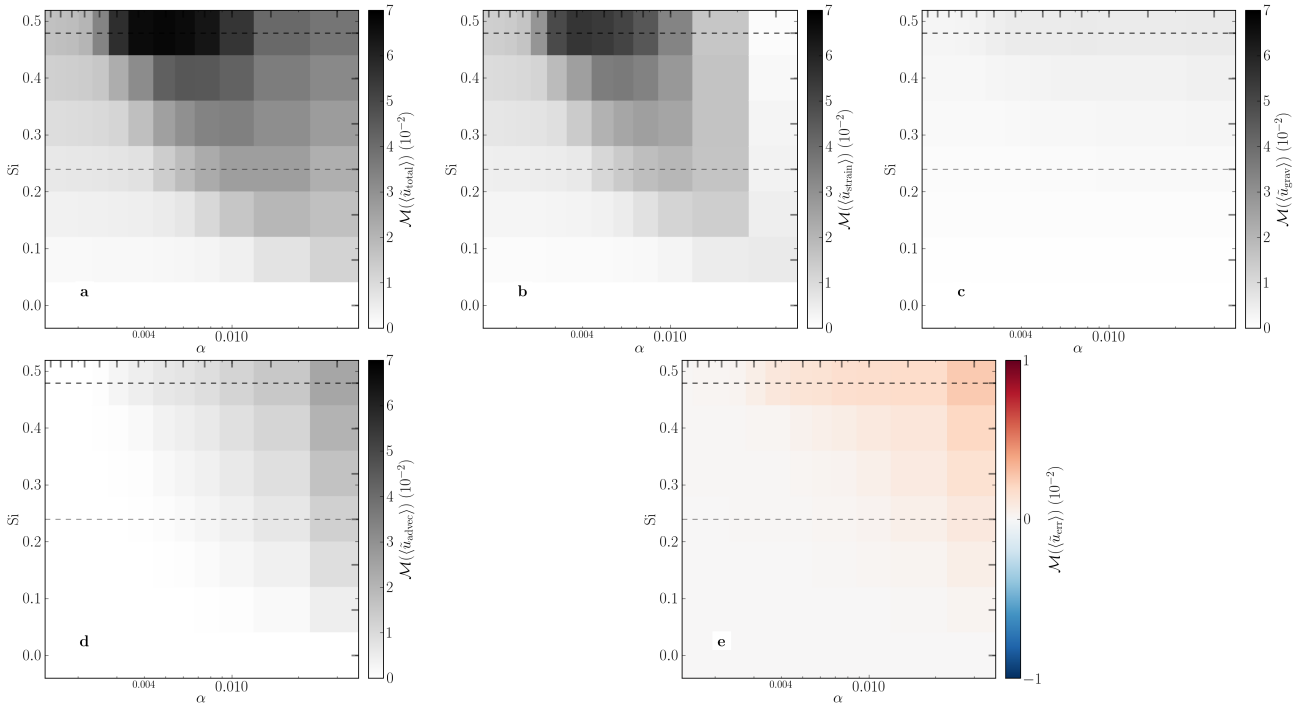


Figure A.3.: Measure of the intensity of the residual longitudinal circulation contributions in the 2D parameter space spanned by the aspect ratio and the Simpson number (other parameters as in Tab. 2.1). **a** Total, **b** tidal straining (same as Fig. 2.11), **c** gravitational, **d** advectively driven and **e** error circulation. The short bars at the upper abscissa and at the right ordinate mark the α and Si values of the individual simulations. The black dashed line corresponds to Fig. 2.2; the grey dashed line corresponds to Fig. 2.10c (α range marked at lower abscissa there).

Appendix B

About the three-dimensional model

B.1. River discharge weighting scheme in consideration of the water depth

In order to distribute the total discharge of a multiple-cell river in consideration of the cells' water depth (section 5.2), the depth information is needed for the river initialisation. For parallel computation, this information is needed from all subdomains affected by the river.

An according weighting scheme is implemented as shown in Src. B.1. (!ef denotes my source code modifications.)

Source code B.1: GETMDIR/src/3d/rivers.F90

```
1 <snip>
2 !!INTERFACE:
3   module rivers
4 <snip>
5 !!INTERFACE:
6   subroutine init_rivers
7 <snip>
8 !!USES:
9 !ef(weight_H_global):
10    use domain, only: iextr, jextr
11    use m2d, only: get_2d_field
12 !ef(weight_H_global).
13    IMPLICIT NONE
14    !
15    !!LOCAL VARIABLES:
16 <snip>
17 !ef(weight_H_global):
18    REALTYPE, dimension(1:iextr,1:jextr) :: H_global
19 !ef(weight_H_global).
20 <snip>
21    select case (river_method)
22    case (0)
23        LEVEL3 'River runoff not included.'
24    case (1,2)
25 <snip>
26        LEVEL2 'weighting multi-cell river flow with water depth'
27        !ef(weight_H) comment
```

```

27 !ef(weight_H_global):
28     call get_2d_field("topo.nc","bathymetry", &
29                     1,iextr,1,jextr,.true.,H_global)
30 !ef(weight_H_global).
31 <snip>
32     flow_fraction_rel = _ZERO_
33     do n=1,nriver
34         read(unit,*) ir(n),jr(n),river_name(n)
35 <snip>
36 ! Other weighting schemes could be implemented here. But we can only use
37 ! information, which is available for cells also outside the present
38 ! subdomain.
39 ! flow_fraction(n) = _ONE_/ARCD1 ! This does not work.
40 !ef(weight_H_global)! flow_fraction_rel(n) = _ONE_
41 flow_fraction_rel(n) = H_global(ir(n),jr(n)) !ef(weight_H_global)
42 <snip>
43 end do
44 <snip>
45 do iriver=1,nriver
46     numcells=0
47     total_weight=_ZERO_
48     do jriver=1,nriver
49         if (river_name(iriver) .eq. river_name(jriver)) then
50             numcells = numcells+1
51             total_weight = total_weight+flow_fraction_rel(jriver)
52 <snip>
53         end if
54     end do
55     river_split(iriver) = numcells
56     flow_fraction(iriver) = flow_fraction_rel(iriver)/total_weight
57 end do
58 <snip>
59 end select
60 return
61 <snip>
62 end subroutine init_rivers
63 <snip>
64 end module rivers
65 <snip>

```


List of Figures

1.1	Schematic of gravitational circulation	2
1.2	Schematic of strain-induced periodic stratification (SIPS)	3
1.3	Schematic of tidal straining circulation	4
1.4	Schematic of laterally differential longitudinal advection and transverse circulation	4
2.1	Schematic of the 2D model domain and Gaussian depth profiles	8
2.2	Intensity of estuarine circulation contributions for varying aspect ratio	14
2.3	Residual circulation, eddy viscosity and salinity profiles for different aspect ratios	16
2.4	Tidal cycles of velocity, shear, eddy viscosity, salinity and Ri for different aspect ratios	17
2.5	Snapshots of lateral velocity and salinity for different aspect ratios	19
2.6	Transverse salinity advection (particle tracking) for different aspect ratios	22
2.7	Stratifying and destratifying terms (1SIPS, 2/3ASIPS, vertical diffusion) over α	23
2.8	Schematic of secondary straining (2SIPS)	25
2.9	Tidal straining intensity, viscosity-shear covariance and residual eddy viscosity over α in reduced experiments	26
2.10	Intensity of estuarine circulation contributions over α with different parameters	26
2.11	Tidal straining intensity for varying aspect ratio and Simpson number	27
2.12	Potential density anomaly and vertical mixing of salinity over α	28
2.13	Topography of the 3D model and estuarine circulation intensity over α	29
3.1	Residual circulation, eddy viscosity and salinity profiles for different experiments	39
3.2	Tidal cycles of velocity, shear, eddy viscosity, salinity and Ri for different experiments	41
3.3	Snapshots of lateral velocity and salinity for different experiments	44
3.4	Snapshots of longitudinal velocity and salinity for different experiments	45
4.1	Intensity of estuarine circulation contributions, viscosity-shear covariance and residual eddy viscosity over \tilde{A}_{y*}	48
4.2	Residual circulation, eddy viscosity and salinity profiles for different \tilde{A}_{y*}	50
4.3	Tidal cycles of velocity, shear, eddy viscosity, salinity and Ri for different \tilde{A}_{y*}	51
4.4	Snapshots of lateral velocity and salinity for different \tilde{A}_{y*}	52
4.5	Intensity of estuarine circulation contributions over α and \tilde{H}_{min}	53
4.6	Intensity of estuarine circulation contributions over α and λ	55
5.1	Residual longitudinal circulation contributions at $x = -40$ km (3D, free surface)	63
5.2	Residuals and tidal cycles of salinity, eddy viscosity, longitudinal velocity and its vertical shear (3D, free surface)	64
5.3	Snapshots of lateral velocity and salinity (3D, free surface)	65

A.1	Snapshot of lateral velocity and salinity for experiment F, $\tilde{t} = 0.13$ (to Fig. 3.3)	VII
A.2	Snapshots of longitudinal velocity and salinity for exp. F, $\tilde{t} = 0.13, 0.63$ (to Fig. 3.4)	VIII
A.3	Intensity of estuarine circulation contributions over α and Si	VIII

List of Tables

2.1	Dimensional parameters and non-dimensional numbers with their reference values or variation ranges	10
2.2	Aspect ratios of several real estuaries	12
2.3	Overview of the characteristics leading to maximum tidal straining circulation	18
2.4	Parameters for the three-dimensional simulations	30
3.1	Intensity of estuarine circulation contributions for full and reduced experiments	35
3.2	Intensity of covariance contributions for different pairs of experiments	37
4.1	Intensity of estuarine circulation contributions for different λ and non-dimensionalisation bases	55
5.1	Intensity of estuarine circulation contributions at different cross-sections (3D, free surface)	62
A.1	Dimension matrix for the parameters characterising the two-dimensional system	IV
A.2	Fundamental matrix of the two-dimensional system	IV

List of Source codes

A.1	eqstate.F90 (alternative equation of state)	I
A.2	uv_advect_3d.F90 (experiment C)	V
A.3	uu_momentum_3d.F90 (experiment D)	V
A.4	salinity.F90 (experiment F)	VI
B.1	rivers.F90 (weighting of multiple-cell river flow with water depth)	IX

References

- Agnew, R., 1960: Estuarine currents and tidal streams. *Coast. Eng. Proc.*, **7**, 510–535.
- Banas, N. S. and B. M. Hickey, 2005: Mapping exchange and residence time in a model of willapa bay, washington, a branching, macrotidal estuary. *J. Geophys. Res.*, **110**, C11011, doi:10.1029/2005JC002950.
- Becherer, J., H. Burchard, G. Flöser, V. Mohrholz, and L. Umlauf, 2011: Evidence of tidal straining in well-mixed channel flow from microstructure observations. *Geophys. Res. Lett.*, **38**, L17611, doi:10.1029/2011GL049005.
- Becherer, J., M. T. Stacey, L. Umlauf, and H. Burchard, 2014: Lateral circulation generates flood-tide stratification and estuarine exchange flow in a curved tidal inlet. *J. Phys. Oceanogr.*, doi:10.1175/JPO-D-14-0001.1.
- Becherer, J. and L. Umlauf, 2011: Boundary mixing in lakes: 1. Modeling the effect of shear-induced convection. *J. Geophys. Res.*, **116**, C10017, doi:10.1029/2011JC007119.
- Brand, L., 1957: The pi theorem of dimensional analysis. *Archive for Rational Mechanics and Analysis*, **1**, 35–45, doi:10.1007/BF00297994.
- Buckingham, E., 1914: On physically similar systems; illustrations of the use of dimensional equations. *Phys. Rev.*, **4**, 345–376, doi:10.1103/PhysRev.4.345.
- Burchard, H., 2009: Combined effects of wind, tide, and horizontal density gradients on stratification in estuaries and coastal seas. *J. Phys. Oceanogr.*, **39**, 2117–2136, doi:10.1175/2009JPO4142.1.
- Burchard, H., G. Flöser, J. V. Staneva, T. H. Badewien, and R. Riethmüller, 2008: Impact of density gradients on net sediment transport into the Wadden Sea. *J. Phys. Oceanogr.*, **38**, 566–587, doi:10.1175/2007JPO3796.1.
- Burchard, H. and R. D. Hetland, 2010: Quantifying the contributions of tidal straining and gravitational circulation to residual circulation in periodically stratified tidal estuaries. *J. Phys. Oceanogr.*, **40**, 1243–1262, doi:10.1175/2010JPO4270.1.
- Burchard, H., R. D. Hetland, E. Schulz, and H. M. Schuttelaars, 2011: Drivers of residual estuarine circulation in tidally energetic estuaries: Straight and irrotational channels with parabolic cross section. *J. Phys. Oceanogr.*, **41**, 548–570, doi:10.1175/2010JPO4453.1.
- Burchard, H. and R. Hofmeister, 2008: A dynamic equation for the potential energy anomaly for analysing mixing and stratification in estuaries and coastal seas. *Estuar. Coast. Shelf S.*, **77**, 679–687, doi:10.1016/j.ecss.2007.10.025.

- Burchard, H., F. Janssen, K. Bolding, L. Umlauf, and H. Rennau, 2009: Model simulations of dense bottom currents in the Western Baltic Sea. *Cont. Shelf Res.*, **29**, 205–220, doi:10.1016/j.csr.2007.09.010.
- Burchard, H. and O. Petersen, 1997: Hybridisation between σ and z coordinates for improving the internal pressure gradient calculation in marine models with steep bottom slopes. *Int. J. Numer. Meth. Fluids*, **25**, 1003–1023.
- Burchard, H., E. Schulz, and H. M. Schuttelaars, 2014: Impact of estuarine convergence on residual circulation in tidally energetic estuaries and inlets. *Geophys. Res. Lett.*, **41**, 913–919, doi:10.1002/2013GL058494.
- Burchard, H. and H. M. Schuttelaars, 2012: Analysis of tidal straining as driver for estuarine circulation in well-mixed estuaries. *J. Phys. Oceanogr.*, **42**, 261–271, doi:10.1175/JPO-D-11-0110.1.
- Burchard, H., H. M. Schuttelaars, and W. R. Geyer, 2013: Residual sediment fluxes in weakly-to-periodically stratified estuaries and tidal inlets. *J. Phys. Oceanogr.*, **43**, 1841–1861, doi:10.1175/JPO-D-12-0231.1.
- Chant, R. J., 2002: Secondary circulation in a region of flow curvature: Relationship with tidal forcing and river discharge. *J. Geophys. Res.*, **107**, 14–1–14–11, doi:10.1029/2001JC001082.
- de Boer, G. J., J. D. Pietrzak, and J. C. Winterwerp, 2008: Using the potential energy anomaly equation to investigate tidal straining and advection of stratification in a region of freshwater influence. *Ocean Model.*, **22**, 1–11, doi:10.1016/j.ocemod.2007.12.003.
- Geyer, W. R., 1993: Three-dimensional tidal flow around headlands. *J. Geophys. Res.*, **98**, 955–966, doi:10.1029/92JC02270.
- Geyer, W. R. and P. MacCready, 2014: The estuarine circulation. *Annu. Rev. Fluid Mech.*, **46**, 175–197, doi:10.1146/annurev-fluid-010313-141302.
- Geyer, W. R. and J. D. Smith, 1987: Shear instability in a highly stratified estuary. *J. Phys. Oceanogr.*, **17**, 1668–1679, doi:10.1175/1520-0485(1987)017<1668:SHIHS>2.0.CO;2.
- Giddings, S. N., D. A. Fong, S. G. Monismith, C. C. Chickadel, K. A. Edwards, W. J. Plant, B. Wang, O. B. Fringer, A. R. Horner-Devine, and A. T. Jessup, 2012: Frontogenesis and frontal progression of a trapping-generated estuarine convergence front and its influence on mixing and stratification. *Estuaries Coasts*, **35**, 665–681, doi:10.1007/s12237-011-9453-z.
- Hansen, D. V. and M. Rattray, Jr., 1965: Gravitational circulation in straits and estuaries. *J. Mar. Res.*, **23**, 104–122.
- Howlett, E. R., T. P. Rippeth, and J. Howarth, 2011: Processes contributing to the evolution and destruction of stratification in the Liverpool Bay ROFI. *Ocean Dyn.*, **61**, 1403–1419, doi:10.1007/s10236-011-0402-y.

- Huijts, K. M., H. E. de Swart, G. P. Schramkowski, and H. M. Schuttelaars, 2011: Transverse structure of tidal and residual flow and sediment concentration in estuaries. *Ocean Dyn.*, **61**, 1067–1091, doi:10.1007/s10236-011-0414-7.
- Ianniello, J. P., 1979: Tidally induced residual currents in estuaries of variable breadth and depth. *J. Phys. Oceanogr.*, **9**, 962–974, doi:10.1175/1520-0485(1979)009<0962:TIRCIE>2.0.CO;2.
- Jay, D. A. and J. D. Musiak, 1994: Particle trapping in estuarine tidal flows. *J. Geophys. Res.*, **99**, 20445–20461, doi:10.1029/94JC00971.
- 1996: Internal tidal asymmetry in channel flows: origins and consequences. *Mixing in Estuaries and Coastal Seas*, C. Pattiaratchi, ed., American Geophysical Union, Washington, D. C., volume 50 of *Coastal and Estuarine Studies*, chapter 13, 211–249.
- Kalagnanam, J., M. Henrion, and E. Subrahmanian, 1994: The scope of dimensional analysis in qualitative reasoning. *Computat. Intell.*, **10**, 117–133, doi:10.1111/j.1467-8640.1994.tb00160.x.
- Kundu, P. K. and I. M. Cohen, 2002: *Fluid Mechanics*. Academic Press, San Diego, London, second edition, 730 pp. pp.
- Lacy, J. R., M. T. Stacey, J. R. Burau, and S. G. Monismith, 2003: Interaction of lateral baroclinic forcing and turbulence in an estuary. *J. Geophys. Res.*, **108**, 3089, doi:10.1029/2002JC001392.
- Lerczak, J. A. and W. R. Geyer, 2004: Modeling the lateral circulation in straight, stratified estuaries. *J. Phys. Oceanogr.*, **34**, 1410–1428, doi:10.1175/1520-0485(2004)034<1410:MTLCIS>2.0.CO;2.
- Linden, P. F., 1979: Mixing in stratified fluids. *Geophys. Astro. Fluid*, **13**, 3–23, doi:10.1080/03091927908243758.
- 1980: Mixing across a density interface produced by grid turbulence. *J. Fluid Mech.*, **100**, 691–703, doi:10.1017/S002211208000136X.
- Linden, P. F. and J. E. Simpson, 1986: Gravity-driven flows in a turbulent fluid. *J. Fluid Mech.*, **172**, 481–497, doi:10.1017/S0022112086001829.
- 1988: Modulated mixing and frontogenesis in shallow seas and estuaries. *Cont. Shelf Res.*, **8**, 1107–1127, doi:10.1016/0278-4343(88)90015-5.
- Longuet-Higgins, M., 1969: On the transport of mass by time-varying ocean currents. *Deep-Sea Research*, **16**, 431–447.
- MacCready, P. and W. R. Geyer, 2010: Advances in estuarine physics. *Annu. Rev. Mar. Sci.*, **2**, 35–58, doi:10.1146/annurev-marine-120308-081015.
- Nunes, R. A. and J. H. Simpson, 1985: Axial convergence in a well-mixed estuary. *Estuar. Coast. Shelf S.*, **20**, 637–649, doi:10.1016/0272-7714(85)90112-X.
- Peters, H., 1997: Observations of stratified turbulent mixing in an estuary: Neap-to-spring variations during high river flow. *Estuar. Coast. Shelf S.*, **45**, 69–88, doi:10.1006/ecss.1996.0180.

- Pritchard, D. W., 1952: Salinity distribution and circulation in the Chesapeake Bay estuarine system. *J. Mar. Res.*, **11**, 106–123.
- Purkiani, K., J. Becherer, G. Flöser, U. Gräwe, V. Mohrholz, H. M. Schuttelaars, and H. Burchard, 2014: Numerical analysis of stratification and destratification processes in a tidally energetic inlet with an ebb tidal delta. *J. Geophys. Res.*, doi:10.1002/2014JC010325.
- Scully, M. E., C. Friedrichs, and J. Brubaker, 2005: Control of estuarine stratification and mixing by wind-induced straining of the estuarine density field. *Estuaries*, **28**, 321–326, doi:10.1007/BF02693915.
- Scully, M. E. and C. T. Friedrichs, 2007: The importance of tidal and lateral asymmetries in stratification to residual circulation in partially mixed estuaries. *J. Phys. Oceanogr.*, **37**, 1496–1511, doi:10.1175/JPO3071.1.
- Scully, M. E. and W. R. Geyer, 2012: The role of advection, straining, and mixing on the tidal variability of estuarine stratification. *J. Phys. Oceanogr.*, **42**, 855–868, doi:10.1175/JPO-D-10-05010.1.
- Scully, M. E., W. R. Geyer, and J. A. Lerczak, 2009: The influence of lateral advection on the residual estuarine circulation: A numerical modeling study of the hudson river estuary. *J. Phys. Oceanogr.*, **39**, 107–124, doi:10.1175/2008JPO3952.1.
- Simpson, J. H., J. Brown, J. Matthews, and G. Allen, 1990: Tidal straining, density currents, and stirring in the control of estuarine stratification. *Estuaries*, **13**, 125–132, doi:10.2307/1351581.
- Simpson, J. H., D. J. Crisp, and C. Hearn, 1981: The shelf-sea fronts: Implications of their existence and behaviour. *Philos. T. Roy. Soc. A*, **302**, 531–546, doi:10.1098/rsta.1981.0181.
- Smith, R., 1976: Longitudinal dispersion of a buoyant contaminant in a shallow channel. *J. Fluid Mech.*, **78**, 677–688, doi:10.1017/S0022112076002681.
- Souza, A. J., 2013: On the use of the stokes number to explain frictional tidal dynamics and water column structure in shelf seas. *Ocean Sci.*, **9**, 391–398, doi:10.5194/os-9-391-2013.
- Stacey, M. T., J. R. Burau, and S. G. Monismith, 2001: Creation of residual flows in a partially stratified estuary. *J. Geophys. Res.*, **106**, 17013–17037, doi:10.1029/2000JC000576.
- Stacey, M. T., S. G. Monismith, and J. R. Burau, 1999: Observations of turbulence in a partially stratified estuary. *J. Phys. Oceanogr.*, **29**, 1950–1970.
- Valle-Levinson, A., 2008: Density-driven exchange flow in terms of the Kelvin and Ekman numbers. *J. Geophys. Res.*, **113**, C04001, doi:10.1029/2007JC004144.
- Valle-Levinson, A., C. Li, K.-C. Wong, and K. M. M. Lwiza, 2000: Convergence of lateral flow along a coastal plain estuary. *J. Geophys. Res.*, **105**, 17045–17061, doi:10.1029/2000JC900025.
- van Rijn, L. C., 2011: Analytical and numerical analysis of tides and salinities in estuaries; part i: tidal wave propagation in convergent estuaries. *Ocean Dyn.*, **61**, 1719–1741, doi:10.1007/s10236-011-0453-0.

- Waterhouse, A. F., B. Tutak, A. Valle-Levinson, and Y. P. Sheng, 2013: Influence of two tropical storms on the residual flow in a subtropical tidal inlet. *Estuaries Coasts*, **36**, 1037–1053, doi:10.1007/s12237-013-9606-3.
- Waterhouse, A. F. and A. Valle-Levinson, 2010: Transverse structure of subtidal flow in a weakly stratified subtropical tidal inlet. *Cont. Shelf Res.*, **30**, 281–292, doi:10.1016/j.csr.2009.11.008.
- Winant, C. D., 2008: Three-dimensional residual tidal circulation in an elongated, rotating basin. *J. Phys. Oceanogr.*, **38**, 12781295, doi:10.1175/2007JPO3819.1.
- Zimmerman, J. T. F., 1979: On the Euler-Lagrange transformation and the Stokes drift in the presence of oscillatory and residual currents. *Deep-Sea Research A*, **26**, 505–520.